The Mechanics of Growth and Residual Stress in Biological Cylinders

Stephen G. O'Keeffe

Hertford College

University of Oxford

A thesis submitted for the degree of

Doctor of Philosophy

Hilary Term 2015

Abstract

Biological tissue differs from other materials in many ways. Perhaps the most crucial difference is its ability to grow. Growth processes may give rise to stresses that exist in a body in the absence of applied loads and these are known as residual stresses. Residual stress is present in many biological systems and can have important consequences on the mechanical response of a body. Mathematical models of biological structures must therefore be able to capture accurately the effects of differential growth and residual stress, since greater understanding of the roles of these phenomena may have applications in many fields.

In addition to residual stresses, biological structures often have a complex morphology. The theory of 3-D elasticity is analytically tractable in modelling mechanical properties in simple geometries such as a cylinder. On the other hand, rod theory is well-suited for geometrically-complex deformations, but is unable to account for residual stress.

In this thesis, we aim to develop a map between the two frameworks. Firstly, we use 3-D elasticity to determine effective mechanical properties of a growing cylinder and map them into an effective rod. Secondly, we consider a growing filament embedded in an elastic foundation. Here, we estimate the degree of transverse reinforcement the foundation confers on the filament in terms of its material properties. Finally, to gain a greater understanding of the role of residual stress in biological structures, we consider a case study: the chameleon's tongue. In particular we consider

the role of residual stress and anisotropy in aiding the rapid projection of the tongue during prey capture. We construct a mechanical model of the tongue and use it to investigate a proposed mechanism of projection by means of an energy balance argument.

Acknowledgements

I wish to thank my supervisors, Professors Derek Moulton, Sarah Waters and Alain Goriely for the help and guidance they have given me throughout my D.Phil. I am also grateful to Professors Dominic Vella, Peter Howell, Yibin Fu and Luis Dorfmann, and Dr Thomas Lessinnes for the helpful insights, comments and suggestions they have provided over the past three years. Further thanks to Dominic Vella and Professor Giuseppe Saccomandi for acting as my thesis assessors and examiners.

It would not have been possible to produce this thesis without the generous funding supplied by the EPSRC Systems Biology Doctoral Training Centre. I would also like to acknowledge additional funding provided by the Oxford Centre for Collaborative Applied Mathematics (with the support of King Abdullah University of Science and Technology) and the Mathematical Biosciences Institute at Ohio State University, which allowed me to attend study groups, conferences and summer schools during my studies.

I would also like to say a big thank you to my family: my parents, Marilyn and George; my sister, Helen; and my brothers, John and Aidan. I am so grateful for the continued love and support you have given me. I don't know how I would have managed without it.

Finally, thank you to Debbie, my soon-to-be wife, for your love, friendship, support, and above all, putting up with me over the past four years, and for many more to come!

Contents

Chapter 1

Introduction

In recent decades, there has been increased interest in using mathematical models to describe biological problems. This rise is partly due to an increasing abundance of biological data sets, such as DNA sequences and records of epidemiological events, as well as an increase in computing power since the mid 20th century. Moreover, advances in the fields of medicine, materials science, imaging and pharmacology have allowed for the development of novel treatments and early detection of diseases. These treatments have, in turn, led to an increased demand for predictive models that can, for example, help plan treatment programmes or judge the efficacy of a particular therapy. Mechanobiology is a branch of mathematical biology that focusses on the mechanical behaviour of biological structures. The natural world offers a rich array of mechanical problems. Understanding these systems could have applications in areas including engineering, physics, food science and botany. For example, the design of oil rig platform supports is inspired by the microscopic structure of certain species of grass stalks and the spines of mammals such as hedgehogs and porcupines [55].

The challenge for mathematicians is to develop models that can be applied to such a wide range of problems, but are detailed enough that they capture the essential features of biological tissue. Our goal is to contribute towards the development

of models that can be used to study growth, stress, anisotropy and various other features of biological tissue. We are particularly interested in cylindrical structures because working in an idealised geometry allows us to take the initial steps in defining mappings between two different theoretical frameworks, which in turn, allows the study of geometrically-complex deformations of growing filaments. One of these frameworks is well-suited to describing the mechanical behaviour of a body, but is useful only as long as the geometry of the body can be described simply. The other is better-suited to describing the geometry, but its description of the mechanics of the body is less sophisticated. We aim to combine the advantages of each framework so that we obtain a means of studying both mechanically- and geometrically-complex bodies. We also consider an interesting case study that can be well-described using one of these modelling frameworks. The chameleon's tongue presents an interesting mechanical problem, as it is not known for certain how it is able to undergo rapid acceleration. We construct a model of the tongue to investigate a proposed mechanism of projection by considering the kinetic energy it is capable of using. As part of this analysis we consider the role of anisotropy, muscle contraction and residual stress in enabling rapid projection to occur.

1.1 Mechanical Problems in Biology

Biological tissue differs from other types of material in several ways. We begin by discussing the various characteristics of soft tissue, with a particular emphasis on those that are of importance to the work in this thesis.

1.1.1 Growth, Residual Stress and Geometry

Perhaps the most important difference between biological tissue and other types of material is its ability to grow. Growth is the increase in mass of an object and is one

of the fundamental characteristics of all living systems. Not only does it change the size and shape of a body, but it can also affect a body's mechanical properties due to the complex relationship it shares with stress. If different parts of a single body grow at different rates, then stresses are generated, even if no loads are applied to it. This phenomenon is exemplified by a simple experiment (see *e.g.* [5, 99]): take a stalk of rhubarb and measure its length. Now peel the stalk and measure the lengths of both the peeled strips and the remaining pith. It is observed that the peel is shorter than the intact length of the stalk, whilst the pith is longer. This change in length of the stalk's components is caused by the relaxation of these stresses, which are known as residual stresses. Fung was first to note their existence in arteries by carrying out experiments on sections of arterial tissue [26]. He observed that when a radial incision is made through the wall of an excised section of an artery, it springs open to form a 'C' shape. The angle between the radii extending from the centre of the ring to each of the tips of the open ring is known as the opening angle. In each of these cases, residual stress is generated because the stalk and artery are composed of different layers of soft tissue growing at different rates. They are subject to the constraint that each layer must remain bonded to its neighbour, so that the difference in growth rates in neighbouring regions results in local compression in one layer and tension in the other. When cut, these bodies change their configuration as the residual stresses are relieved.

Conversely, stress can influence the growth of biological tissue. Several experiments have demonstrated that organisms change the way they grow in response to changes in their mechanical environment. For example, Lamoureux *et al.* showed that axons grow longer in response to an applied tension [57]. Tissue expanders can stimulate the growth of skin by gradually stretching it over a period of weeks and are a commonly-used surgical technique of obtaining skin for grafts [108]. A further example can be seen in the heart: the growth of the chamber walls is dependent upon

its geometry and the pressure of the blood within. If the blood pressure or volume of the chambers increases then wall thickening occurs in order to maintain a constant stress on the inner surface [41]. This structural change is an underlying factor in certain health conditions, such as cardiac hypertrophy [33].

The term resorption refers to a decrease in mass of an object or region of a body, *i.e.* resorption is the opposite of growth. In living systems, growth and resorption processes drive the formation of different morphologies. It is believed that many morphologies arise due to a combination of a relatively simple set of rules for growth, and the effects of residual stress [68]. For example, the airways, plant root systems and trees are all examples of branching networks acting as transport vessels, whilst seashells and animal horns exist in many different styles, ranging from those with simple geometries, to those exhibiting complex spirals, spines, ribs and ornamentations (see Figure 1.1). Furthermore, the folding and looping patters observed in the intestines are thought to be the result of differential growth between the intestine walls and mesentery lining of the gut, as demonstrated by Savin *et al.* [83]. Certain types of climbing plant achieve a helical form by undergoing non-uniform growth in their cross-section, in response to contact with a rigid support [53] (see Figure 1.2). Thus, changes in the growth laws or mechanical properties of a tissue may have a significant impact on the resulting morphology, and hence, functionality of a body. In the case of arteries, abnormal growth processes can lead to tortuosity in vessels [52, 35], whilst abnormal brain development may result from the soft brain matter growing at a faster rate than the surrounding skull. This difference imposes a geometric constraint on the brain, which results in it becoming compressed. A similar issue occurs if the brain tissue swells, due to a trauma, such as impact during a car crash.

(a) Kudu horns (b) Seashells

Figure 1.1: The elaborate geometries of seashells and animal horns can be explained by relatively simple models of growth. *Figure credits: (a): By Tamar Assaf (Own work) [Public domain], via Wikimedia Commons. (b): "Shells of marine Mollusc1" by Brocken Inaglory - Own work. Licensed under CC BY-SA 3.0 via Wikimedia Commons - http://commons.wikimedia.org/wiki/File:Shells_of_marine_Mollusc1.jpg.*

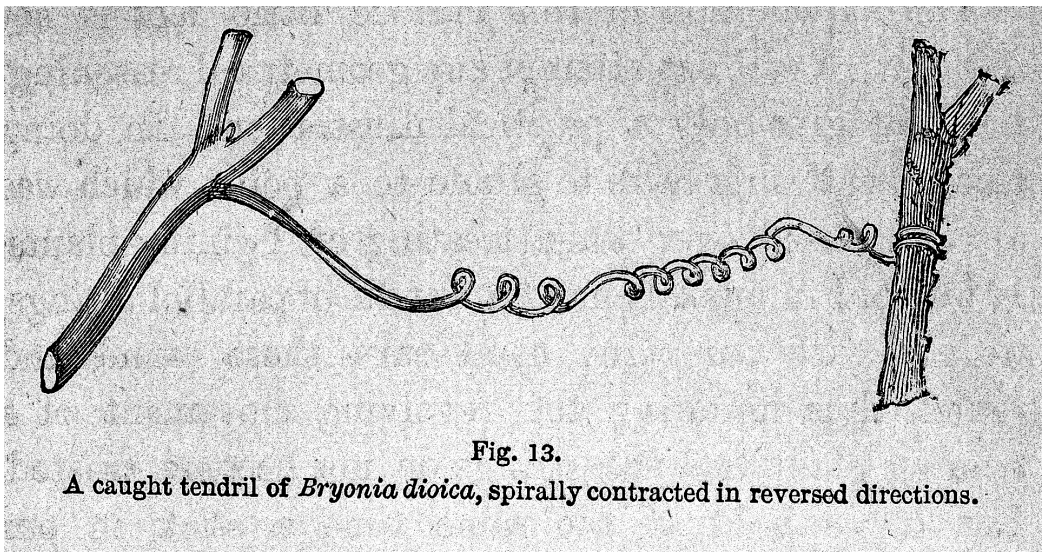

Figure 1.2: The helical form of many climbing plants is achieved via a process of non-uniform growth in the stem. *Figure credit: "C. Darwin, The movements...climbing plants. Wellcome L0028188" by Wellcome Library, London - Licensed under CC BY 4.0 via Wikimedia Commons.*

1.1.2 Multiple Layers

In many cases, it is not just growth that is non-uniform within a structure. Many tissues are made up of several different layers, each with its own material properties. For example, arterial walls consist of three concentric layers: the intima (innermost layer), the media and the adventitia (outermost layer) [47]. It is the combination of the growth and mechanical properties of each layer that allows arteries to function efficiently. Changes in the material properties of a single layer can have important consequences. For example, aneurysms are characterised by swelling or bulging of a section of the arterial wall, due to a weakening of connective tissue. If left untreated, they may increase in size, until the wall ruptures, causing internal bleeding. Individuals with Marfan Syndrome are particularly prone to aortic aneurysms, because the disease affects the elastic properties of connective tissue throughout their bodies.

Another disease affecting the arteries is atherosclerosis. In healthy arteries, the intima is very thin and makes little contribution to the mechanical properties of the vessel. A key feature in the transition of a healthy artery to one that exhibits signs of atherosclerosis [71] is the deposition of plaque on the inner walls, which leads to a build-up of lesions inside the arteries and an overall thickening and stiffening of the intima. Over time, these lesions may become unstable, causing arterial rupture, blood clots and restricted blood flow. The ability to model accurately the development of such diseases and understand their mechanical basis may allow clinicians to decide when to intervene surgically or predict the susceptibility of a patient to them.

The presence of multiple layers of tissue in a body is not only useful for maintaining structural integrity. One question at the forefront of current research in biomechanics is that of mechanotransduction (see, for example, the discussion in [3]); how do living organisms and cells obtain, interpret, and respond to information about their mechanical environment? There exist many different types of mechanoreceptors, but several utilise a layered structure, including vibrissae and Pacinian corpuscles [16]. Vibrissae

are more commonly known as whiskers and are an anatomical feature of many mammals. They consist of three layers: the innermost layer is called the medulla, which comprises relatively large, loosely connected cells. The middle layer is the cortex and consists of keratin fibres oriented along the length of the fibre. Finally, the outer layer is known as the cuticle, a thin, hard shell. It is generally understood that the primary role of whiskers is sensory; each vibrissa is anchored at one end to the face of an animal by a specially adapted follicle that incorporates a blood sinus. When the fibres are mechanically deformed, vibrations are detected by hair follicles endowed with rich nerve supplies. However, it is not well-understood what the specific role of each layer is. Pacinian corpuscles are found in the skin of humans and other mammals and consist of alternating layers of fluid and elastic lamellae, surrounding a central nerve fibre. When subject to mechanical deformation, it is believed the layers undergo oscillations that are detected by the fibre, but the structure acts as a mechanical filter so that the corpuscle is sensitive only to certain types of deformation [91, 59]. However, the exact mechanism of mechanotransduction is not fully understood and greater understanding of this phenomenon could have wide-ranging applications in medicine, engineering and physics.

There are also several examples of dynamical problems in which the presence of multiple layers is important. The tongue of the chameleon (as well as certain species of salamander) is used for prey capture. The structure of the tongue consists of a rigid cartilage skeleton connected to an accelerator muscle via layers of elastic sheaths containing helically-wound collagen fibres. This structure allows the muscle to slide easily along the skeleton. The tongue is capable of very rapid extension: depending on the species, it can extend up to twice the chameleon's own body length in approximately 20ms [19]. As we will demonstrate later, residual stress plays an important role in achieving such high-powered acceleration.

A further example of the role of multiple layers in dynamical problems is that

Figure 1.3: A three-horned chameleon *(trioceros jacksonii)* shooting its tongue. The acceleration is rapid. *Figure credit: By Whileexist (Own work) [Public domain], via Wikimedia Commons*

of seed and pollen dispersal in certain species of plant, including *arabidopsis*, and *impatiens capensis*. Here, the grains of pollen, or seeds develop inside sealed pods. Upon maturity, growth and resorption processes in the various layers of the pod walls generate residual stresses, which increase in magnitude until the pods rupture and the particles are catapulted far from the plant. This process is known as dehiscence (see [42] and references therein).

1.1.3 Other Features

In addition to growth processes, residual stress and the existence of multiple layers, there are several other hallmarks of soft tissue that affect its mechanical behaviour. We briefly describe them here and give examples of systems in which they are present.

- **Incompressibility** – One of the most commonly adopted assumptions of soft tissue is that it is close to incompressible, mainly because of its water content. During any deformation of an incompressible body, material elements do not change in volume. Consequently, the range of deformations that the body is able to undergo is restricted. For example, if a cube made of incompressible material is stretched in one direction, it must contract in at least one other

direction to satisfy this material constraint.

- **Anisotropy** – Anisotropy is the tendency of a material to respond differently to loads applied in different directions. Soft tissues usually exhibit anisotropy due to the presence of embedded fibres, such as elastin, collagen and muscle fibres. For example, airways and arteries contain families of helically-arranged fibres in their walls, which help to regulate the shape and size of the vessels. Fibres are not necessarily uniformly aligned in one (or even two) direction(s); it is common to observe a distribution of fibres in all directions, with the anisotropic effect arising from some directions being more 'preferred' than others. However, in some cases the degree of uniformity in fibre arrangement is very high (see Figure 1.4).

- **Active Stress** – Processes occurring within an elastic body can generate stresses, which are known as active stresses. Perhaps the most common examples of bodies that are able to generate active stresses are muscles. Muscle tissue is endowed with fibres that are able to contract and relax, thereby inducing a change in their length. The resulting stress can induce deformations in a body in the absence of external tractions or body forces. For example, the presence of contractile tissue in the walls of the heart chambers is essential to induce a blood flow through the circulatory system. Coughing is induced by muscle contraction and is necessary to remove obstructions from the airway, whilst peristaltic waves of muscle contraction are used to transport food through the digestive system.

- **Remodelling** – Remodelling describes changes in the mechanical properties of a body, such as its stiffness, strength or the orientation of its fibres [3]. Like growth, remodelling processes arise due to changes in the microstructure of a material, but unlike growth, they do not change the overall mass of the body.

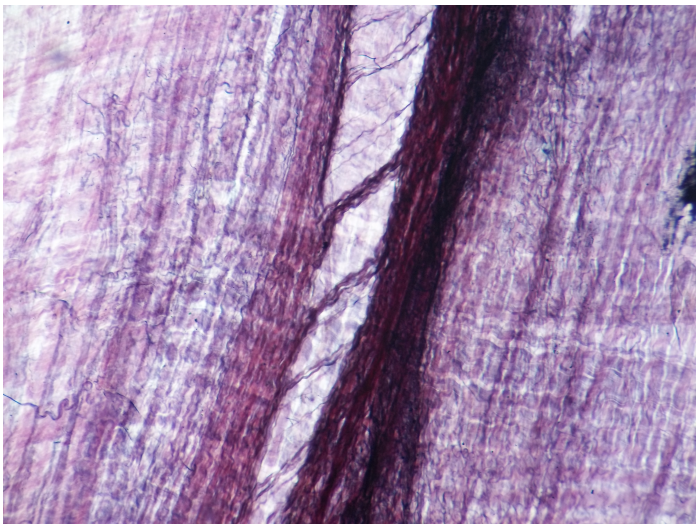

Figure 1.4: Stained section of an excised aponeurosis showing two families of collagen fibres aligned in two roughly perpendicular directions. The upper layer is torn, making it easier to see the fibres beneath. Note the high degree of uniformity in the fibre alignment in each layer. *Figure credit: By Ganmedes (Own work) [CC BY-SA 3.0 (http://creativecommons.org/licenses/by-sa/3.0)], via Wikimedia Commons.*

Bone tissue is constantly subject to remodelling processes, which replace old and weakened sections of bone with new, strong tissue, and respond to the mechanical demands of the body [82]. In humans the turnover of bone tissue is around 10% per year. Collagen fibres are known to reorient in response to mechanical loading such that they prefer to align with the direction of greatest stretch [62]. Airway remodelling is believed to be linked to asthma, by influencing the critical internal pressure at which the airway wall buckles and the number of folds that exist in the vessel wall once the instability develops [66]. We do not focus directly on the mechanisms of remodelling in this thesis, but since growth and remodelling are so closely related it is important that the effects of remodelling, such as changes in fibre angles and material parameters can be incorporated into biomechanical models.

1.2 Cylindrical Structures

In the previous section, among the various features of biological tissue, we discussed some of the complex geometries that exist in the natural world. However, it is also important to note that many of the examples referred to are geometrically similar. Arteries, airways, intestines, plant stems and the tongue of the chameleon, among others, all have an approximately cylindrical form on a relatively small scale, whilst on a larger scale their shapes are more complex (*i.e.* their cross-sections are roughly circular or annular). A summary of the geometric and mechanical features of each example (and others) is given in Table 1.1.

The development of accurate models of biological, cylindrical structures is therefore highly desirable, because a single, general modelling framework could have useful applications to a wide variety of biological systems, at various length scales. This issue is a clear motivation for the work detailed in this thesis: our goal is to contribute towards the development of such a framework. We do so through the study of several different biomechanical problems, focussing on those with a cylindrical form. Cylinders are appealing structures to study because, as we will see, it is easy to describe their geometric form and and mechanical behaviour. Moreover, cylindrical structures are widely found throughout the natural world, so mechanical models of cylindrical bodies have many applications. Before outlining these problems, we summarise previous research in the field of growth and soft tissue modelling and highlight the areas we aim to build upon in the following chapters.

1.3 Modelling Approaches

Biological growth has been the focus of much research for hundreds of years. One of the pioneers of mathematical modelling of biological structures was D'Arcy Thompson, who, in 1917, published the seminal work "On Growth and Form" [94]. In this

System	Structure	Description	Environment & Material Properties	Typical Young's Modulus	Typical Dimensions
Arteries	3 layers	Intima - thin layer of epithelial cells. Media - smooth muscle cells and helically oriented fibrous tissue. Adventitia - thick bundles of wavy collagenous fibrils.	Highly anisotropic due to helical fibres. Exhibit strain stiffening behaviour. Subject to residual stresses and normal loading *in vivo*.	Media: 9kPa, Adventitia, 0.9kPa (for small deformation) [47].	$R_1 = 0.71$mm, $R_2 = 0.97$mm, $R_3 = 1.10$mm (rabbit carotid artery, thickness of intima assumed to be negligible) [47].
Airways	3 layers	Thin layer of epithelial cells lying on a basement membrane. Smooth muscle layer. Loose connective tissue and cartilage ribs in larger vessels.	Exhibit anisotropy and strain-stiffening properties. Subject to residual stresses and normal loading *in vivo*.	Mucosa: 80kPa (circumferential), 150kPa (axial) [54, 77]. Smooth muscle with cartilage: 75kPa (circumferential), 75kPa (axial) [77].	$R_1 = 0.175$cm, $R_2 = 0.189$cm, $R_3 = 0.206$cm (human bronchus) [9, 90].
Plant stems	2 layers	Thin outer shell containing more compliant foam core. Core may fill entire shell or have a hollow centre.	Subject to axial compression and bending moments.	Shell: 60-100MPa, Core: 3-5MPa [30, 55].	$R_1 = 0.285$mm, $R_2 = 0.934$mm, $R_3 = 0.97$mm (*Elytrigia repens*) [55].
Quills and spines	2 layers	Thin outer shell containing more compliant foam core. Core usually fills shell but sometimes has hollow centre. Radial and longitudinal stiffeners may also be present.	Subject to axial compression and bending moments.	Shell: 1-4GPa, Core: 15.6-62.4MPa [30, 55].	$R_1 = 0$mm, $R_2 = 0.842$mm, $R_3 = 0.89$mm (*Erethizon*) [55].
Axons	2 layers	Nerve fibre wrapped in sheets of myelin.	Highly anisotropic due to arrangement of cytoskeleton [31].	Fibre and myelin: 12kPa [10].	$R_1 = 0\mu$m, $R_2 = 2.1\mu$m, $R_3 = 3.2\mu$m (Human adult sural nerve) [86].
Chameleon tongues	3 layers	Rigid entoglossal process connected to a cylindrical accelerator muscle and 'retractor complex' via thick connective tissue (intra-lingual sheaths). These contain collagen fibres in helical arrangements.	Anisotropic. 'Pre-firing' configuration is highly stressed.	Unknown - not found in literature.	$R_1 = 0$mm, $R_2 = 0.635$mm, $R_3 = 1.43$mm $R_4 = 1.5$mm (*Chamaeleo jacksonii*, retracted configuration) [105, 18].
Microtubules	1 layer	Tubulin polymers embedded in elastic cytoplasm.	Effectively isotropic. Subject to dynamic instability (polymerisation and depolymerisation processes) and exhibit buckling when they reach the cell membrane.	0.6GPa [84].	$R_1 = 8.4$nm, $R_2 = 10.05$nm [84].
Whiskers	3 layers	Medulla - innermost layer consisting of large, loosely-connected cells. Not always present in hair shaft. Cortex - keratin (usually α-keratin) strands lying along the axial direction of the hair. Cuticle - hard layer of overlapping cells, usually 5-12 cells thick.	Anisotropic filaments. Anchored by a follicle at one end and tapered at the free end.	3.1-3.9GPa (rat) [46]	$R_1 = 0\mu$m, $R_2 = 5\mu$m, $R_3 = 33\mu$m, $R_4 = 39\mu$m (*rattus norvegicus* B2 vibrissa) [103].
Gastrointestinal Tract	4 layers	Mucosa - epithelial cells, connective material and smooth muscle cells. Submucosa - Dense connective tissue containing blood vessels and nerves. Muscularis externa - helically aligned muscle cells. Adventitia - connective tissue.	Subject to residual stresses and normal loading *in vivo*.	Mucosa-submucosa layer: 170.5kPa (axial), 4.93kPa (circumferential). Muscle layer: 142.9kPa (axial), 0.89kPa (circumferential) [40].	$r_1 = 0.5$mm, $r_2 \approx 0.68$mm, $r_3 = 1$mm (rat oesophagus, two-layer model consisting of mucosa-submucosa layer and smooth muscle-adventitia layer) [22].

Table 1.1: Summary of properties and typical parameter estimates for various cylindrical structures. The parameters R_i, $i = 1, 2, 3, 4$ denote tissue boundaries in configurations that are traction-free, whilst r_i denote tissue boundaries in a physiological regime.

book, he considered a wide variety of problems, ranging from the shapes of different animals, to cellular mechanics, to the mechanical efficiency of skeletons. He also noted that growth is a complex phenomenon and speculated that differential growth is an essential tool in driving morphogenesis. Indeed, growth processes are driven primarily by biochemical factors and occur at the cellular level, therefore growth can be viewed as a local phenomenon [1]. However, the purpose of biological growth is to achieve a particular form, such as an insect's wing, a human's heart or the stalk of a plant. The length scale of a tissue or organ is of a greater order of magnitude than its constituent cells and molecules and applied stresses generally act on the whole surface of a body, rather than a localised region. This fact leads to the question of how growth occurring on a local level is able to generate form or pattern on a global scale, a phenomenon known as emergence. Moreover, the timescales of growth and the elastic response of a material can be vastly different; the timescale of biological growth can range from hours to months or years, whilst elastic processes can occur in under one second. Thus, biomechanics is truly a multiscale discipline, and this issue gives rise to the additional question of how one can best represent the growth and elasticity of a body mathematically. This question has previously been studied using a number of different modelling approaches, which we now discuss in more detail.

1.3.1 0-D Theories

One approach is to use discrete mechanical models of growth, whereby a material body is represented by a collection of individual units or cells, which evolve according to a set of rules. Such models have their roots in the work of von Neumann in the 1940s, and were popularised by Conway in 1970 with the development of the *Game of Life* [27]. The game has the form of a 2-D grid seeded with an initial population. At each discrete time step, every member updates its state according to the state of its neighbours, with each rule intended to represent a biological event: death from

overpopulation, continuation of life, reproduction and death from underpopulation. This original model has been adapted in many ways, including the introduction of different types of individual, the use of different spatial domains and incorporation of various other biological processes, such as diffusion of nutrients through the domain. In the early 1990s, the Cellular Potts model (CPM) was introduced by Glazier and Graner [38], in which cells are assumed to be deformable objects. Updates are first proposed and then either accepted or rejected with a certain probability, depending upon a Hamiltonian. The form of this Hamiltonian is based upon the interactions of cells with their surrounding environment and their own shape and size.

Other types of discrete model include off-lattice models. These treat the spatial domain as a continuous medium, with individuals represented by 2-D or 3-D shapes [48, 12, 23]. Off-lattice models fall into two categories: centre-based and vertex-based models. In centre-based models, individual cells are represented by polygons or polyhedra surrounding a central point, with cell boundaries defined by the bisectors of neighbouring points. This division of the domain is known as a Voronoi tessellation. Other examples include the representation of cells as overlapping spheres [76], where the degree of interaction between different cells is related to their degree of overlap. In vertex-based models, we specify the location of the vertices at which cell boundaries meet and allow these to move, as opposed to the centres. In either case, mechanics such as cell-cell interactions and external tractions, as well as rules for nutrient diffusion, chemical signals and individual cell behaviour can be easily specified, and incorporated into robust computational frameworks [78].

Discrete models offer a convenient means of incorporating many biological features into growth problems and observing the effects of small-scale processes at a tissue level. The main drawback of such approaches is that as the number of individuals increases, so does the computational complexity of the model, so that modelling large populations can be extremely slow. Moreover, it is difficult to carry out mathematical

analysis of the governing equations, so it is difficult to determine the key biological, physical or chemical processes that drive a system and to identify emergent features from the underlying rules.

1.3.2 Continuous Theories

The alternative to using a discrete approach to model growth is to treat the population of individuals as a continuous medium. Rather than accounting for the growth and mechanical behaviour of each cell, these quantities are averaged over the entire population to gain a tissue-level response. In other words, the population behaves as a single, deformable body. A deformation is modelled as a bijective mapping of the body from an initial configuration to a deformed, or current configuration. The well-established theory of 3-D elasticity is a natural choice for modelling elastic solids, and has roots in the pioneering work of Mooney and Rivlin in the 1940s [64, 80], as well as Truesdell and Noll in the 1960s [96]. In the 1980s, Skalak and others built upon these ideas by proposing a kinematic description of growth within this framework [89]. This idea led to the theory of morphoelasticity, with Rodriguez *et al.* establishing the idea of decomposing a deformation into two stages [81]. Firstly, each material point undergoes some prescribed stress-free growth. In the absence of any stress, the growth step could result in a body in which different regions intersect one another or voids exist, because the growth step only changes the stress-free configuration of each local volume element. In the second stage of the deformation, an elastic response is introduced, which ensures no such regions develop, and generates stress in the body. Following the elastic response, the body occupies a global, residually-stressed state. Stresses and strains are related by a constitutive law, which encapsulates the response of the material to loading.

The framework of non-linear elasticity offers a powerful means of incorporating many mechanical effects into tissue models, and it is generally straightforward to de-

rive equations of mechanical equilibrium satisfied by the displacement field. However, these equations are intractable in all but a few simple cases. When it is possible to find an exact solution, or analytic approximation to the solution, non-linear models yield much information about the stress and strain profiles within a tissue, as well as its deformed shape. However, little can be inferred about the underlying cell biology of the system, because all the information relating to individual members of the cellular population is lost in the averaging process. Moreover, there continues to exist some controversy regarding the incorporation of growth into continuum models. Because the cellular notion of growth is missing at this spatial scale, the growth laws used are phenomenological. In fact, it may be more accurate to say that a growth law describes the *effects* of cellular growth at the tissue level, rather than describing the growth itself [4, 3]. Furthermore, if we wish to study the mechanical behaviour of a residually-stressed object then knowledge of a corresponding stress-free configuration is essential, in order for the strains in the loaded body to be measured. Finding such a configuration may not be possible. Nevertheless, non-linear models remain a popular choice for many studies of biological growth, because of their wide applicability and well-founded mathematics.

In the case of small strains, the theory of non-linear elasticity can be simplified to linear elasticity. Here, it is assumed that the stresses are linear functions of the strains, with the material properties captured by two constants known as the *Lamé parameters*. Moreover, there is no distinction between the initial and current configurations. These simplifications allow a wider range of problems to be easily studied than with the non-linear theory because the form of the equilibrium equations are more analytically tractable. However, the reliability of the theory is decreased as larger deformations are considered.

Other 3-D approaches to soft tissue modelling include mixture theory and multiphase theory. In mixture theory, a region of tissue is represented by a superposition of

different components. For example, if the material is fibre-reinforced, one component is used to represent the isotropic matrix, with another component used to represent the fibres. Each component has its own stress-free configuration, so that it is possible for the unloaded body to exhibit material stress, if the stress-free configurations of each phase differ from one another [15]. In poroelastic or biphasic models, a region of tissue is considered to be composed of an elastic component, representing the solid fraction of the tissue and a viscous component, representing the interstitial fluid [58]. An extension to this theory is triphasic mixture theory, in which the fluid component is assumed to be ionic, with the soluble ions represented by a third phase. These approaches tend to lead to large systems of equations, but they have the advantage that they incorporate more biological information into the modelling framework.

1.3.3 Computational Techniques

It is often possible to overcome some of the limitations of continuous frameworks using numerical techniques. Finite element methods (FEMs) are often used to solve complex boundary value problems. Here, the domain of interest is approximated by generating a mesh of nodes and edges, which discretise the domain. Instead of a continuum, a body is represented by an arrangement of polygons (in 2-D) or polyhedra (in 3-D), known as elements. The governing equations are also discretised and it is assumed that the solution in each element is given by a linear combination of basis functions. Although rigorous mathematical analysis is not always feasible, FEMs are useful for carrying out simulation studies and validating analytic models. Advances in imaging technology in recent decades have yielded high resolution meshes of body tissues, which have allowed for patient-specific studies to be carried out. However, as in the case of discrete models, the computational complexity of solving the discretised equations grows non-linearly with the size of the mesh, so the time taken to process high resolution data can become large if the processing power of a computer is limited.

1.3.4 1-D and 2-D Theories

In certain cases, a full 3-D formulation of growth and elasticity may not be required. If we consider thin surfaces, such as a plant leaf, or slender structures, such as a neuron or a vine, most of the geometric information of the structure is encoded in the mid-surface or centreline respectively. This observation allows specialised theories to be utilised, including non-linear plate theory and Kirchhoff rod theory, which date back to classic problems, such as Euler's bending of a beam [21]. The main advantage of such theories is that they are, in general, more analytically tractable than the full theory of finite elasticity; and, unlike linear elasticity, they can be used to study arbitrarily large deformations. This tractability allows for investigation of more geometrically-complex problems than the case of the full 3-D theory. Recent advances in these models have included the inclusion of growth processes, giving rise to the theory of morphoelastic rods and elastic models of accretion [89, 68]. Here, the notion of decomposition of the deformation in the non-linear framework is replaced by a space curve parametrised in terms of one of three possible arc lengths: initial, grown and current. The main drawback of this approach is that the mechanical description of the body is less sophisticated than the full 3-D approach. Additionally, care must be taken to avoid problems such as self-intersection, which may arise as a direct consequence of using a 1-D model of a 3-D physical system.

1.3.5 Applications

As mentioned above, many applications of mechanical models in biology relate to disease treatment or prevention, since many diseases are mechanical in nature. For example, malignant tumours are the result of unregulated cell growth. If left untreated, they can lead to death simply by increasing in size and applying pressure to surrounding tissues and organs, causing them to fail. Cellular Potts models have remained popular since their introduction, with variations of the model used to describe

many growth problems, including tumour growth, wound healing and morphogenesis [93, 87]. Traumatic injuries, such as those experienced in a car accident, can have a similar effect, by causing tissues to swell, albeit on a much shorter timescale than the growth of a tumour. This swelling not only increases the pressure on the surrounding region, but also damages the swollen region of tissue by placing it under large strain. In the case of brain swelling an extra consideration is the presence of the rigid skull, which restricts the space the brain is able to occupy. Multiphase methods are particularly useful for modelling problems of this type because the swelling is caused by an increase in the fluid fraction of the tissue [20], which can easily be accounted for in these approaches.

Non-linear elasticity has been applied to a large variety of physiological scenarios, especially those involving cylindrical geometries. In 2000, Holzapfel *et al.* developed a constitutive model for arterial walls [47], which was later extended to include the effects of fibre dispersion [28]. This type of model has since been used in many studies of arteries (e.g. [56, 79]). Moulton and Goriely investigated the possible role of airway growth and remodelling in the onset of chronic asthma by examining cross-sectional growth in a two-layer cylinder [67]. In the case of more complex geometries, such as the heart, much work has been done to develop computational software for modelling various conditions, such as stress-dependent growth and fibrillation [78].

Outside the field of medicine, plants provide a rich and diverse source of mechanical problems. Plant stems fulfil a number of important roles, including supporting the leaves and flowers and acting as transport vessels for nutrients and water. They must be able to fulfil these roles whilst maintaining their structural integrity against many types of mechanical load, including being blown by the wind and stepped on by animals. Previous research has examined how certain plant species may employ growth and remodelling processes to adapt to their mechanical environment. In the case of flowering plants, studying the growth of flower petals could give insight into

how complex morphologies may emerge from relatively simple underlying growth processes. For example, Ben Amar *et al.* used a surface-growth approach to investigate the shapes of certain types of flower petals [2]. Similarly, Moulton *et al.* investigated the morphology of seashells by considering simple growth laws of a 2-D surface and demonstrated that local growth rules could accurately reproduce the somewhat complex shapes of many different shells [68], whilst Goriely and Neukirch investigated the coiling of vines around tree-trunks, as in Figure 1.2 [37].

These examples demonstrate the importance of using mechanical models to investigate biological problems. They provide clinicians with insight into disease prevention and treatment, and offer inspiration to engineers working on similar problems in industry. One key challenge is to develop modelling frameworks that can accurately model the behaviour of residually-stressed, multi-layered tissues subject to geometrically complex deformations. In this thesis, our goal is to work towards the development of such frameworks by focussing on filamentary structures, which are ubiquitous throughout the biological world.

1.4 Motivation and Aims

In summary, we have identified a clear need for accurately modelling the mechanical behaviour of soft tissue. Formulating mechanical models to describe biological structures is challenging, for several reasons: the non-trivial interplay between growth and stress, the existence of complex morphologies and the properties of the constituent material, such as incompressibility, strain-stiffening behaviour and anisotropy. In the case of filamentary structures, progress can be made, because they can be idealised as cylindrical bodies, which reduces the geometric complexity of the problem. Our interest lies in characterising the effects of growth and residual stress on the mechanical behaviour of cylinders, so it is natural for us to use continuum models. The theory of

3-D elasticity is able to capture effectively the mechanical features of a body, but is essentially restricted to simple geometric problems, whilst rod theory is able to describe geometrically complex deformations, but much of the mechanical description of the body is lost. The specific aims of this thesis are to work towards a mapping between 3-D, non-linear elasticity and rod theory. That is, we use non-linear elasticity to determine the effective mechanical properties of residually-stressed cylindrical bodies and use these properties to inform the constitutive laws of an analogous rod theory approach. The result is an effective rod, which is able to undergo geometrically complex deformations, whilst retaining some of the information about the residual stress profile in the 3-D cylinder. Furthermore, we aim to gain insight into the influence of differential growth and residual stress on the mechanical properties of both single-layered and multi-layered filaments. We do so by applying the 3-D framework to a real-world problem: the tongue of the chameleon. This is an ideal system to study because it is cylindrical in form, consists of multiple layers of tissue and each layer contains reinforcing fibres. The outermost region is muscular, so it is also possible for the tongue to generate active stress. The exact mechanism of tongue projection is not yet known for certain, but there exists much experimental evidence relating to the dynamics of projection and anatomy of the tongue [7, 18, 43, 105]. Therefore we have an organism that allows the development and testing of a mechanical model, which could provide information about the various roles of each feature of soft biological tissue.

1.5 Thesis Outline

The structure of this thesis is as follows: in Chapter 2, two of the modelling approaches described above are introduced in greater detail. These are the theory of 3-D non-linear elasticity for an arbitrary hyperelastic body, and the theory of elastic rods. As

we have discussed, both are well-developed frameworks that have been widely used in many biomechanical problems. We give examples of common choices of strain-energy density used in existing literature and also give details of incremental deformations, which allow the investigation of the stability of a particular configuration.

In Chapter 3, we study the effect of differential growth in a one-layer cylinder. Using a range of simple growth laws, representative of those observed in biology, we develop an initial method for deriving effective stiffnesses of an isotropic cylinder subject to differential growth. We use the theory of 3-D elasticity detailed in Chapter 2 to determine these stiffnesses and introduce a means of mapping them into the constitutive laws of an analogous rod theory model. To do so we derive the equations of static equilibrium for an isotropic, incompressible cylinder. The mapping constitutes an initial step in working towards a general correspondence between 3-D elasticity and rod theory and allows us to account, in some way, for the effects of residual stress in rod theory problems.

In Chapter 4, we also focus on mapping between 3-D and rod theory models. Here, we turn our attention to the behaviour of an elastic filament embedded in a surrounding matrix and its stability under the effects of constrained axial growth. When the outer layer is sufficiently thick it can be thought of as an elastic foundation, which transversely reinforces the inner layer. However, it is difficult to relate the degree of reinforcement, usually encapsulated in a foundation modulus parameter, to the material properties of the outer layer. The objective of this chapter is to obtain an analytic estimate of this foundation modulus in terms of the directly measurable properties of the system.

In Chapter 5 we apply the theory of 3-D elasticity to an intriguing case-study. Here, we examine the projection of the chameleon's tongue. The tongue constitutes an ideal problem for us to investigate, because it can be approximated as a cylinder, consists of multiple layers of tissue, is endowed with reinforcing fibres and exhibits

residual stress. It is also capable of rapid acceleration: during projection it can extend up to twice the chameleon's body length in under 10ms. In the 19th and 20th centuries, various theories were proposed as to how this acceleration is achieved. In 2004, histological studies and experimental investigations carried out by de Groot and van Leeuwen [18] led to the proposition that this high-power acceleration is achieved via an energy storage-and-release mechanism, similar to a catapult. However, until now this proposal is yet to be understood from a mathematical point of view. Specifically, there has been much debate surrounding the question of what provides the energy that is required for high-power projection. We construct a simple mechanical model of the tongue and use it to study the kinetic energy available during projection arising from the soft tissue components of the tongue. In particular, we consider its performance in the case that the system is stress-free prior to muscle activation and compare this case to that in which the elastic sheaths are mechanically loaded.

Finally, we summarise our findings in Chapter 6 and discuss open problems and potential avenues for future research in this field.

Chapter 2

Mathematical Models of Elasticity

In this chapter we introduce the modelling frameworks that will be of use throughout the remainder of this thesis. We first give details of the general theory of non-linear elastic deformations, followed by the theory of elastic rods. In the following chapters these results will be applied in a variety of scenarios involving elastic cylindrical structures.

2.1 3-D Elasticity Approach

2.1.1 Kinematics

We follow closely the method outlined in [8]. We consider an elastic body occupying a reference (stress-free) configuration, $\mathcal{B}_0$, with a material point in $\mathcal{B}_0$ represented by the vector $\mathbf{X}$, where

$$\mathbf{X} = X_1\mathbf{E}_1 + X_2\mathbf{E}_2 + X_3\mathbf{E}_3, \tag{2.1}$$

and $\{\mathbf{E}_1, \mathbf{E}_2, \mathbf{E}_3\}$ is an orthonormal basis defined with respect to the reference configuration. We call this the Lagrangian, or reference, basis. The body is subject to a deformation, $\boldsymbol{\chi}(\mathbf{X};\ t)$, which maps each point in $\mathcal{B}_0$ to a point in a new configuration, $\mathcal{B}_f$, which we refer to as the current configuration. The image of $\mathbf{X}$ in $\mathcal{B}_f$ is denoted

by

$$\mathbf{x} = \boldsymbol{\chi}(\mathbf{X};\ t) = x_1\mathbf{e}_1 + x_2\mathbf{e}_2 + x_3\mathbf{e}_3, \tag{2.2}$$

where $\{\mathbf{e}_1, \mathbf{e}_2, \mathbf{e}_3\}$ is an orthonormal basis defined with respect to the current configuration. We call this the Eulerian, or current, basis. The deformation gradient tensor is denoted by $\mathbf{F}$ and describes the transformation of a line element, $\mathrm{d}\mathbf{X}$, passing through $\mathbf{X}$ in the reference configuration into the line element $\mathrm{d}\mathbf{x}$, passing through $\mathbf{x}$ in the current configuration. It is defined to be

$$\mathbf{F} = \mathrm{Grad}\ (\boldsymbol{\chi}) = \frac{\partial \mathbf{x}}{\partial \mathbf{X}} = \frac{\partial}{\partial X_j}(x_i\mathbf{e}_i) \otimes \mathbf{E}_j, \tag{2.3}$$

where we use the Einstein summation convention on the indices i and j.

As described in Chapter 1, the effects of growth are incorporated into the model via multiplicative decomposition of the deformation gradient tensor, so that

$$\mathbf{F} = \mathbf{A}\mathbf{G}, \tag{2.4}$$

where $\mathbf{G}$ represents local stress-free growth and $\mathbf{A}$ represents an elastic response. This is illustrated in Figure 2.1. The growth tensor is usually represented as follows

$$\mathbf{G} = \mathrm{diag}\ (\gamma_1, \gamma_2, \gamma_3)\,, \tag{2.5}$$

where the diagonal components, $\gamma_i,\ i = 1, 2, 3$, represent the growth occurring in the directions of the reference basis vectors. For example, in cylindrical polar coordinates, $\gamma_i,\ i = 1, 2, 3$ denote the growth of a material element in the radial, circumferential and axial directions respectively. This is illustrated in Figure 2.2. If $\gamma_i > 1$ then we observe an increase in size in the i^{th} direction, whilst if $\gamma_i < 1$ the material shrinks in the i^{th} direction. During the growth step, volume elements may change in size, giving rise to a resultant configuration that is not necessarily physically possible, *i.e.* $\mathbf{G}$

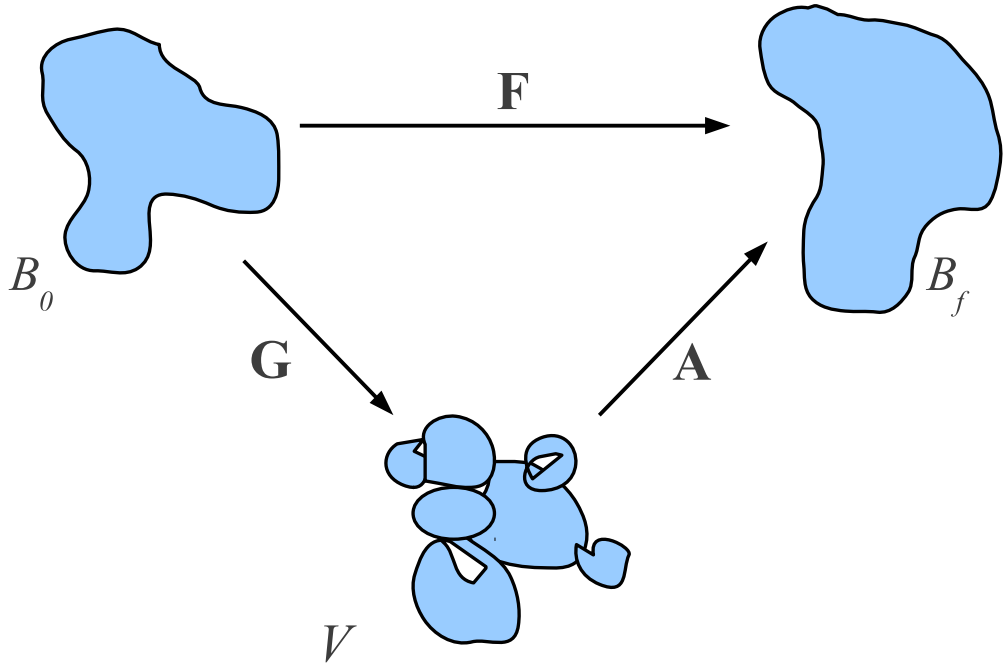

Figure 2.1: Decomposition of a deformation into two stages. In the first stage, each material point undergoes stress-free volumetric growth, which is assumed to depend only upon the reference geometry, $\mathbf{X}$. However this does not, in general, correspond to a compatible deformation, since neighbouring regions may encroach on one another, or voids may be created. This is represented by a virtual configuration, $\mathcal{V}$. During the elastic response step the grown volume elements in $\mathcal{V}$ are 'reassembled' into a new configuration $\mathcal{B}_f$. This elastic response generates residual stress, which is necessary if we are to maintain compatibility of the overall deformation from $\mathcal{B}_0$ to $\mathcal{B}_f$.

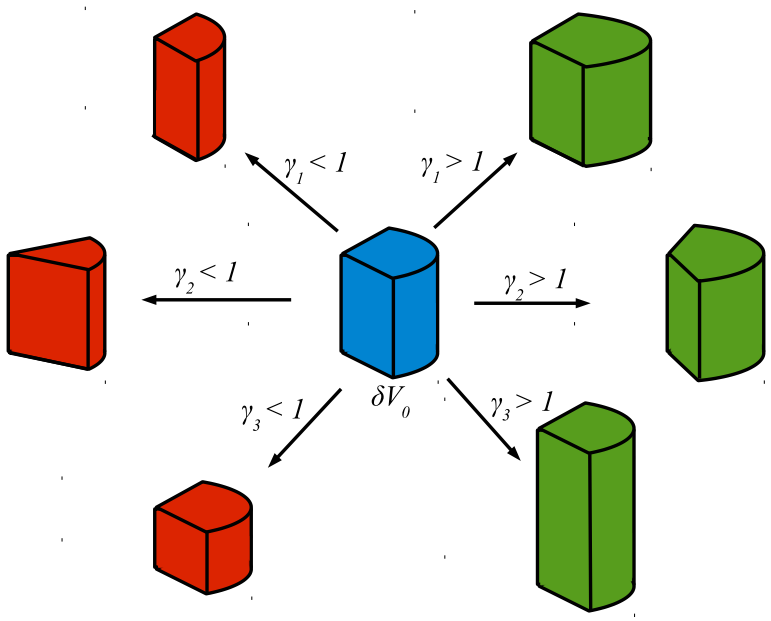

Figure 2.2: Interpretation of the components of the growth tensor, $\mathbf{G}$, for a small volume element, δV_0 of a cylinder. If $\gamma_1 > 1$ we have growth in the radial direction, whilst if $\gamma_1 < 1$ we have resorption in the radial direction. The same is true for γ_2 (circumferential direction) and γ_3 (axial direction).

does not correspond to a compatible deformation. In order to achieve a compatible deformation, internal stresses may be generated to ensure the grown body does not self-penetrate or develop voids. The elastic response, $\mathbf{A}$, accounts for any stress arising from the incompatibility of the growth step, as well as any applied loads or body forces. If no external loads or moments are applied, we refer to the resulting configuration as unloaded. It is not necessarily stress-free, since residual stresses may exist due to incompatible growth. From the elastic response tensor, we derive the left and right Cauchy-Green strain tensors:

$$\mathbf{B} = \mathbf{A}\mathbf{A}^T \quad \text{and} \quad \mathbf{C} = \mathbf{A}^T\mathbf{A}, \tag{2.6}$$

respectively. The eigenvectors of $\mathbf{B}$ and $\mathbf{C}$ can be interpreted as the principal directions of stretch with respect to the Eulerian and Lagrangian bases respectively and

are consequently known as the principal Eulerian and Lagrangian axes. Their associated eigenvalues, $\alpha_i^2,\ i = 1, 2, 3$, denote the square of the magnitude of the stretch in these directions and we therefore refer to $\alpha_i,\ i = 1, 2, 3$, as the principal stretches.

2.1.2 Equilibrium Equations

To study the effect of strain on an elastic body, we turn our attention to the resulting stresses induced by a deformation. First we consider the balance of linear momentum in some arbitrary region, Ω of $\mathcal{B}_f$, which yields the following equation

$$\int_{\Omega} \rho(\ddot{\mathbf{x}} - \mathbf{b})\ \mathrm{d}v = \int_{\partial\Omega} \mathbf{t}\ \mathrm{d}a, \tag{2.7}$$

where ρ denotes mass density, $\mathbf{b}$ denotes the external resultant body force per unit mass acting on Ω, and $\mathbf{t}$ represents surface tractions per unit area, which arise due to contact with the surrounding medium. Appealing to Cauchy's stress theorem and the divergence theorem, we are able to localise (2.7) (under the standard assumptions of arbitrary Ω and continuity of the integrand) to obtain

$$\rho\ddot{\mathbf{x}} = \rho\mathbf{b} + \mathrm{div}\ \mathbf{T}. \tag{2.8}$$

The tensor $\mathbf{T}$ is the Cauchy stress tensor, whose i, j^{th} component denotes the stress acting in the i^{th} direction on a surface element in the current configuration with unit normal in the j^{th} direction. If we consider the balance of angular momentum, using a similar method we obtain

$$\int_{\Omega} \rho\mathbf{x} \wedge (\ddot{\mathbf{x}} - \mathbf{b})\ \mathrm{d}v = \int_{\partial\Omega} \mathbf{x} \wedge \mathbf{t}\ \mathrm{d}a, \tag{2.9}$$

and localising leads to the following condition on the Cauchy stress tensor

$$\mathbf{T}^T = \mathbf{T}. \tag{2.10}$$

It is also convenient to introduce the analogue of $\mathbf{T}$ defined in the reference configuration, that is the force per unit undeformed area. This is known as the (first) Piola-Kirchhoff stress tensor and is given by

$$\mathbf{P} = \mathbf{S}^T, \quad \text{where} \quad \mathbf{S} = J\mathbf{A}^{-1}\mathbf{T}. \tag{2.11}$$

The tensor $\mathbf{S}$ is known as the nominal stress tensor.

2.1.3 Boundary Conditions

On the boundary of $\mathcal{B}_f$ it is commonplace to consider two natural choices of condition: either we prescribe the displacement, so that the overall shape of the deformed body is known, or we impose a known traction or moment and solve to find the corresponding displacement. Of course, it is possible to use a combination of such conditions, so that the displacement is fixed in one region of the boundary, say $\partial\mathcal{B}_f^1$, and the loading is fixed in another region, $\partial\mathcal{B}_f^2$. For example

$$\boldsymbol{\chi} = \hat{\boldsymbol{\chi}} \quad \text{on } \partial\mathcal{B}_f^1, \tag{2.12}$$

$$\mathbf{T}.\hat{\mathbf{n}} = \hat{\mathbf{t}} \quad \text{on } \partial\mathcal{B}_f^2, \tag{2.13}$$

where $\hat{\boldsymbol{\chi}}$ and $\hat{\mathbf{t}}$ are known.

In the following chapters, various combinations of boundary conditions will be used in the context of extension-inflation problems involving elastic cylinders. In these problems, the boundary consists of up to four surfaces: the upper and lower flat ends of the cylinder and the outer and inner curved boundaries. If the cylinder is solid then

the latter does not exist. In addition if the cylinder consists of multiple layers, then there is a material boundary at some radius within the deformed configuration. Here, we must impose two matching conditions: continuity of displacement and continuity of normal stress. Note that we do not require the same of circumferential or axial stress, so they may be discontinuous across the boundary.

2.1.4 Growth Laws

In Chapter 1, we noted that growth and stress influence one another. On a microscopic level, cells grow according to their local mechanical environment, therefore as the geometry and stress profiles with an elastic body evolve, so will the growth tensor, $\mathbf{G}$, as a function of stress. In fact, in its most general form, an evolution law for $\mathbf{G}$ may be written as a function of material stress, the deformation, the growth itself and external fields, such as chemical gradients (represented by $\boldsymbol{\mu}$):

$$\dot{\mathbf{G}} = \mathcal{G}\left(\mathbf{T}, \mathbf{F}, \mathbf{G}, \boldsymbol{\mu}; t, \mathbf{x}, \mathbf{X}\right). \tag{2.14}$$

A useful discussion of evolving growth laws is provided in [101], in which a discretised version of (2.14) is used to treat growth as an incremental process. However, throughout this thesis, we will consider a simplified version of (2.14) in which the growth tensor is either constant, or dependent only upon the reference geometry. That is

$$\mathbf{G} = \mathcal{G}\left(\mathbf{X}\right). \tag{2.15}$$

This assumption allows us to treat the growth of a body as a single stage in the decomposition of the overall deformation, as depicted in Figure 2.1.

2.1.5 Constitutive Laws

To relate the deformation, $\boldsymbol{\chi}$, to the resulting stresses in a body, $\mathbf{T}$, it is necessary to prescribe a constitutive law, which captures the mechanical response of the material. We do so by introducing the scalar function W, which is known as the strain-energy density. A widely-used modelling assumption is that of hyperelasticity, whereby W depends only upon the deformation. In other words, we write

$$W = W(\mathbf{A}). \tag{2.16}$$

Consequently, it can be shown that

$$\mathbf{S} = \frac{\partial W}{\partial \mathbf{A}}, \tag{2.17}$$

where

$$S_{ij} = \frac{\partial W}{\partial A_{ji}}. \tag{2.18}$$

Alternatively, making use of (2.11)

$$\mathbf{T} = J^{-1}\mathbf{A}\frac{\partial W}{\partial \mathbf{A}}. \tag{2.19}$$

We also assume that W is objective, *i.e.* the material's properties are independent of the observer's frame of reference. This implies

$$W(\mathbf{QA}) = W(\mathbf{A}), \tag{2.20}$$

for any proper orthogonal tensor, $\mathbf{Q}$. If, in addition, the material is isotropic, then the response of the material is the same in all directions, *i.e.* there is no preferred

direction of stretch. This implies

$$W(\mathbf{AP}) = W(\mathbf{A}), \tag{2.21}$$

for any proper orthogonal tensor, $\mathbf{P}$. In this case, W depends upon the deformation $\boldsymbol{\chi}$ only through its strain invariants, which are given by

$$I_1 = \mathrm{tr}(\mathbf{B}) = \alpha_1^2 + \alpha_2^2 + \alpha_3^2, \tag{2.22}$$

$$I_2 = \frac{1}{2}\left(\mathrm{tr}(\mathbf{B})^2 - \mathrm{tr}(\mathbf{B}^2)\right) = \alpha_1^2\alpha_2^2 + \alpha_1^2\alpha_3^2 + \alpha_2^2\alpha_3^2, \tag{2.23}$$

$$I_3 = \det(\mathbf{B}) = \alpha_1^2\alpha_2^2\alpha_3^2 = J^2. \tag{2.24}$$

In such circumstances, we can use one of the following equivalent expressions for W

$$W = W(\alpha_1, \alpha_2, \alpha_3) = \bar{W}(I_1, I_2, I_3). \tag{2.25}$$

However, if the material is anisotropic, the energy required to deform a volume element varies depending on the direction of stretch. Within this thesis we shall restrict our attention to materials that have at most two preferred directions of stretch. In these cases, we use the vectors $\mathbf{M}$ and $\mathbf{M}'$ to denote the directions of preferred stretch in the reference configuration, $\mathcal{B}_0$. Then, the strain-energy density depends upon a total of eight invariants: the first three remain the same as those in (2.22)-(2.24), two further invariants depend only upon the first preferred direction, $\mathbf{M}$, another two depend only upon the second preferred direction, $\mathbf{M}'$ and the last invariant represents a coupling effect between the two directions. Explicitly, these extra invariants are given by

$$I_4 = \mathbf{M}.(\mathbf{CM}), \quad I_5 = \mathbf{M}.(\mathbf{C}^2\mathbf{M}), \tag{2.26}$$

$$I_6 = \mathbf{M}'.(\mathbf{CM}'), \quad I_7 = \mathbf{M}'.(\mathbf{C}^2\mathbf{M}'), \quad I_8 = \mathbf{M}.(\mathbf{CM}'). \tag{2.27}$$

Name	Expression
neo-Hookean	$\bar{W} = \frac{\mu}{2}(I_1 - 3)$
Mooney-Rivlin	$\bar{W} = \frac{\mu_1}{2}(I_1 - 3) + \frac{\mu_2}{2}(I_2 - 3)$
Ogden	$W = \sum_{p=1}^{\infty} \mu_p \left(\alpha_1^{\beta_p} + \alpha_2^{\beta_p} + \alpha_3^{\beta_p} - 3\right)$
Fung	$\bar{W} = \frac{1}{2\alpha}\left[e^{\alpha(I_1-3)} - 1\right]$
reinforced neo-Hookean	$\bar{W} = \frac{\mu}{2}(I_1 - 3) + \frac{\mu_4}{2}\left[(I_4 - 1) + (I_6 - 1)\right]$
Holzapfel-Gasser-Ogden	$\bar{W} = \frac{\mu}{2}(I_1 - 3) + \frac{k_1}{k_2}\sum_{i=4,6}\left(\exp\left[k_2(I_i - 1)^2\right] - 1\right)$

Table 2.1: Examples of commonly-used strain-energy densities.

For convenience we shall use the same notation $\bar{W}$ to represent the augmented strain-energy density and we write

$$\bar{W} = \bar{W}(I_1, I_2, I_3, I_4, I_5, I_6, I_7, I_8). \tag{2.28}$$

In Table 2.1, some common choices of isotropic and anisotropic strain-energy densities are presented.

For any particular choice of W (or equivalently $\bar{W}$) it can be shown that the Cauchy stress tensor, $\mathbf{T}$ can be written as

$$\begin{aligned}\mathbf{T} = {} & 2I_3^{\frac{1}{2}}\left(\bar{W}_1 + I_1\bar{W}_2\right)\mathbf{B} - 2I_3^{-\frac{1}{2}}\bar{W}_2\mathbf{B}^2 + 2I_3^{\frac{1}{2}}\bar{W}_3\mathbf{I} + 2\bar{W}_4\mathbf{m}\otimes\mathbf{m} \\ & + 2\bar{W}_5(\mathbf{m}\otimes\mathbf{Bm} + \mathbf{Bm}\otimes\mathbf{m}) + 2\bar{W}_6\mathbf{m}'\otimes\mathbf{m}' + 2\bar{W}_7(\mathbf{m}'\otimes\mathbf{Bm}' + \mathbf{Bm}'\otimes\mathbf{m}') \\ & + \bar{W}_8(\mathbf{m}\otimes\mathbf{m}' + \mathbf{m}'\otimes\mathbf{m}),\end{aligned} \tag{2.29}$$

where $\mathbf{m} = \mathbf{AM}$ and $\mathbf{m}' = \mathbf{AM}'$.

The orientation of the fibres can have important consequences on the mechanical response of a body. For example, in Chapter 5 we will demonstrate that for certain fibre angles in the muscular component of the chameleon's tongue, projection cannot

be initiated by muscle contraction. We will discuss this phenomenon in more detail later.

2.1.6 Incompressibility

In the case where the material body is subject to some constraint, $\mathcal{C}(\mathbf{A}) = 0$, then we must impose a restriction on the set of possible deformations. This is of particular relevance to our work, because in many modelling situations, biological tissue is regarded as incompressible. Therefore, the function space of $\boldsymbol{\chi}$ is limited to the set of mappings for which

$$J := \det \mathbf{A} = 1. \tag{2.30}$$

This ensures that any change in volume during the deformation occurs only due to growth; in the elastic response step, no change in the volume of material elements is permitted.

One further modification of the modelling framework is also required when a material constraint is imposed: we include an extra term in the strain-energy density so that instead of (2.16) we have

$$W(\mathbf{A}) = \tilde{W}(\mathbf{A}) - p\mathcal{C}(\mathbf{A}), \tag{2.31}$$

where p is a Lagrange multiplier associated with the constraint and $\tilde{W}$ is any strain-energy density, such as those in Table 2.1. For convenience, we will drop the $\tilde{W}$ notation and simply use W in both the compressible and incompressible cases. In the case of incompressibility, we have $\mathcal{C}(\mathbf{A}) = \det(\mathbf{A}) - 1$ and (2.17) becomes

$$\mathbf{S} = \frac{\partial W}{\partial \mathbf{A}} - p\mathbf{A}^{-1}. \tag{2.32}$$

Furthermore, substitution into (2.11) yields

$$\mathbf{T} = \mathbf{A}\frac{\partial W}{\partial \mathbf{A}} - p\mathbf{I}, \tag{2.33}$$

to give a modified expression for the Cauchy stress tensor.

2.2 Incremental Deformations

Having described the general boundary value problem corresponding to a finite deformation, it is convenient at this point to consider the stability of a given solution of (2.8). We do so by introducing a small perturbation to the finite solution. This perturbation belongs to a wider class of deformation than the finite deformation, and is defined by

$$\boldsymbol{\chi}(\mathbf{X}) = \boldsymbol{\chi}^{(0)}(\mathbf{X}) + \epsilon\boldsymbol{\chi}^{(1)}(\mathbf{X}), \tag{2.34}$$

where $0 < \epsilon \ll 1$ characterises the size of the perturbation. Here, we use the superscript $^{(0)}$ to denote the finite deformation and its associated quantities, and $^{(1)}$ to denote the incremental deformation. Accordingly, we define

$$\mathbf{F} = (\mathbb{1} + \epsilon\mathbf{F}^{(1)})\mathbf{F}^{(0)}, \quad \mathbf{A} = (\mathbb{1} + \epsilon\mathbf{A}^{(1)})\mathbf{A}^{(0)}. \tag{2.35}$$

Here, the incremental equations and boundary conditions are formulated in terms of the current configuration. We expand the Cauchy stress tensor as follows

$$\mathbf{T} = \mathbf{T}^{(0)} + \epsilon\mathbf{T}^{(1)} + \mathcal{O}(\epsilon^2). \tag{2.36}$$

Substitution of (2.36) into (2.33), under the assumption of incompressibility, gives

$$\mathbf{T}^{(0)} = \mathbf{A}^{(0)}\frac{\partial W^{(0)}}{\partial \mathbf{A}^{(0)}} - p^{(0)}\mathbb{1}, \tag{2.37}$$

$$\mathbf{T}^{(1)} = \mathcal{L} : \mathbf{A}^{(1)} + \mathbf{A}^{(1)}\mathbf{A}^{(0)}W_A^{(0)} - p^{(1)}\mathbb{1}, \tag{2.38}$$

where $p = p^{(0)} + \epsilon p^{(1)}$ and $\mathcal{L}$ is the fourth-order tensor given by

$$\mathcal{L} : \mathbf{A}^{(1)} = \mathbf{A}^{(0)}\left(W_{AA}^{(0)} : \mathbf{A}^{(1)}\right)\mathbf{A}^{(0)}. \tag{2.39}$$

Here, $W_A^{(0)}$ and $W_{AA}^{(0)}$ are the first and second derivatives of W with respect to $\mathbf{A}$ evaluated at $\mathbf{A}^{(0)}$. Explicitly, the non-zero components of $\mathcal{L}$ are given by [73]:

$$\left.\begin{aligned}
\mathcal{L}_{iijj} &= \mathcal{L}_{jjii} = \alpha_i\alpha_j\frac{\partial^2 W}{\partial\alpha_i\partial\alpha_j}, & \\
\mathcal{L}_{ijij} &= \alpha_i^2\frac{\alpha_i\frac{\partial W}{\partial\alpha_i} - \alpha_j\frac{\partial W}{\partial\alpha_j}}{\alpha_i^2 - \alpha_j^2}, & i\neq j, \alpha_i\neq\alpha_j,\\
\mathcal{L}_{ijij} &= \tfrac{1}{2}\left(\mathcal{L}_{iiii} - \mathcal{L}_{iijj} + \alpha_i\frac{\partial W}{\partial\alpha_i}\right), & i\neq j, \alpha_i = \alpha_j,\\
\mathcal{L}_{ijij} - \mathcal{L}_{ijji} &= \mathcal{L}_{ijij} - \mathcal{L}_{jiij} = \alpha_i\frac{\partial W}{\partial\alpha_i}, & i\neq j,
\end{aligned}\right\} \tag{2.40}$$

where α_i are the principal stretches of $\mathbf{A}^{(0)}$. The incremental equilibrium equations are then given by

$$\rho\ddot{\mathbf{x}}^{(1)} = \rho\mathbf{b}^{(1)} + \mathrm{div}(\mathbf{T}^{(1)}), \tag{2.41}$$

where $\mathbf{x}^{(1)}$ and $\mathbf{b}^{(1)}$ are the incremental material coordinate and body force per unit mass respectively. The boundary conditions are given by fixing $\boldsymbol{\chi}^{(1)}$ on some part of the boundary and on the remainder, we prescribe zero incremental stress, so that

$$\mathbf{T}^{(1)}.\hat{\mathbf{n}} = \mathbf{0}. \tag{2.42}$$

Should there exist of a solution of (2.41) and its associated boundary conditions, we will assume that the finite solution cedes stability to another state. In general this is not necessarily true. In order to examine the stability of each solution, we could investigate whether each solution corresponds to a local minimum of the strain energy or not. Haughton and Chen [17] derived a stability criterion for inhomogeneous deformations of incompressible hyperelastic materials and applied it to inflation problems involving thick-walled cylinders. In all cases tested, they found that the bifurcation point corresponded to a change in stability of the finite solution, and we expect the same to be true in all cases we investigate.

2.3 Elastic Rod Theory

In certain scenarios a reduced theory can be used to model an elastic body. One example, which is of particular interest in our work, is the theory of elastic rods. This can be applied to the case of slender structures, where the length of the body is of a greater order of magnitude than its other two spatial dimensions. In such cases, most of the information regarding the geometry of the structure is encoded in a 1-D curve running through its cross-section. In 3-D Cartesian co-ordinates, we define this curve, in the current configuration, to be

$$\mathbf{r} = (x_1(s;t), x_2(s;t), x_3(s;t)), \tag{2.43}$$

where s is the arc length in the current configuration. It follows that at any fixed time, t, the vector $\boldsymbol{\tau} = \dfrac{\partial \mathbf{r}}{\partial s}$ is a unit tangent to to the curve at any point, P on the centreline. We then define $\kappa\boldsymbol{\nu} = \dfrac{\partial \boldsymbol{\tau}}{\partial s}$ to be a normal to the centreline at P, where $\kappa = \left|\dfrac{\partial \boldsymbol{\tau}}{\partial s}\right|$ is the curvature of the centreline. Finally a third unit vector, $\boldsymbol{\beta}$, known as the binormal, is given by $\boldsymbol{\beta} = \boldsymbol{\tau} \wedge \boldsymbol{\nu}$. At each point on the centreline, we now have a local orthonormal basis, $\mathcal{B}_1 = \{\boldsymbol{\nu}, \boldsymbol{\beta}, \boldsymbol{\tau}\}$, known as the Frenet frame (or Frenet-

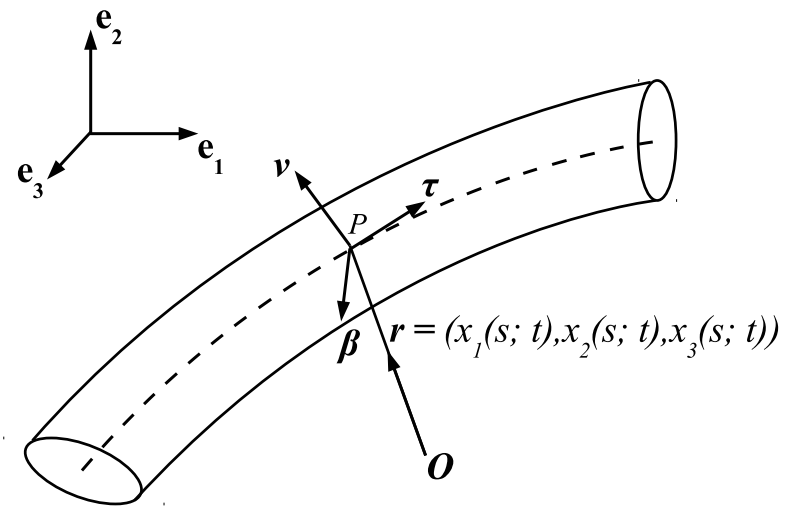

Figure 2.3: The Frenet frame of an elastic rod is shown for an arbitrary point, P on its centreline. Equations (2.44)-(2.46) govern the variation of the Frenet frame with respect to the arc length parameter, s.

Serret frame), which varies along the centreline as a function of s according to the Frenet-Serret equations:

$$\frac{\partial \boldsymbol{\tau}}{\partial s} = \kappa \boldsymbol{\nu}, \tag{2.44}$$

$$\frac{\partial \boldsymbol{\nu}}{\partial s} = -\kappa \boldsymbol{\tau} + \tau \boldsymbol{\beta}, \tag{2.45}$$

$$\frac{\partial \boldsymbol{\beta}}{\partial s} = -\tau \boldsymbol{\nu}. \tag{2.46}$$

The scalar quantity τ is known as the torsion, and is a measure of rotation of the Frenet frame about $\boldsymbol{\tau}$. In Figure 2.3 a depiction of an elastic rod, showing its Frenet frame at a point on the centreline is shown.

The Frenet-Serret equations alone are not sufficient to study the elastic behaviour of rod-like structures, since a description of a rod's centreline does not uniquely define its geometry. As an example, consider a thin strip of paper; if the paper is held at either end and one end is subjected to a single twist, the geometry of the strip has changed, even though its centreline is unaffected. Similarly, shearing a rod in a direc-

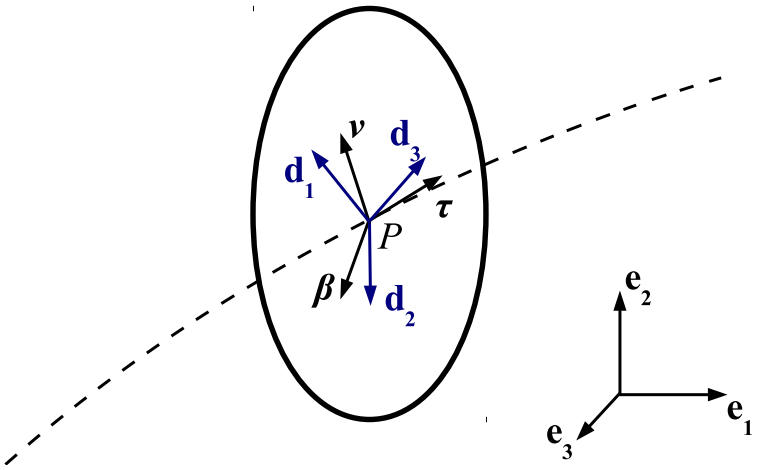

Figure 2.4: The relationship between the Frenet frame, $\mathcal{B}_1$ and the local director basis, $\mathcal{B}_2$ is illustrated. The two vectors $\mathbf{d}_1$ and $\mathbf{d}_2$ remain in the cross-section throughout. If the rod is unshearable then $\mathbf{d}_3 = \boldsymbol{\tau}$ and the bases $\mathcal{B}_1$ and $\mathcal{B}_2$ differ only by a cross-sectional twist.

tion parallel to $\boldsymbol{\tau}$ affects the geometry whilst preserving its centreline. To distinguish between such configurations, a second local basis, $\mathcal{B}_2 = \{\mathbf{d}_1(S;t), \mathbf{d}_2(S;t), \mathbf{d}_3(S;t)\}$ is required. Here, $\mathbf{d}_1$ and $\mathbf{d}_2$ are taken to be orthonormal vectors lying in the cross-sectional plane of the rod at a point P, with $\mathbf{d}_3 = \mathbf{d}_1 \wedge \mathbf{d}_2$. The relationship between this local director basis and the Frenet frame is shown in Figure 2.4. In this case the arc length, S is defined with respect to a stress-free configuration. These vectors satisfy the general system of equations

$$\frac{\partial \mathbf{r}}{\partial S} = \mathsf{v}, \tag{2.47}$$

$$\frac{\partial \mathbf{d}_i}{\partial S} = \mathsf{u} \wedge \mathbf{d}_i, \tag{2.48}$$

$$\frac{\partial \mathbf{d}_i}{\partial t} = \mathsf{w} \wedge \mathbf{d}_i, \tag{2.49}$$

where u and v are strain vectors, whilst w is known as a spin vector. We use sans-serif fonts to denote vectors written in terms of the basis $\mathcal{B}_2$, so that $\mathsf{u} = \mathsf{u}_1\mathbf{d}_1 + \mathsf{u}_2\mathbf{d}_2 + \mathsf{u}_3\mathbf{d}_3$

and similarly for v and w. Finally, we define $\alpha = \dfrac{\partial s}{\partial S}$ to be the change in arc length between the unstressed and current configurations.

We now consider the mechanics of an elastic rod. Let $\mathbf{n}$ denote contact forces and $\mathbf{f}$ denote body forces per unit unstressed arc length acting on the rod. Applying the principle of conservation of linear momentum to an arbitrary section of the rod $[S, S_1]$, we obtain the localised equation

$$\rho A \ddot{\mathbf{r}} = \frac{\partial \mathbf{n}}{\partial S} + \mathbf{f}, \tag{2.50}$$

where ρ represents mass density per unit unstressed arc length and A denotes the unstressed cross-sectional area of the rod. Furthermore, if $\mathbf{m}$ represents internal couple and $\mathbf{l}$ represents body couple per unit unstressed arc length, applying the principle of conservation of angular momentum, we obtain the following

$$\frac{\partial \mathbf{m}}{\partial S} + \frac{\partial \mathbf{r}}{\partial S} \wedge \mathbf{n} + \mathbf{l} = \dot{\mathbf{J}}, \tag{2.51}$$

where

$$\mathbf{J} = \rho \left(\mathcal{I}_2 \mathbf{d}_1 \wedge \dot{\mathbf{d}}_1 + \mathcal{I}_1 \mathbf{d}_2 \wedge \dot{\mathbf{d}}_2 \right). \tag{2.52}$$

The quantities $\mathcal{I}_1$ and $\mathcal{I}_2$ are the second moments of cross-sectional area about the axes $\mathbf{d}_1$ and $\mathbf{d}_2$.

To close the problem, constitutive relations must be prescribed. Assuming the rod is isotropic and unshearable, with quadratic strain energy, the expressions relating stresses to strains can be written as follows

$$\mathbf{m} = K_{m_1}(\mathsf{u}_1 - \hat{\mathsf{u}}_1)\mathbf{d}_1 + K_{m_2}(\mathsf{u}_2 - \hat{\mathsf{u}}_2)\mathbf{d}_2 + K_{m_3}(\mathsf{u}_3 - \hat{\mathsf{u}}_3)\mathbf{d}_3, \tag{2.53}$$

$$\mathbf{n} = K_{n_1}(\mathsf{v}_1 - \hat{\mathsf{v}}_1)\mathbf{d}_1 + K_{n_2}(\mathsf{v}_2 - \hat{\mathsf{v}}_2)\mathbf{d}_2 + K_{n_3}(\mathsf{v}_3 - \hat{\mathsf{v}}_3)\mathbf{d}_3. \tag{2.54}$$

The parameters K_{m_i} and K_{n_i}, $\quad i = 1, 2, 3$, depend upon the material and geometric properties of the rod. We refer to K_{m_1} and K_{m_2} as the principal bending stiffnesses of the rod, whilst K_{m_3} is known as the torsional stiffness. For an unstressed body, these can be written explicitly as follows

$$K_{m_1} = E\mathcal{I}_1, \quad K_{m_2} = E\mathcal{I}_2, \quad K_{m_3} = \mu\mathcal{J}, \tag{2.55}$$

where E is the Young's modulus of the constituent material, μ is the shear modulus and $\mathcal{J}$ is a parameter that depends upon the shape of the cross-section. In Chapter 3, we will investigate how these constitutive laws are modified when a stress-free rod is subjected to a non-uniform growth field.

We have now derived the equations of equilibrium and proposed various constitutive laws, which can be used to model both 3-D and (essentially) 1-D structures subject to large deformations. In Chapters 3 and 4 we will use both modelling approaches to investigate differential growth in the context of filamentary structures. In both cases, our focus will be to use the full 3-D elasticity framework to inform various choices of parameter values, which can be used in the rod theory framework. In Chapter 5, we restrict our attention to 3-D elasticity only, and investigate the role of anisotropy, muscle fibre contraction and residual stress in enabling the chameleon's tongue to undergo high-power projection and catch prey before they are able to react.

Chapter 3

Differential Growth of a One-Layer Cylinder

In Chapter 1, we described briefly some of the characteristic features of biological tissue: growth, anisotropy, incompressibility and the existence of multiple layers of tissue. Of these features, only growth is found in all living tissue, and we shall focus on this aspect in this chapter.

3.1 Introduction

Growth is a fundamental process in nature. All living organisms grow not only to increase their size, but also to develop complex morphologies, ranging from the delicate folding patterns of the brain to the spiraled horns of the ram. At the tissue level, such complexity is achieved via differential growth: a phenomenon in which different regions of the same body grow at different rates. We have previously discussed several examples of systems exhibiting differential growth: the looping of the intestinal system, which is driven by a mismatch in the growth of the gut wall and mesentery lining, many types of plant stalk, the arterial walls and the lining of the airway walls.

However, growth does not only affect the geometry (*i.e.* the shape and size) of a

body. It is also intrinsically linked to the body's mechanical behaviour. In particular, differential growth generates residual stresses, which exist even in the absence of applied loads. Residual stress is caused by incompatibilities, which arise due to the non-uniform nature of differential growth. The mechanical changes caused by residual stress can often be advantageous to a structure. For instance, it may increase the structure's stability or alter its mechanical properties. In Chapter 1 we presented the example of the rhubarb stalk to demonstrate the geometric changes induced by the relieving of residual stress when peeled. There is also a mechanical difference between the peeled and intact stalks. If two sections of identical length are subject to an applied moment, it is observed that the peeled stalk is much easier to bend than the residually-stressed stalk [99]. Alternatively it may allow a structure to maintain a particular form under loading, as is the case with arteries remaining the same length at all times under the pulsatile flow of blood within.

A useful tool for modelling the mechanics of biological tissues is the theory of finite elasticity, introduced in Chapter 2. This theory is a well-developed framework, which allows for the study of arbitrarily large deformations. It can easily be adapted to study differential growth, thanks to the work of Rodriguez *et al.* in 1994 [81]. Their idea that a deformation gradient tensor can be decomposed into stress-free local growth and an elastic response is a fundamental principle in the theory of morphoelasticity. The main drawback of finite elasticity is that the resulting governing equations are, in general, difficult to solve. Only in a small number of cases, in which the geometry is simple, are the equations tractable. These were first summarised by Truesdell in 1952, building upon earlier results of Rivlin [80, 95]. In each case a 'semi-inverse' approach is used, whereby the form of the deformation is specified up to one or more unknowns and these are determined using the loading conditions on the boundary of the object. One such example where a semi-inverse approach can be used is the mapping of a cylinder to another cylinder. This approach is particularly applicable

in many biological scenarios due to the abundance of cylindrical structures found throughout nature. Hence, the theory of finite elasticity is a useful tool for modelling differential growth of many, biological structures, but only in those cases where an idealised cylindrical geometry is applicable.

In the case of slender structures, the theory of elastic rods provides an attractive alternative to finite elasticity for studying more geometrically complex morphologies. Here, the geometry of a 3-D structure is reduced to a 1-D curve describing its centre-line and an associated director basis describing the orientation of the cross-section. Such models have been used successfully to model many biological problems, including vines twining around trees, molecular polymers and microtubules. However, by reducing the structure to a 1-D object, the cross-sectional stresses and moments are also reduced to averaged quantities. In the process of averaging, the notion of residual stress is naturally lost, and only the geometric effects of growth are accounted for.

In short, if one wishes to account for complexity in the mechanical response of an elastic body, a natural choice of framework to use is finite elasticity, whilst if one wishes to account for complexity in the geometry, then rod theory is the natural choice. However, when considering the differential growth of biological structures, it is likely that complexity will arise in both the mechanical behaviour and the geometry of the system. In such circumstances, how should one proceed? One possibility is to utilise numerical techniques. In particular, finite element methods are powerful tools, which can yield approximations to the finite elasticity equations of equilibrium, even in the case of complex geometries. However, it is difficult to gain insight into the underlying physical features that govern the behaviour of a system using numerical techniques. An alternative strategy, in the case of slender structures, is to somehow combine both theories described above: with finite elasticity, the mechanical properties of a body can be captured within a 3-D setting. If these properties could be mapped into the 1-D framework of elastic rods then it may be possible to explore a

wide variety of deformations. In short, the idea is to seek an effective rod to describe the body, whose mechanical properties incorporate the effects of residual stresses arising from differential growth of the full 3-D body.

The objective of this chapter is to take a first step in defining such a map between these two theories. We consider several simple, but natural forms of growth that a cylinder may undergo, including anisotropic and inhomogeneous cases. In each case, the growth affects the cylinder by altering its geometry and generating residual stress. We use three simple mechanical tests to determine three different mechanical properties. These 'effective stiffnesses' combine the effects of the change in geometry and residual stress. Thus, if they are used as parameters in the rod's constitutive law, then we have a means of studying geometrically-complex deformations of a slender structure, without losing all effects of residual stress. In the absence of residual stress, the correspondence between non-linear elasticity and rod theory is well-understood; there exist various methods of deriving rod theories from the full 3-D approach. For example, Parker [75] and Green *et al.* [39] used a direct approach to obtain the equations of equilbrium for an elastic rod, with [39] including a derivation of the constitutive parameters. Mora and Müller [65] used a variational approach to derive a theory of inextensible rods from 3-D, non-linear elasticity. However, we are not aware of an existing rigorous derivation of a rod theory from a residually-stressed body.

We begin by briefly summarising the framework of morphoelasticity and stating the equations of equilibrium and relevant boundary conditions for an incompressible, isotropic cylinder subject to differential growth. An analogous rod theory approach is derived for the same problem and we give details of the key parameters used in its constitutive laws. Given an initial stress-free cylinder and prescribed growth law, the goal is to use the morphoelastic formulation to derive an 'effective' rod, whose material properties are similar to those of the grown, residually-stressed cylinder. We consider

six types of growth law that are simple, but cover a range of scenarios, including non-uniform growth in all directions, as well as anisotropic growth. We assess the reliability of the estimated stiffnesses by comparing them with the corresponding values obtained using a numerical scheme. This method gives insight into the role of effective material properties and geometry in determining mechanical properties of a growing filament. Furthermore, we investigate the inverse problem of whether a desired set of mechanical properties can be prescribed and a suitable growth law can be found that will yield such properties.

3.2 Non-Linear Framework

We consider a continuous, hyperelastic cylinder, whose reference configuration is $\mathcal{B}_0$. A material point in this stress-free configuration is denoted by

$$\mathbf{X} = (R, \Theta, Z) = R\mathbf{E}_R + Z\mathbf{E}_Z, \tag{3.1}$$

where $A \leq R \leq B$ and $0 \leq Z \leq L$. We assume all deformations $\boldsymbol{\chi}$ maintain the cylindrical form of the body and the axial stretch is constant. Then the image of $\mathbf{X}$ in the deformed configuration, $\mathcal{B}_f$, can be written as

$$\mathbf{x} = (r(R), \Theta + \tau Z, \lambda Z) = r(R)\mathbf{e}_r + \lambda Z\mathbf{e}_z, \tag{3.2}$$

where $a \leq r \leq b$ and $\lambda > 0$ is constant. The deformation gradient has the form

$$\mathbf{F} = \text{Grad } \mathbf{x} = \begin{pmatrix} r' & 0 & 0 \\ 0 & \frac{r}{R} & \tau r \\ 0 & 0 & \lambda \end{pmatrix}. \tag{3.3}$$

Appealing to the fundamental assumption of morphoelasticity, the deformation gradient can be decomposed into stress-free growth and an elastic response, according to (2.4), where the stress-free growth tensor, $\mathbf{G}$ is assumed to be of the form

$$\mathbf{G} = \text{diag } (\gamma_1(R), \gamma_2(R), \gamma_3(R)), \tag{3.4}$$

and the elastic tensor, $\mathbf{A}$ is given by

$$\mathbf{A} = \mathbf{F}\mathbf{G}^{-1} = \begin{pmatrix} \frac{r'}{\gamma_1} & 0 & 0 \\ 0 & \frac{r}{R\gamma_2} & \frac{\tau r}{\gamma_3} \\ 0 & 0 & \frac{\lambda}{\gamma_3} \end{pmatrix}. \tag{3.5}$$

We assume that the cylinder is made of incompressible material. This assumption often used to model soft, biological tissue [51] and implies $\det(\mathbf{A}) = 1$, from which we obtain the following expression for $r(R)$:

$$r = \sqrt{a^2 + 2\int_A^R \frac{\gamma_1\gamma_2\gamma_3\tilde{R}}{\lambda}\, \mathrm{d}\tilde{R}}, \tag{3.6}$$

where $a = r(A)$. We define $\mathbf{B} = \mathbf{A}\mathbf{A}^T$ to be the left Cauchy-Green stretch tensor, whose eigenvalues are given by

$$\alpha_1 = \frac{r'}{\gamma_1}, \tag{3.7}$$

$$\alpha_2 = \left(\frac{\gamma_3^2 r^2 + \gamma_2^2 R^2 (r^2\tau^2 + \lambda^2) + \sqrt{\gamma_3^4 r^4 + 2\gamma_2^2\gamma_3^2 r^2 R^2 (r^2\tau^2 - \lambda^2) + \gamma_2^4 R^4 (r^2\tau^2 + \lambda^2)^2}}{2\gamma_2^2\gamma_3^2 R^2} \right)^{\frac{1}{2}}, \tag{3.8}$$

$$\alpha_3 = \left(\frac{\gamma_3^2 r^2 + \gamma_2^2 R^2 (r^2\tau^2 + \lambda^2) - \sqrt{\gamma_3^4 r^4 + 2\gamma_2^2\gamma_3^2 r^2 R^2 (r^2\tau^2 - \lambda^2) + \gamma_2^4 R^4 (r^2\tau^2 + \lambda^2)^2}}{2\gamma_2^2\gamma_3^2 R^2} \right)^{\frac{1}{2}}. \tag{3.9}$$

These eigenvalues are referred to as the principal stretches. Note that in the absence of twist, $\tau = 0$ and the principal stretches are precisely the diagonal components of $\mathbf{A}$.

Incompressibility implies $I_3 \equiv 1$, therefore we can use a modified form of (2.25) to describe the material response:

$$W = \bar{W}(I_1, I_2), \tag{3.10}$$

In this case, the constitutive equation for the Cauchy stress tensor is given by a modified form of (2.29):

$$\mathbf{T} = -p\mathbf{I} + 2((\bar{W}_1 + I_1\bar{W}_2)\mathbf{B} - \bar{W}_2\mathbf{B}^2), \tag{3.11}$$

where the notation $\bar{W}_i$ denotes differentiation of $\bar{W}$ with respect to the i^{th} strain invariant, I_i. Explicitly, the non-zero components of $\mathbf{T}$ are given by

$$T_{rr} = -p + 2((\bar{W}_1 + I_1\bar{W}_2)B_{rr} - \bar{W}_2 B_{rr}), \tag{3.12}$$

$$T_{\theta\theta} = -p + 2((\bar{W}_1 + I_1\bar{W}_2)B_{\theta\theta} - \bar{W}_2(B_{\theta\theta}^2 + B_{zz}^2)), \tag{3.13}$$

$$T_{zz} = -p + 2((\bar{W}_1 + I_1\bar{W}_2)B_{zz} - \bar{W}_2(B_{\theta z}^2 + B_{\theta z}^2)), \tag{3.14}$$

$$T_{\theta z} = T_{z\theta} = 2((\bar{W}_1 + I_1\bar{W}_2)B_{\theta z} - \bar{W}_2 B_{\theta z}(B_{\theta\theta} + B_{zz})). \tag{3.15}$$

The off-diagonal stresses are known explicitly, but the diagonal stresses depend upon the unknown variable, p. However, we are able to proceed by solving the equilibrium equations. An important assumption we shall make use of throughout this study is that the growth is slow. That is, the elastic dynamics of the body operate on a faster timescale than the growth, so that the body can be taken to be in static equilibrium

throughout. In the absence of body forces, the resulting form of (2.8) is

$$\text{div } \mathbf{T} = \mathbf{0}. \tag{3.16}$$

Due to the imposed symmetry and constant axial stretch, the problem is independent of θ and z. Hence, the only non-trivial equation arising from (3.16) is

$$\frac{dT_{rr}}{dr} = \frac{T_{\theta\theta} - T_{rr}}{r}, \tag{3.17}$$

which is independent of p. Integrating (3.17), we obtain the following expression for the radial stress:

$$T_{rr} = T_{rr}(a) + \int_a^r \frac{T_{\theta\theta} - T_{rr}}{r}\, \mathrm{d}r = T_{rr}(a) + \int_A^R \frac{\gamma_1\gamma_2\gamma_3\tilde{R}\lambda\,(T_{\theta\theta} - T_{rr})}{r^2}\, \mathrm{d}\tilde{R}. \tag{3.18}$$

Substitution of (3.18) into (3.12) yields an expression for p, which can be used in (3.13)-(3.15) to determine the remaining stress components, $T_{\theta\theta}, T_{zz}$ and $T_{\theta z}$, in terms of the unknown geometric quantities, a, τ and λ. These are determined using the boundary conditions.

3.2.1 Boundary Conditions

We first consider the curved outer and inner boundaries of the cylinder, denoted $\partial\mathcal{B}_1$ and $\partial\mathcal{B}_2$ respectively. On the exterior surface, $r = b$, we impose zero traction, so that

$$T_{rr}(b) = 0. \tag{3.19}$$

If the deformed cylinder is hollow, then we impose a similar stress-free condition at the inner curved boundary:

$$T_{rr}(a) = 0. \tag{3.20}$$

If the initial configuration is a solid cylinder, *i.e.* $A = 0$, we will impose the condition that the deformed body must also be solid[1], so that

$$r(0) = 0. \tag{3.21}$$

On the flat ends of the cylinder, $\partial\mathcal{B}_3$, the boundary conditions are formulated in terms of the applied loads and applied moments. The axial load, denoted by N is given by

$$N = 2\pi \int_a^b r T_{zz} \mathrm{d}r = 2\pi \int_A^B \frac{\gamma_1\gamma_2\gamma_3}{\lambda} R T_{zz} \, \mathrm{d}R. \tag{3.22}$$

The bending moment about the x-axis (which is defined such that the positive x-axis coincides with the half-line $\Theta = 0$) is defined by

$$M_x = \int_{\partial\mathcal{B}_3} (y\mathbf{e}_y \wedge \mathbf{T}\mathbf{e}_z).\mathbf{e}_x \, \mathrm{d}\mathcal{A} = \int_{\partial\mathcal{B}_3} y T_{zz} \, \mathrm{d}\mathcal{A}, \tag{3.23}$$

whilst the applied twisting moment about the z-axis is denoted by $\mathbf{M}_z$ and is given by

$$M_z = \int_{\partial\mathcal{B}_3} (r\mathbf{e}_r \wedge \mathbf{T}\mathbf{e}_z).\mathbf{e}_z \, \mathrm{d}\mathcal{A} = \int_{\partial\mathcal{B}_3} r T_{\theta z} \, \mathrm{d}\mathcal{A}. \tag{3.24}$$

For convenience, we shall use M_x and M_z to denote the $\mathbf{e}_x$ and $\mathbf{e}_z$ components of $\mathbf{M}_x$ and $\mathbf{M}_z$ respectively. Additionally, we assume all other components of applied moments and tractions are zero throughout.

To determine the effective stiffnesses under a particular growth profile, we first need to find the geometry of the grown, unloaded configuration. We use the notation a^*, λ^* and τ^* to denote the values of a, λ and τ in this configuration. This state

[1]Depending on the form of the strain-energy density, there may exist solutions to both the cavitated and uncavitated boundary value problems. See [34] for more details. We shall assume throughout this work that the cylinder always remains solid.

satisfies the boundary conditions

$$M_x = 0, \quad M_z = 0, \quad N = 0. \tag{3.25}$$

Once the unloaded configuration is known, the idea is to subject the cylinder to three different types of load and measure the geometric change, as represented in Figure 3.1. The first mechanical test represents uniaxial tension:

$$M_x = 0, \quad M_z = 0, \quad N = \delta N_1. \tag{3.26}$$

Here, $\delta \ll 1$ is used to characterise the size of the applied load (or, as may the case, applied moment). The second represents a twist about the centreline of the cylinder and is given by

$$M_x = 0, \quad M_z = \delta M_{z_1}, \quad N = 0. \tag{3.27}$$

The final set of boundary conditions represents bending about the x-axis and is given by

$$M_x = \delta M_{x_1}, \quad M_z = 0, \quad N = 0. \tag{3.28}$$

Each mechanical test yields a different parameter, representing the response of the cylinder to each type of load. It is these three parameters that are mapped into the effective rod formulation in order to capture the effect of residual stress. In the following section, we turn to the rod formulation and give details of the mapping between the two frameworks.

3.3 Rod Theory Framework

Our objective is to construct a map between the residually-stressed grown cylinder and an elastic rod whose initial configuration is geometrically identical to the unloaded

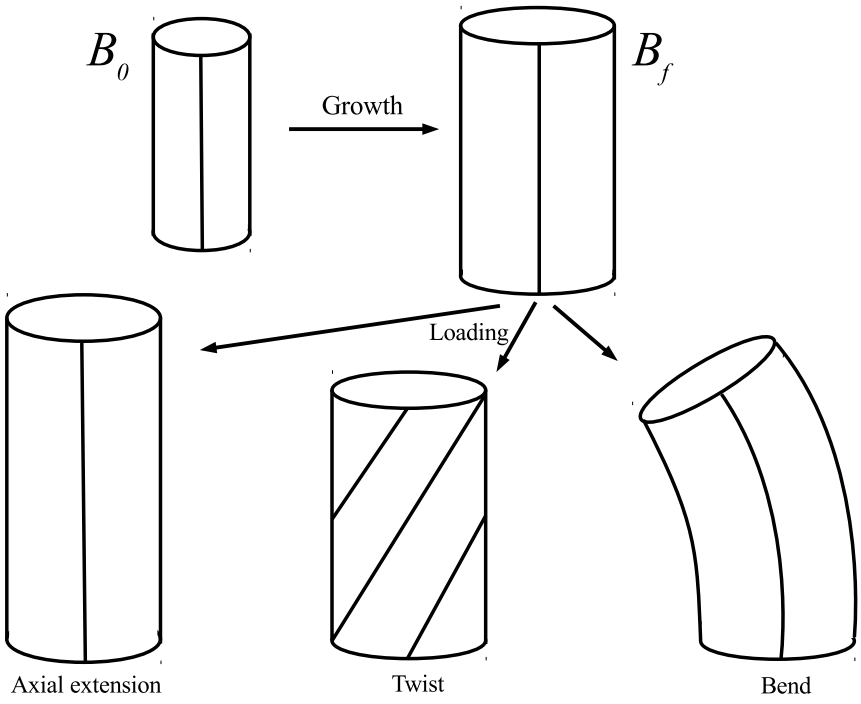

Figure 3.1: Illustration of the non-linear problem, in which an initially stress-free cylinder is subject to a prescribed growth profile. The grown cylinder is then subject to three different mechanical tests to determine its effective mechanical properties. Extension corresponds to the boundary conditions (3.26), twisting to (3.27) and bending to (3.28).

configuration. As before, we assume the rod is in static equilibrium, so that in the absence of applied forces and couples, we have, from (2.50) and (2.51)

$$\frac{\partial \mathbf{n}}{\partial S} = \mathbf{0}, \tag{3.29}$$

$$\frac{\partial \mathbf{m}}{\partial S} + \frac{\partial \mathbf{r}}{\partial S} \wedge \mathbf{n} = \mathbf{0}. \tag{3.30}$$

In addition, for an extensible, unshearable rod that is initially straight, untwisted and unstretched, the constitutive laws, (2.53) and (2.54), can be written as

$$\mathbf{m} = K_{m_1} \mathsf{u}_1 \mathbf{d}_1 + K_{m_2} \mathsf{u}_2 \mathbf{d}_2 + K_{m_3} \mathsf{u}_3 \mathbf{d}_3, \tag{3.31}$$

$$\mathsf{n}_3 = K_{n_3}(\alpha - 1). \tag{3.32}$$

Together with the kinematic relations (2.47)-(2.48), the equations (3.29)-(3.30) constitute a system of 18 first-order ordinary differential equations, which can be solved subject to suitable boundary conditions.

The quantities $K_{m_1} = K_{m_2}$ are referred to as the principal bending stiffnesses, whilst K_{m_3} is the torsional stiffness and K_{n_3} is the axial stiffness. Once prescribed, we have a complete mechanical description of the rod. It is these three parameters that are to be obtained from full 3-D elasticity framework and the simulated mechanical tests described in the previous section and illustrated in Figure 3.1. Differential growth affects these stiffnesses by changing the geometry of the cylinder and generating residual stress, thus, by estimating these quantities using 3-D elasticity we have a means of capturing residual stress in the rod theory framework.

We first consider axial extension. The effective axial stiffness is obtained by taking the limit of the ratio of the applied axial load to resulting strain as the strain tends

to zero. In other words, it is the infinitesimal load-to-strain ratio:

$$K_{n_3} = \lim_{\delta\to 0} \frac{N(\hat{\lambda}) - N(\lambda^*)}{\frac{\hat{\lambda}-\lambda^*}{\lambda^*}} = \lim_{\delta\to 0} \lambda^* \frac{N(\hat{\lambda}) - N(\lambda^*)}{\delta\lambda} = \lambda^* \left.\frac{\partial N}{\partial \lambda}\right|_{\lambda=\lambda^*}. \tag{3.33}$$

Here, we use $\hat{\lambda}$ (and subsequently $\hat{\tau}$ and $\hat{\kappa}$) to denote the axial stretch (and twist and curvature respectively) in the loaded configuration. Note that our definition of strain is the extension per unit unloaded length, rather than per unit reference length. We use this definition because the undeformed, effective rod is assumed to have the same length as the unloaded configuration, so we require the change in length between the loaded and unloaded configurations. Next we consider torsion of the cylinder. We measure the moment about the rod's centreline required to twist the rod such that the cross-section of one end of the rod is rotated by an angle of τL with respect to the other end. Note that the angle is defined in terms of the initial arc length, S, for consistency with (3.2). The effective torsional stiffness is then given by the limit of the ratio of applied moment to resulting twist per unit current length as the twist tends to zero. That is:

$$K_{m_3} = \lim_{\delta\to 0} \frac{M_z(\hat{\tau}) - M_z(\tau^*)}{\frac{L\hat{\tau}-L\tau^*}{L\lambda^*}} = \lim_{\delta\to 0} \lambda^* \frac{M_z(\hat{\tau}) - M_z(\tau^*)}{\delta\tau} = \lambda^* \left.\frac{\partial M_z}{\partial \tau}\right|_{\tau=\tau^*}. \tag{3.34}$$

Finally, we consider the effective bending stiffness. We measure the moment about the x-axis required to bend the rod such that its centreline lies on the arc of a circle of radius ρ and the angle between the two ends of the rod measured at the centre of this circle is κL, where κ is the curvature of the rod. As with the torsional stiffness, the curvature is measured with respect to the initial configuration. The effective bending stiffness is then given by the limit of the ratio of applied moment to resulting angle of deflection as the curvature tends to zero. That is:

$$K_{m_1} = \lim_{\delta\to 0} \frac{M_x(\hat{\kappa}) - M_x(\kappa^*)}{\frac{L\hat{\kappa}-L\kappa^*}{L\lambda^*}} = \lim_{\delta\to 0} \lambda^* \frac{M_x(\hat{\kappa}) - M_x(\kappa^*)}{\delta\kappa} = \lambda^* \left.\frac{\partial M_z}{\partial \kappa}\right|_{\kappa=\kappa^*}. \tag{3.35}$$

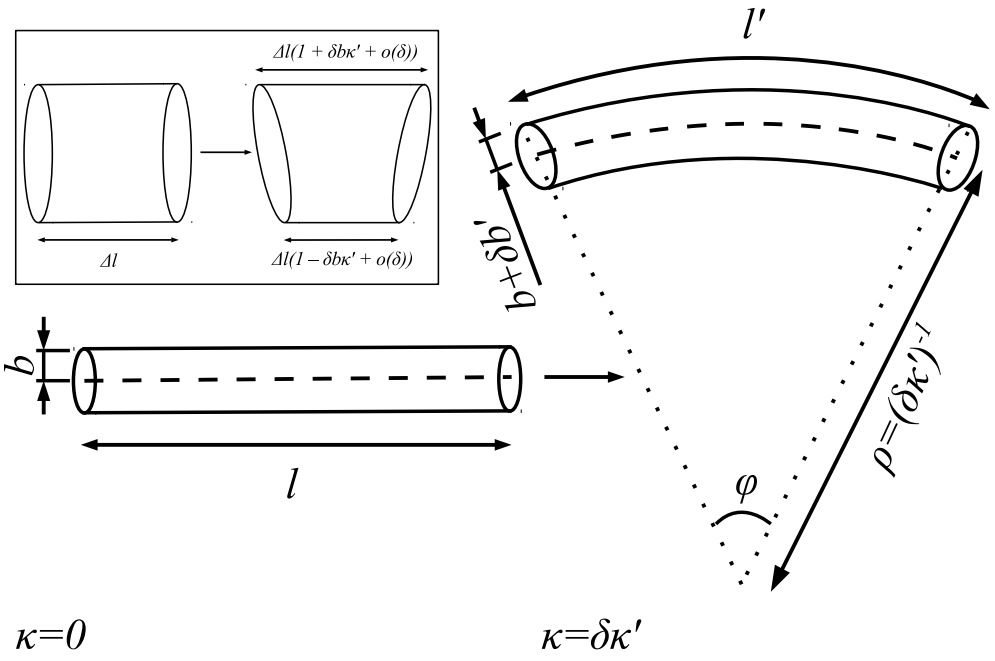

Figure 3.2: Applying a bending moment induces a non-zero curvature. Inset: on a local level, this deformation can be approximated by an axial stretch that varies as a linear function of the y-coordinate.

Finding the principal bending stiffnesses is trickier, since bending breaks the symmetry of the problem. To overcome this difficulty, we consider the rod illustrated in Figure 3.2. We approximate the bending as a mapping from the straight configuration to one in which the length of the centreline is preserved and image of every line initially parallel to the z-axis is the arc of a circle with centre Q. We refer to the angle formed by the ends of the rod at Q as $\delta\varphi$, and the distance from Q to any point on the deformed centreline as ρ, so that

$$\rho\delta\varphi = \lambda^* L. \tag{3.36}$$

Then, any line that lies a distance y^* in the $\mathbf{e}_2$ direction from the centreline will lie a distance $\rho + y^* + \delta y'$ from Q following bending (*i.e.* the distance between two lines may change during bending, but only by an amount that is the same order of

magnitude as the bending moment). Thus, the deformed length of a line parallel to the centreline is given by

$$l(y) = \delta\varphi\,(\rho + y^* + \delta y') = \lambda^* L + \delta\varphi y^* + \mathcal{O}(\delta^2). \tag{3.37}$$

The corresponding axial stretch at each point in the body can then easily be obtained:

$$\lambda = \lambda^* + \delta y^* \kappa' + \mathcal{O}(\delta^2), \tag{3.38}$$

where $\kappa' = \frac{\varphi}{L}$. Expanding (3.23) about the unloaded state gives the following

$$M_x = \int_{\mathcal{A}} y \left(T_{zz}(\alpha_3^*) + (\alpha_3 - \alpha_3^*) \left.\frac{\partial T_{zz}}{\partial \alpha_3}\right|_{\alpha_3=\alpha_3^*} \right) \mathrm{d}\mathcal{A} \tag{3.39}$$

$$= \int_A^B \int_0^{2\pi} y \left(T_{zz}^* + (\lambda - \lambda^*) \left.\frac{\partial T_{zz}}{\partial \lambda}\right|_{\lambda=\lambda^*} \right) r \mathrm{d}\theta \mathrm{d}r \tag{3.40}$$

Then, from (3.38) and making use of the relationship $y = r\sin\theta$, we have, in terms of the reference configuration variables

$$M_x = \int_A^B \int_0^{2\pi} y \left(T_{zz}^* + (\lambda - \lambda^*) \left.\frac{\partial T_{zz}}{\partial \lambda}\right|_{\lambda=\lambda^*} \right) r \frac{dr}{dR} \mathrm{d}\Theta \mathrm{d}R \tag{3.41}$$

$$= \int_A^B \int_0^{2\pi} r\sin\Theta \left(T_{zz}^* + \delta r \kappa' \sin\Theta \left.\frac{\partial T_{zz}}{\partial \lambda}\right|_{\lambda=\lambda^*} \right) \frac{Rr\gamma_1\gamma_2\gamma_3}{r\lambda} \mathrm{d}\Theta \mathrm{d}R \tag{3.42}$$

$$= \int_A^B \int_0^{2\pi} \frac{Rr\gamma_1\gamma_2\gamma_3}{\lambda} \sin\Theta \left(T_{zz}^* + \delta r \kappa' \sin\Theta \left.\frac{\partial T_{zz}}{\partial \lambda}\right|_{\lambda=\lambda^*} \right) \mathrm{d}\Theta \mathrm{d}R. \tag{3.43}$$

Substitution of (3.43) into (3.35) then yields an estimate of K_{m_1}.

An alternative method for computing the effective bending stiffness of a slender filament is to examine its resistance to buckling under the action of a compressive force applied to its ends. In general, computing the critical buckling force, N_{crit}, analytically is difficult, but it is possible to obtain easily a numerical value. From this estimate we can derive an estimate of the bending stiffness, which provides a

useful means of assessing the reliability of the approximation to bending described above.

To find N_{crit} we consider a small perturbation to the axisymmetric state. The perturbation belongs to a wider class of deformation with no prescribed symmetry and has the general form $\boldsymbol{\chi}^{(1)} = (u(r,\theta,z), v(r,\theta,z), w(r,\theta,z))^T$. Under this assumption, we obtain the following expression for $\mathbf{A}^{(1)}$:

$$\mathbf{A}^{(1)} = \text{grad}\boldsymbol{\chi}^{(1)} = \begin{pmatrix} u_r & \dfrac{u_\theta - v}{r} & u_z \\ \\ v_r & \dfrac{u + v_\theta}{r} & v_z \\ \\ w_r & \dfrac{w_\theta}{r} & w_z \end{pmatrix}, \tag{3.44}$$

where subscripts denote differentiation with respect to the relevant variable. The incompressibility condition leads to the relation

$$\text{tr } \mathbf{A}^{(1)} = u_r + \frac{u + v_\theta}{r} + w_z = 0. \tag{3.45}$$

We seek displacements that correspond to Euler buckling, so that u, v and w are of the form

$$u = f(r)\cos\theta \ \cos\frac{\pi z}{\lambda L}, \tag{3.46}$$

$$v = g(r)\sin\theta \ \cos\frac{\pi z}{\lambda L}, \tag{3.47}$$

$$w = h(r)\cos\theta \ \sin\frac{\pi z}{\lambda L}, \tag{3.48}$$

$$p_1 = k(r)\cos\theta \ \cos\frac{\pi z}{\lambda L}, \tag{3.49}$$

In the case of constant growth, it is easy to invert the deformation mapping to find R in terms of r. However, it is not always so simple to solve for R. Therefore, it will

be convenient to work in terms of the reference variables, so that

$$f(r(R)) = F(R), \quad g(r(R)) = G(R), \quad h(r(R)) = H(R), \quad k(r(R)) = K(R). \tag{3.50}$$

Substitution into the incremental equilibrium equations then yields

$$\begin{aligned}
K'R' = {} & (rR'(\mathcal{L}'_{2211} - \mathcal{L}'_{3311}) - \mathcal{L}_{2222} + \mathcal{L}_{2233} - \mathcal{L}_{2121} + \mathcal{L}_{1331})G/r^2 \\
& + (\mathcal{L}_{2112} + \mathcal{L}_{2211} - \mathcal{L}_{1331} - \mathcal{L}_{3311})R'G'/r \\
& + (\mathcal{L}_{1111} - \mathcal{L}_{3311} - \mathcal{L}_{1331})(R'^2F'' + R''F') \\
& + (rR'(\mathcal{L}'_{1111} + p'_0 - \mathcal{L}'_{3311}) + \mathcal{L}_{1111} - 2\mathcal{L}_{3311} + \mathcal{L}_{2233} - \mathcal{L}_{1331})R'F'/r \\
& + (rR'(\mathcal{L}'_{2211} - \mathcal{L}'_{3311}) - \mathcal{L}_{2222} + \mathcal{L}_{2233} + \mathcal{L}_{1331})F/r^2 - \mathcal{L}_{2121}F/r^2 \\
& - \frac{\pi^2}{L^2}\mathcal{L}_{3131}F,
\end{aligned} \tag{3.51}$$

$$\begin{aligned}
r\mathcal{L}_{1212}(R'^2G'' + R''G') = {} & -K + (rR'\mathcal{L}'_{1212} + \mathcal{L}_{1212} + \mathcal{L}_{2222} - \mathcal{L}_{2233} - \mathcal{L}_{3223})F/r \\
& + (rR'\mathcal{L}'_{1212} + \mathcal{L}_{1212})G/r + (\mathcal{L}_{2222} - \mathcal{L}_{2233} - \mathcal{L}_{3223})G/r \\
& + r\frac{\pi^2}{L^2}\mathcal{L}_{3232}G + (\mathcal{L}_{2211} - \mathcal{L}_{2233} - \mathcal{L}_{3223} + \mathcal{L}_{1221})R'F' \\
& - (r\mathcal{L}_{1212} + \mathcal{L}_{1212})R'G',
\end{aligned} \tag{3.52}$$

$$\begin{aligned}
\mathcal{L}_{1313}(F'''R'^3 + 3F''R'R'' + F'R''') = {} & (F' + (G+F)/r)\mathcal{L}_{2323}/r^2 \\
& - (r\mathcal{L}'_{1331} + rp'_0 + \mathcal{L}_{1331} - \mathcal{L}_{2332})\frac{\pi^2}{L^2}F/r - \mathcal{L}_{1313}((F'' + G'')/r \\
& - 2(F' + G')/r^2 + 2(F+G)/r^3) + (\mathcal{L}_{3333} - \mathcal{L}_{2332} - \mathcal{L}_{2233})\frac{\pi^2}{L^2}(F+G)/r \\
& - (r\mathcal{L}'_{1313} + \mathcal{L}_{1313})(F'' + (F'+G')/r - (F+G)/r^2)/r \\
& + (\mathcal{L}_{3333} - \mathcal{L}_{3311} - \mathcal{L}_{1331})\frac{\pi^2}{L^2}F' - \frac{\pi^2}{L^2}K.
\end{aligned} \tag{3.53}$$

On the inner and outer walls, we have the three boundary conditions:

$$(\mathcal{L}_{1122} - \mathcal{L}_{1133})(F+G) + \left(\mathcal{L}_{1111} - \mathcal{L}_{1133} + \alpha_1 \frac{\partial W}{\partial \alpha_1}\right) rR'F' - rK = 0, \tag{3.54}$$

$$rR'G' - G - F = 0, \tag{3.55}$$

$$r^2(R'^2F'' + R''F') + rF' + \frac{\pi^2}{L^2}r^2F = 0. \tag{3.56}$$

Equations (3.51)-(3.53) can be simplified by eliminating K. We then obtain a six-dimensional system of equations, which can be written in the form

$$\mathbf{y}' = \mathbf{F}(\mathbf{y}; R), \quad \mathbf{y} \in \mathbb{R}^6, \tag{3.57}$$

where $\mathbf{y}= (F, F', F'', G, G', G'')$. The remaining boundary conditions comprise a set of three linear functions $c_i(\mathbf{y}(R); R), i = 1, 2, 3$, which satisfy

$$c_{1,2,3}(\mathbf{y}(B); B) = 0. \tag{3.58}$$

The determinant method can be used to find values of γ for which non-trivial solutions exist. We make three copies of the system (3.57) and select three linearly independent vectors satisfying the boundary conditions (3.54)-(3.56) at $R = A$. We integrate this system up to $R = B$ and evaluate the 3×3 determinant of boundary conditions given by

$$\Delta(N) = \begin{vmatrix} c_1(\mathbf{y}^{(1)}(B); N) & c_2(\mathbf{y}^{(1)}(B); N) & c_3(\mathbf{y}^{(1)}(B); N) \\ c_1(\mathbf{y}^{(2)}(B); N) & c_2(\mathbf{y}^{(2)}(B); N) & c_3(\mathbf{y}^{(2)}(B); N) \\ c_1(\mathbf{y}^{(3)}(B); N) & c_2(\mathbf{y}^{(3)}(B); N) & c_3(\mathbf{y}^{(3)}(B); N) \end{vmatrix}. \tag{3.59}$$

Given an initial length of the cylinder, there exists a non-trivial solution of the system (3.51)-(3.53) satisfying the prescribed boundary conditions for values of N at which the determinant of (3.59) vanishes. To find such values, we use a numerical root-finding scheme, such as the interval bisection method. For an applied axial load,

the critical force, N^{crit} is the greatest value of N in the interval $(-\infty, 0)$ for which $\Delta(N) = 0$. Once the critical load is known, we calculate the corresponding axial stiffness using a modified form of Euler's buckling criterion, which can be obtained by seeking oscillatory solutions of the system (3.29)-(3.32):

$$K_{m_1} = -\frac{\lambda^*}{\hat{\lambda}} \frac{L^2 N^{crit}}{\pi^2}. \tag{3.60}$$

Here, the factor $\frac{\hat{\lambda}}{\lambda^*}$ represents the degree of compression of the rod at the point of buckling and arises due to the fact that the rod is compressible. In Chapter 4 a derivation of (3.60) will be given, but for now it is sufficient to simply state the result.

3.4 Incremental Growth

Having defined a mapping of the effective stiffnesses of a residually-stressed 3-D cylinder to a 1-D rod theory formulation, we now aim to see how these stiffnesses are affected by differential growth. To do so, we investigate six different simple growth laws. These are given in Table 3.1. In the following section, two letter abbreviations are used as shorthand for each type of growth. Laws I and II define constant radial (CR) growth and radially-dependent radial (RR) growth, respectively, whilst III and IV denote constant circumferential (CC) growth and radially-dependent circumferential (RC) growth respectively. In the case of V, the cross-sectional growth is isotropic, but inhomogeneous (which we shall denote CS) and in the case of VI we have radially-dependent axial (RA) growth. In all cases, ϵ characterises the magnitude of the incremental growth. When $\epsilon = 0$, the growth is uniform and isotropic, therefore no residual stress is generated. In such circumstances we are able to solve the resulting equilibrium equation (3.16) and unloaded boundary conditions (3.25)

Growth Law	$\boldsymbol{\gamma}_1$	$\boldsymbol{\gamma}_2$	$\boldsymbol{\gamma}_3$
I (CR)	$1+\epsilon\gamma_{11}$	1	1
II (RR)	$1+\epsilon\gamma_{11}(R-R_0)$	1	1
III (CC)	1	$1+\epsilon\gamma_{21}$	1
IV (RC)	1	$1+\epsilon\gamma_{21}(R-R_0)$	1
V (CS)	$1+\epsilon\gamma_{21}(R-R_0)$	$1+\epsilon\gamma_{21}(R-R_0)$	1
VI (RA)	1	1	$1+\epsilon\gamma_{31}(R-R_0)$

Table 3.1: Components of the growth tensor, $\mathbf{G}$. The growth laws represent the following situations: constant radial (CR) growth; radially-dependent radial (RR) growth; constant circumferential (CC) growth; radially-dependent circumferential (RC) growth; radially-dependent cross-sectional (CS) growth; radially-dependent axial (RA) growth. At leading order, the growth is isotropic and uniform, so no residual stress is generated and the effective stiffness changes only because of the change in cross-sectional area. We assume $\gamma_{10} = \gamma_{30} = 1$ so that any changes to the cross-sectional area and/or length occur only as a result of differential growth.

exactly, to obtain the following

$$K_{m_1} = \frac{3}{2}\pi\gamma_{10}^4(B^4 - A^4)(\bar{W}_1 + \bar{W}_2), \tag{3.61}$$

$$K_{m_3} = \pi\gamma_{10}^4(B^4 - A^4)(\bar{W}_1 + \bar{W}_2), \tag{3.62}$$

$$K_{n_3} = 6\pi\gamma_{10}^2(B^2 - A^2)(\bar{W}_1 + \bar{W}_2), \tag{3.63}$$

where $\bar{W}_i = \left.\dfrac{\partial \bar{W}}{\partial I_i}\right|_{(3,3)}$

When the growth is close to uniform and isotropic (*i.e.* $\epsilon \ll 1$), we are able to proceed analytically by expanding the variables as follows

$$\hat{a} = A + \epsilon a_1 + \epsilon^2 a_2 + \delta a_3, \tag{3.64}$$

$$\hat{\lambda} = 1 + \epsilon\lambda_1 + \epsilon^2\lambda_2 + \delta\lambda_3, \tag{3.65}$$

$$\hat{\tau} = 0 + \epsilon\tau_1 + \epsilon^2\tau_2 + \delta\tau_3, \tag{3.66}$$

$$\hat{u} = 0 + \epsilon u_1 + \epsilon^2 u_2 + \delta u_3. \tag{3.67}$$

Similarly, we have

$$K_{m_1} = K_{m_1}^{(0)} + \epsilon K_{m_1}^{(1)} + \epsilon^2 K_{m_1}^{(2)}, \tag{3.68}$$

$$K_{m_3} = K_{m_3}^{(0)} + \epsilon K_{m_3}^{(1)} + \epsilon^2 K_{m_3}^{(2)}, \tag{3.69}$$

$$K_{n_3} = K_{n_3}^{(0)} + \epsilon K_{n_3}^{(1)} + \epsilon^2 K_{n_3}^{(2)}, \tag{3.70}$$

with the leading order term in each expansion given by (3.61)-(3.63). When $\delta = 0$ we have $\hat{a} = a^*, \hat{\lambda} = \lambda^*$, *etc.* We assume $\delta \ll \epsilon^2$ because we require the growth to be small and finite, whilst each mechanical test (3.33)-(3.35) requires us to take an infinitesimal limit $\delta \to 0$. The assumption of a small gradient in the growth with respect to the radius is valid for various biological scenarios. For example, the difference in axial growth rates between the inner and outer regions of certain plant stems is at most 6% [99].

To estimate the effective stiffnesses in the case of each growth law I-VI, consider the unloaded case: we set $\delta = 0$ and substitute (3.64)-(3.67) into (3.16) and solve the resulting system at $\mathcal{O}(\epsilon)$ subject to the boundary conditions given in (3.25). This process yields a_i, λ_i, τ_i and $u_i,\ i = 1, 2$. We then solve the same system subject to each set of boundary conditions (3.26)-(3.28) in turn to obtain a relationship between the relevant applied load or torque and the remaining undetermined variables. These can be substituted into (3.33)-(3.35) to yield the desired rod theory effective stiffness parameters.

3.5 Results

We first seek the asymptotic solution of the unloaded boundary value problem. For each growth law, we obtain expressions for the unloaded axial stretch λ^* and unloaded inner radius a^*, which allows us to determine the area of the cross-section (and relevant

moments of inertia). We then consider the cases of axial tension, twisting and bending in turn.

3.5.1 Unloaded Configuration

The $\mathcal{O}(\epsilon)$ terms in the asymptotic expansions of a^* and $\mathcal{A}^*$ are given in Table 3.2. We note firstly that at $\mathcal{O}(\epsilon)$ the geometric change is independent of the choice of strain-energy density, W. This finding is to be expected if we are to ensure consistency with the theory of linear elasticity when strains are small. Secondly we note that in cases I and III, if $\gamma_{i1} > 0$ then the $\mathcal{O}(\epsilon)$ contribution to the area is always positive. In other words, $\mathcal{A}^*$ increases with γ_{i1}. In cases II, IV and V, the area has some dependence on R_0 and there exists a critical value, $R_0^c = \frac{2}{3}\left(\frac{B^3-A^3}{B^2-A^2}\right)$, such that when $R_0 < R_0^c$ the area increases with γ_{i1} and when $R_0 > R_0^c$ the area decreases with γ_{i1}.

Having obtained the effect of differential growth on the unloaded geometry, we move on to consider its effect on the effective stiffnesses. Throughout the following section, all plots of the asymptotic approximations include the first three terms in the expansion of the relevant quantity (*i.e.* up to $\mathcal{O}(\epsilon^2)$), however the $\mathcal{O}(\epsilon^2)$ terms are omitted from each table for the sake of brevity.

3.5.2 Effective Stiffnesses

The expressions for the $\mathcal{O}(\epsilon)$ contributions to each of the effective stiffnesses and effective material properties are summarised in Appendix A.

First, we consider the axial stiffness. If a cylinder undergoes uniform cross-sectional growth (I or III), then the axial stiffness always increases as a function of γ_{i1}, regardless of the stress-free geometry or strain-energy density. In all other instances of cross-sectional growth (II, IV and V), the behaviour of the axial stiffness depends upon R_0, whilst in the case of axial growth (VI) there is no change in area at $\mathcal{O}(\epsilon)$. The effective Young's modulus of the material can be obtained by normalising

Growth	$\mathcal{O}(\epsilon)$radius, a_1	$\mathcal{O}(\epsilon)$ area
I (CR)	$\frac{A\gamma_{11}\left(A^2-2B^2\log(A)-B^2+2B^2\log(B)\right)}{2\left(A^2-B^2\right)}$	$\pi\gamma_{11}\gamma_{10}\left(B^2-A^2\right)$
II (RR)	$\frac{A\gamma_{11}}{6(A^2-B^2)}\left(3R_0\left(B^2-A^2\right)+6B^2R_0(\log(A)\right.$ $\left.-\log(B))+2(A+2B)(A-B)^2\right)$	$\frac{2}{3}\pi\gamma_{11}\gamma_{10}\left(2(B^3-A^3)\right.$ $\left.-3(B^2-A^2)R_0\right)$
III (CC)	$\frac{A\gamma_{21}\left(A^2+2B^2\log(A)-B^2-2B^2\log(B)\right)}{2\left(A^2-B^2\right)}$	$\pi\gamma_{21}\gamma_{10}\left(B^2-A^2\right)$
IV (RC)	$\frac{A\gamma_{21}}{6(A^2-B^2)}\left(2A^3-3A^2R_0+6B^2R_0(\log(B)\right.$ $\left.-\log(A))+6AB^2+B^2(3R_0-8B)\right)$	$\frac{2}{3}\pi\gamma_{21}\gamma_{10}\left(2(B^3-A^3)\right.$ $\left.-3(B^2-A^2)R_0\right)$
V (CS)	$\frac{A\gamma_{21}\left(2\left(A^2+AB+B^2\right)-3R_0(A+B)\right)}{3(A+B)}$	$\frac{2}{3}\pi\gamma_{21}\gamma_{10}\left(2(B^3-A^3)\right.$ $\left.-3(B^2-A^2)R_0\right)$
VI (RA)	0	0

Table 3.2: $\mathcal{O}(\epsilon)$ terms of the cross-sectional radius and area. In the case of axial growth there is no change in the cross-sectional geometry at this order. In all other cases there is no change only when $R_0 = R_0^c$.

K_{n_3} with respect to the cross-sectional area of the cylinder. For all types of growth considered here, the magnitude of the residual stress in the unloaded configuration is $\mathcal{O}(\epsilon^2)$, whilst the change in cross-sectional area, in all cases except axial growth (VI), is $\mathcal{O}(\epsilon)$. Therefore, growth affects the axial stiffness primarily through its effect on the cross-sectional geometry. This result is illustrated in Figure 3.3. Here we consider Growth Law V and plot the axial stiffness as a function of the incremental growth parameter for three different values of R_0. In this, and all subsequent cases, the material is assumed to be Mooney-Rivlin, and $\bar{W}$ is given by the incompressible form of the relevant expression in Table 2.1:

$$\bar{W} = \frac{\mu_1}{2}(I_1 - 3) + \frac{\mu_2}{2}(I_2 - 3). \tag{3.71}$$

When $R_0 < R_0^c$, increasing γ_{21} increases the cross-sectional area, therefore the axial stiffness increases. Conversely, when $R_0 > R_0^c$, increasing γ_{21} decreases the cross-

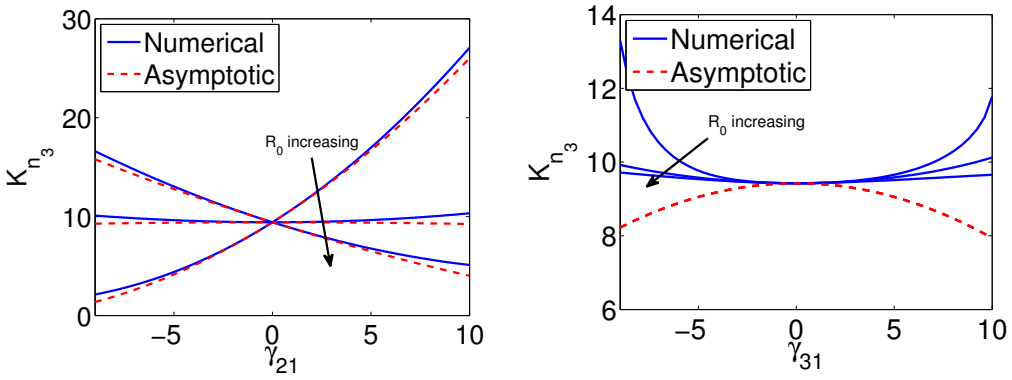

(a) Growth Law V. (b) Growth Law VI.

Figure 3.3: Effective axial stiffness of a Mooney-Rivlin cylinder subject to two different growth laws and three different choices of R_0. In the case of cross-sectional growth, the agreement between the asymptotic approach and numerical results is better than that obtained in the case of axial growth. In both cases $\mu_1 = \mu_2 = \frac{1}{2}$ and $\epsilon = 0.1$.

sectional area, which decreases the axial stiffness. In the case of axial growth, or when $R_0 = R_c$ there is no change in area at $\mathcal{O}(\epsilon)$, therefore the change in axial stiffness is of $\mathcal{O}(\epsilon^2)$. Figure 3.3 also shows the corresponding results obtained numerically, by solving (3.17), first subject to, (3.25) to find approximations of a^*, λ^* and τ^*, and then subject to (3.26) with a small value of N, to find $\hat{a}, \hat{\lambda}$ and $\hat{\tau}$. All quantities can then be substituted into a finite version of (3.33):

$$K_{n_3} \approx \lambda^* \frac{N(\hat{\lambda}) - N(\lambda^*)}{\hat{\lambda} - \lambda^*}. \tag{3.72}$$

When the asymptotic and numerical results are compared, we see that the analytic estimate of K_{n_3} performs well in the case of cross-sectional growth, but is less reliable in the case of axial growth. Furthermore, we see from the numerical results that in the case of axial growth the axial stiffness is dependent upon R_0, but this dependence is not detected by the asymptotic approach to $\mathcal{O}(\epsilon^2)$.

The dependence of the torsional stiffness upon the growth law is not as straightforward as the axial stiffness. In this case, the residual stress is not, in general, zero

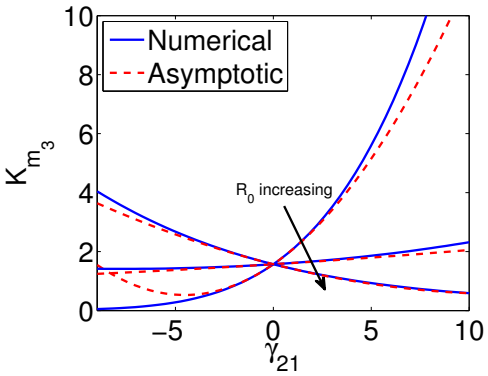

(a) Growth law V, $\mu_1 = \mu_2 = \frac{1}{2}$.

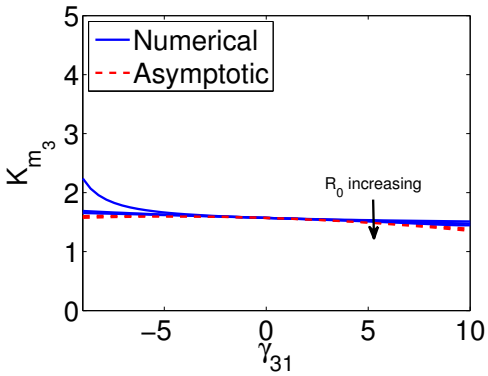

(b) Growth law VI, $\mu_1 = \mu_2 = \frac{1}{2}$.

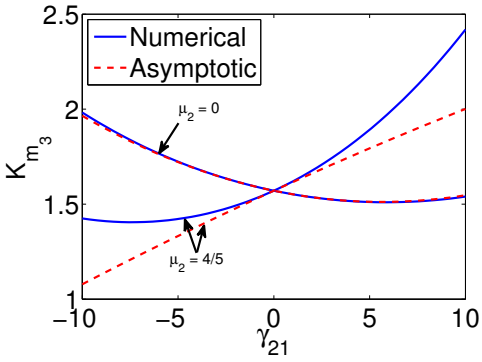

(c) Growth law V, $\mu_1 = 1 - \mu_2$.

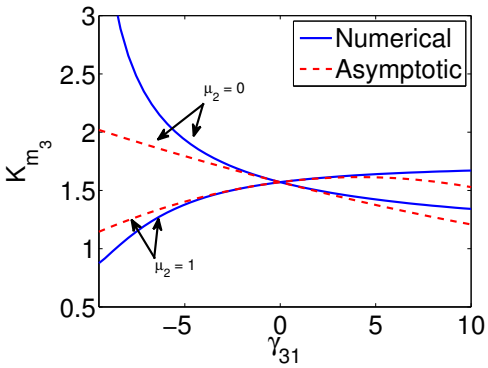

(d) Growth law VI, $\mu_1 = 1 - \mu_2$.

Figure 3.4: Effective torsional stiffness of a Mooney-Rivlin cylinder subject to two different growth laws. In the upper portion three different choices of R_0 are used and the material parameters are fixed, whilst in the lower portion, R_0 is fixed and two choices of material parameters are considered. Unlike the case of axial stiffness, the behaviour of the torsional stiffness is not dominated by the change in geometry. In all cases $\epsilon = 0.1$.

at $\mathcal{O}(\epsilon)$. Therefore, the stiffness may either increase or decrease with the incremental growth parameter, depending upon the choice of strain-energy density and value of R_0. This effect is demonstrated in Figure 3.4. In (a) the behaviour is similar to the axial stiffness: for certain materials the torsional stiffness increases with the area of the cross-section. In (b), we consider axial growth. Here there is a slight decrease in the torsional stiffness as the incremental growth parameter increases, but the change is relatively small. In (c) we see that it is possible to choose the strain-energy density such that growth decreases the cross-sectional area, but increases the torsional stiffness. In (d) we see that in the case of axial growth, the behaviour of the torsional stiffness may either increase or decrease with γ_{31} depending only on the choice of strain-energy, since the change in cross-sectional area is zero at $\mathcal{O}(\epsilon)$.

Finally, we examine the effective bending stiffness, which is illustrated in Figure 3.5. In (a), we see similar behaviour to that shown in Figure 3.4(a): for certain choices of strain-energy density, if the cylinder grows such that the cross-sectional area increases, then the bending stiffness increases. However, by varying the material properties of the cylinder this effect can, in some cases be reversed, as shown in (b). Unlike the torsional stiffness, the bending stiffness always increases with the incremental parameter in the case of Growth Law VI, regardless of the choice of strain-energy density.

3.5.3 Discussion

Our results show that the effective stiffnesses of a residually stressed cylinder depend upon the growth in a non-trivial way. In Figure 3.6 we summarise the effect of differential growth on the effective stiffnesses for a Mooney-Rivlin cylinder subject to Growth Law V. In general, increasing the cross-sectional area of a cylinder, acts to increase the axial, torsional and bending stiffnesses. Similarly, decreasing the cross-sectional area acts to decrease the stiffnesses. However, residual stress can counter

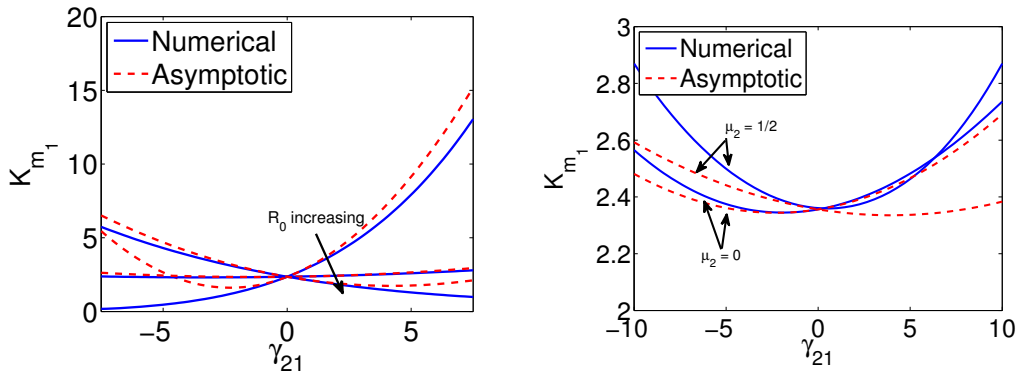

(a) Growth law V, $\mu_1 = \mu_2 = \frac{1}{2}$.

(b) Growth law V, $\mu_1 = 1 - \mu_2$.

Figure 3.5: Effective bending stiffness of a Mooney-Rivlin cylinder subject to two different growth laws. In the upper portion three different choices of R_0 are used and the material parameters are fixed, whilst in the lower portion, R_0 is fixed and two choices of material parameters are considered. As with the torsional stiffness, the behaviour of the torsional stiffness is not dominated by the change in geometry. In both cases $\epsilon = 0.1$.

this effect, so that it is possible to obtain cylinders that have a smaller-cross sectional area following growth, but are more difficult to bend (orange) and/or twist (red). This effect cannot be achieved with stress-free growth, which affects the mechanical properties of a cylinder only through the geometric change it induces.

With uniform growth (no residual stress) the combinations of K_{m_1}, K_{m_3} and K_{n_3} that are possible to attain are restricted. To illustrate this point, we consider the twist-to-bend ratio of a cylinder, which is obtained by taking the ratio of K_{m_3} to K_{m_1}. For an unstressed circular cylinder, this ratio always lies in the region $(\frac{2}{3}, 1)$ [69], so that it is always easier to twist a cylinder than bend it. In Figure 3.7 the twist-to-bend ratio, *i.e.* $\dfrac{K_{m_3}}{K_{m_1}}$, is plotted as a function of the incremental growth for each growth law. In all cases, we find that it is not confined to the range occupied by the twist-to-bend ratio of unstressed compressible cylinders. Moreover, it may increase or decrease with the incremental parameter, depending upon the choice of growth law, and for sufficiently large growth, it is possible to achieve a value greater than 1, so that it becomes easier to bend such a cylinder than twist it. Indeed, this

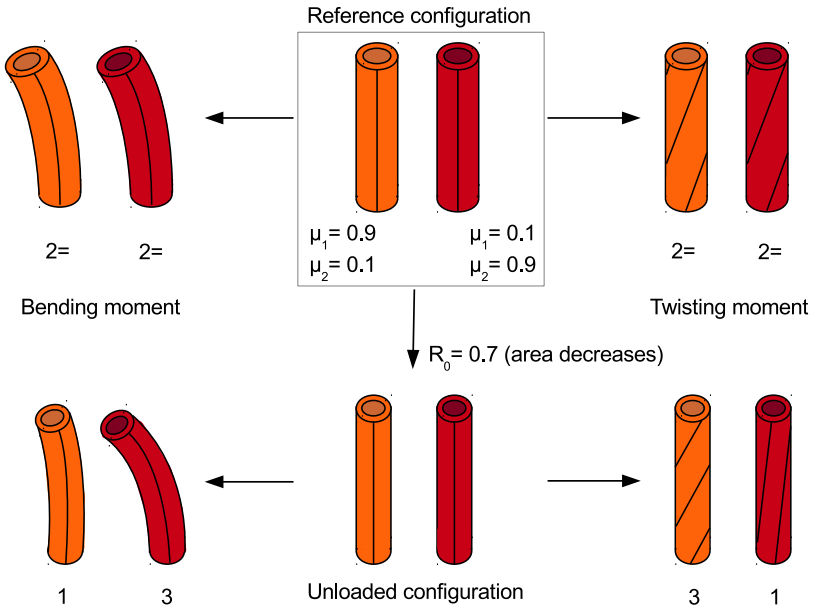

Figure 3.6: Illustration of the various combinations of stiffness that can arise from a single growth law, depending on the material parameters and choice of R_0. In the upper centre we have two geometrically identical cylinders made of a Mooney-Rivlin material. The orange cylinder (l) has material parameters $\mu_1 = 0.9, \mu_2 = 0.1$, whilst the red cylinder (r) has $\mu_1 = 0.1, \mu_2 = 0.9$. Both are subjected to Growth Law V when $R_0 > R_0^c$ (lower centre). Each of the stress-free and residually-stressed configurations is then subject to the same bending moment (left) or twisting moment (right). The resulting cylinders are ranked in order of curvature or twist respectively with 1 denoting the smallest curvature (respectively twist) and 3 the largest. A decrease in the cross-sectional area tends to reduce the stiffness parameters of a cylinder, but this effect can, in certain cases, be reversed by altering the material parameters. For example, the red cylinder less resistant to bending than its unstressed counterpart, whilst the orange cylinder is more resistant. Conversely, the red cylinder more resistant to twisting than its unstressed counterpart, whilst the orange cylinder is less resistant. Axial stiffness always increases with the cross-sectional area.

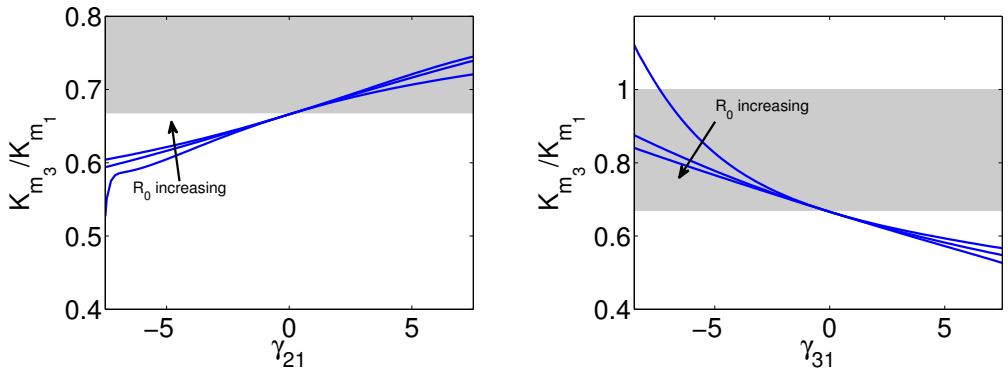

(a) Growth law V

(b) Growth law VI

Figure 3.7: Twist-to-bend ratio plotted as a function of the incremental growth for Growth Laws V and VI. If a cylinder undergoes uniform, isotropic growth then the ratio is confined to the shaded region.

behaviour is observed in many examples of circular plant stem [102]. This example illustrates the idea that filamentary structures are able to utilise differential growth to obtain combinations of material parameters that would not otherwise be attainable by growing uniformly and isotropically. In other words, if we take $K_d \subset \mathbb{R}^3$ to be the set of triples of values, $(K_{m_1}, K_{m_3}, K_{n_3})$ that can be achieved via differential growth and $K_u \subset \mathbb{R}^3$ to be the set of values that can be attained via uniform, isotropic growth only, then $K_u \subset K_d$.

3.6 Inverse Problem

The fact that differential growth allows greater independence of the stiffnesses of an elastic rod leads to an interesting inverse problem. Namely, is it possible for an unstressed cylinder to grow in such a way so as to achieve any desired cross-sectional area and stiffness parameters? To investigate this question, we consider a cylinder subject to a growth law of the following form:

$$\mathbf{G} = \begin{pmatrix} \gamma_{10} & 0 & 0 \\ 0 & \gamma_{10} & 0 \\ 0 & 0 & \gamma_{30} \end{pmatrix} + \epsilon R \begin{pmatrix} \gamma_{11} & 0 & 0 \\ 0 & \gamma_{21} & 0 \\ 0 & 0 & \gamma_{31} \end{pmatrix}. \tag{3.73}$$

As in the previous cases, we consider small perturbations to a uniform, isotropic growth, but we now consider a more general scenario in which all components of the incremental growth tensor are independent. Thus, we have 5 independent growth parameters, $\gamma_{10}, \gamma_{30}, \gamma_{11}, \gamma_{21}$ and γ_{31}. For simplicity we assume the cylinder is made from a neo-Hookean material with shear modulus μ. Applying the growth law (3.73) and using the same method as that described in earlier in this chapter, we obtain the following analytic expressions for the outer radius and stiffnesses:

$$\begin{aligned} \lambda^* = {} & \gamma_{30} + \frac{2B\gamma_{31}\delta}{3} \\ & + \frac{B^2\delta^2\left(\gamma_{31}^2\gamma_{10}^2 + 2\gamma_{11}\gamma_{31}\gamma_{10}\gamma_{30} + 14\gamma_{21}\gamma_{31}\gamma_{10}\gamma_{30} + 4\gamma_{11}^2\gamma_{30}^2 - 16\gamma_{11}\gamma_{21}\gamma_{30}^2 + 16\gamma_{21}^2\gamma_{30}^2\right)}{108\gamma_{10}^2\gamma_{30}}, \end{aligned} \tag{3.74}$$

$$\begin{aligned} b^* = {} & B\gamma_{10} + \frac{1}{3}B^2\gamma_{11}\delta \\ & + \frac{B^3\delta^2\left(-\gamma_{31}^2\gamma_{10}^2 + 4\gamma_{11}\gamma_{31}\gamma_{10}\gamma_{30} - 8\gamma_{21}\gamma_{31}\gamma_{10}\gamma_{30} - 16\gamma_{11}^2\gamma_{30}^2 + 70\gamma_{11}\gamma_{21}\gamma_{30}^2 - 16\gamma_{21}^2\gamma_{30}^2\right)}{216\gamma_{10}\gamma_{30}^2}, \end{aligned} \tag{3.75}$$

$$\begin{aligned} K_{m_1} = {} & \frac{3}{4}\pi B^4\gamma_{10}^4\mu + \pi\mu B^5\gamma_{10}^3\delta\frac{17\gamma_{31}\gamma_{10} + 26\gamma_{11}\gamma_{30} + 23\gamma_{21}\gamma_{30}}{30\gamma_{30}} + \frac{\pi\gamma_{10}^2B^6\mu\delta^2}{2160\gamma_{30}^2}\left(317\gamma_{31}^2\gamma_{10}^2\right. \\ & \left.+1258\gamma_{11}\gamma_{31}\gamma_{10}\gamma_{30} + 886\gamma_{21}\gamma_{31}\gamma_{10}\gamma_{30} + 500\gamma_{11}^2\gamma_{30}^2 + 2608\gamma_{11}\gamma_{21}\gamma_{30}^2 + 344\gamma_{21}^2\gamma_{30}^2\right), \end{aligned} \tag{3.76}$$

$$\begin{aligned} K_{m_3} = {} & \frac{1}{2}\pi B^4\gamma_{10}^4\mu - \frac{2\pi\mu B^5\gamma_{10}^3\delta\left(\gamma_{31}\gamma_{10} - 5\gamma_{11}\gamma_{30} - 5\gamma_{21}\gamma_{30}\right)}{15\gamma_{30}} \\ & + \frac{\delta^2\pi\mu B^6\gamma_{10}^2\left(2\gamma_{31}^2\gamma_{10}^2 - 3\gamma_{11}\gamma_{31}\gamma_{10}\gamma_{30} - 3\gamma_{21}\gamma_{31}\gamma_{10}\gamma_{30} + 4\gamma_{11}^2\gamma_{30}^2 + 17\gamma_{11}\gamma_{21}\gamma_{30}^2 + 4\gamma_{21}^2\gamma_{30}^2\right)}{18\gamma_{30}^2}, \end{aligned} \tag{3.77}$$

$$\begin{aligned} K_{n_3} = {} & 3\pi B^2\gamma_{10}^2\mu + 2\pi\mu B^3\gamma_{10}\delta\left(\gamma_{11} + \gamma_{21}\right) \\ & + \frac{\pi\mu B^4\delta^2\left(7\gamma_{31}^2\gamma_{10}^2 - 4\gamma_{11}\gamma_{31}\gamma_{10}\gamma_{30} + 8\gamma_{21}\gamma_{31}\gamma_{10}\gamma_{30} + 4\gamma_{11}^2\gamma_{30}^2 + 38\gamma_{11}\gamma_{21}\gamma_{30}^2 + 16\gamma_{21}^2\gamma_{30}^2\right)}{36\gamma_{30}^2}. \end{aligned} \tag{3.78}$$

In the forward approach, specifying values for each growth parameter uniquely determines the stiffnesses $K_{m_1}, K_{m_3}, K_{n_3}$, axial stretch, λ^* and outer radius, b^*. In the

inverse problem, we select values of $K_{m_1}, K_{m_3}, K_{n_3}, \lambda^*$ and b^*, and seek the values of the growth parameters (if they exist) for which the system (3.74)-(3.78) is satisfied. For the overall deformation to be compatible, J must be non-zero at all points in the body, and this requirement places the following restrictions on the permitted parameter values:

$$\gamma_{10} > 0 \tag{3.79}$$

$$\gamma_{30} > 0 \tag{3.80}$$

$$\epsilon B\gamma_{11} > -\gamma_{10} \tag{3.81}$$

$$\epsilon B\gamma_{21} > -\gamma_{10} \tag{3.82}$$

$$\epsilon B\gamma_{31} > -\gamma_{30} \tag{3.83}$$

Due to the complexity of the governing equations, we do not attempt an analytic proof of existence of a solution. However, we demonstrate numerically that solutions of the inverse problem satisfying (3.79)-(3.83), can be found. As in the previous section, we specify the reference geometry and material properties, $B = 1,\ \mu = 1$, as well as setting $\delta = 0.1$. We consider the three cases in which the unloaded cylinder is more difficult to (i) stretch axially; (ii) twist; (iii) bend than its unstressed counterpart. To do so, we seek growth parameters for which K_{n_3}, K_{m_3} and K_{m_1}, respectively, are 10% greater than in the unstressed counterpart, whilst all other parameters are unchanged. In all instances, we will assume the reference and unloaded configurations are geometrically identical. That is, $b^* = 1, \lambda^* = 1$. The following results were obtained using the solver `NSolve` in *Wolfram Mathematica 10*. In each case, the resulting growth profiles are plotted in Figure 3.8.

Case (i): Increased axial stiffness

In this case, we require the grown cylinder to have a greater axial stiffness than the unstressed cylinder, but maintain the same torsional and bending stiffnesses. One set of growth parameters that yield this state are $\gamma_{10} = 0.69, \gamma_{30} = 0.82, \gamma_{11} = 5.81, \gamma_{21} = 4.58, \gamma_{31} = 2.28$. This solution corresponds to the inner regions of the cylinder undergoing resorption in all directions, whilst the outer regions undergo growth in all directions, as depicted in Figure 3.8(a).

Case (ii): Increased torsional stiffness

In this case, we require the grown cylinder to have a greater torsional stiffness than the unstressed cylinder, but maintain the same axial and bending stiffnesses. A possible solution is $\gamma_{10} = 1.20, \gamma_{30} = 1.19, \gamma_{11} = -3.20, \gamma_{21} = -2.96, \gamma_{31} = -3.02$. Here, the growth profiles in all directions are similar (see Figure 3.8(b)). The inner regions undergo growth in all directions, whilst the outer regions undergo resorption in all directions.

Case (iii): Increased bending stiffness

In this case, we require the grown cylinder to have a greater bending stiffness than the unstressed cylinder, but maintain the same axial and torsional stiffnesses. Here, we find the solution $\gamma_{10} = 1.10, \gamma_{30} = 0.99, \gamma_{11} = -1.57, \gamma_{21} = -1.55, \gamma_{31} = 0.15$.. In the inner regions we have growth in the radial and circumferential directions, whilst in the outer regions we have resorption in these directions. There is very little growth in the axial direction, with the inner regions subject to slight resorption and the outer regions subject to slight growth.

It is also worth noting that in some circumstances the solver found no admissible solutions (*i.e.* those satisfying (3.79)-(3.83)). The absence of solutions may be due

to the fact that `NSolve` failed, though it could also be attributed to the fact that our asymptotic approximations are only valid to $\mathcal{O}(\epsilon)$, and a solution may be found if more terms are considered. On the other hand, it may indeed be true that no solution exists, which indicates that the stiffness parameters and unloaded geometry have some dependence upon one another, for our choice of growth law.

In addition to finding no admissible solutions, in some circumstances, it was possible to find multiple solutions of the inverse problem. For example, if we seek a growth law for which the radius and length are increased by 10%, the torsional stiffness is reduced by 10% and the bending stiffness is increased by 30%, whilst the axial stiffness is unchanged, the following numerical values are found

$$\gamma_{10} = 0.83, \quad \gamma_{30} = 0.32, \quad \gamma_{11} = -8.17, \quad \gamma_{21} = 4.00, \quad \gamma_{31} = 10.00, \tag{3.84}$$

and

$$\gamma_{10} = 1.06, \quad \gamma_{30} = 0.88, \quad \gamma_{11} = -2.54, \quad \gamma_{21} = 0.59, \quad \gamma_{31} = 3.23. \tag{3.85}$$

Before we continue, it must be noted that of the two solutions found, the values obtained in (3.84) represent a rather extreme growth profile: the incremental parameters are up to one order of magnitude larger than the uniform growth parameters, which violates our assumption that the perturbation to uniform growth is small. However, in principle, the existence of multiple solutions of the inverse problem is not surprising, because the theory of Kirchhoff rods takes into account only the average cross-sectional stresses. Thus if two different cross-sectional stress profiles are the same, on average, they yield the same effective stiffnesses. The solutions (3.84) and (3.85) show this behaviour clearly and are given primarily as illustrative examples.

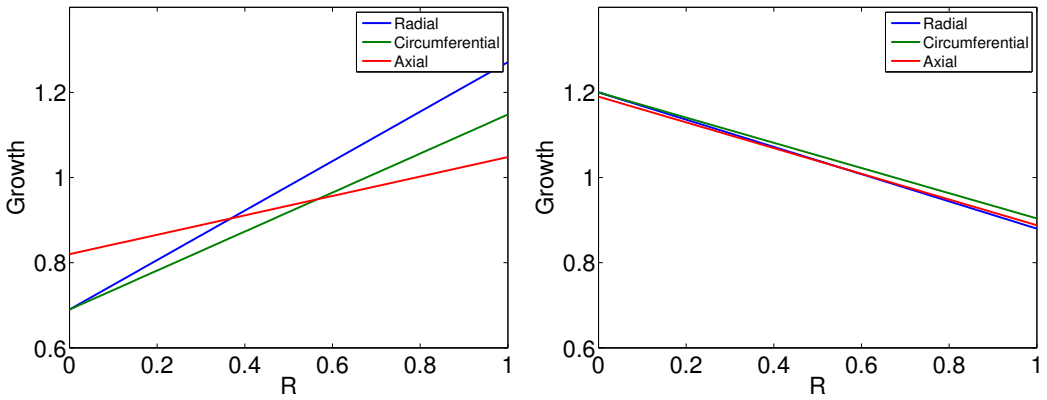

(a) Axial stiffness

(b) Torsional stiffness

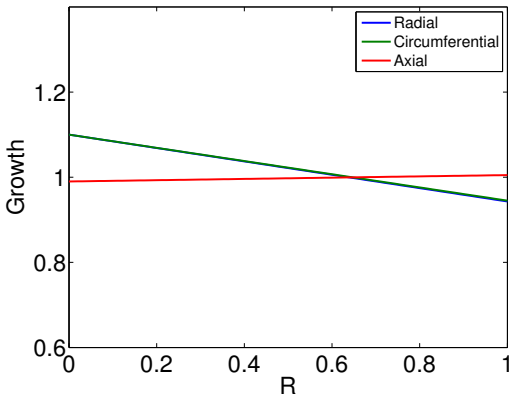

(c) Bending stiffness

Figure 3.8: Growth laws required to produce a 10% increase in the relevant stiffness whilst maintaining the same geometry and other stiffnesses as the unstressed cylinder. In each case the growth laws are of the form $\gamma_i = \gamma_{i0} + \epsilon R \gamma_{i1}$, with $\gamma_{10} = \gamma_{20}$.

3.7 Conclusion

In this chapter we have taken the initial steps towards a means of incorporating residual stress in rod-theory problems. This link is established by deriving effective mechanical properties of a residually-stressed, isotropic cylinder using the theory of 3-D, non-linear elasticity and using these effective properties as parameters in the constitutive law of an analogous rod model. The method is general in the sense that it yields expressions for the effective stiffnesses in terms of any annular stress-free geometry and isotropic strain-energy density. In most cases, the asymptotic approximations show good agreement with the corresponding numerical results, though the level of agreement is dependent on the choice of strain-energy density, particularly in the case of axial growth.

We have also gained insight into the possible roles of residual stress and cross-sectional geometry in determining the mechanical behaviour of cylindrical biological structures. This interplay between the geometry and effective stiffnesses of a cylinder allows for a wider range of structures to be obtained than in the case of uniform, isotropic growth, such as those with a smaller area, but higher bending or torsional stiffness than those of their unstressed counterparts. In the case of the uniaxial loading, it is the area of the cross- section that dominates the behaviour of the effective stiffness, unless growth occurs in the axial direction only.

By means of an inverse problem formulation, we have demonstrated that, in some instances, we are able to prescribe a set of geometric and mechanical properties and find a growth law that achieves these desired parameters. Furthermore, it is possible for two different growth laws to give rise to the same rod theory model, if the resulting cross-sectional stresses are, on average, the same.

In the next chapter, we continue the theme of forging links between 3-D elasticity and rod theory. We do so by considering a problem that is common to many biological scenarios: that of a slender filament surrounded by an elastic medium, buckling under

compression. The surrounding material acts as a transverse reinforcement to the filament and can significantly alter its axial stability and post-buckling behaviour. However, it difficult to relate the degree of reinforcement to the known material properties of the rod. We will discuss drawbacks of current techniques used to estimate the degree of transverse reinforcement and suggest a new estimate of this foundation parameter. As in this chapter, we use theory of 3-D elasticity to inform parameter choices of the analogous rod model.

Chapter 4

Growth-Induced Buckling of a Two-Layer Cylinder

4.1 Introduction

In the previous chapter we examined the mechanical properties of an elastic cylinder, consisting of a single layer of homogeneous material, subject to a non-uniform growth profile, which generates residual stress. In this chapter we consider the effects of multiple layers of tissue, which do not necessarily have the same elastic properties. This work is based upon the publication "Growth-induced axial buckling of a slender elastic filament embedded in an isotropic elastic matrix", by O'Keeffe *et al.* (*Int. J. Nonlin. Mech.* **56**:94–104 (2013)) [74]. We will assume that each layer grows uniformly and that residual stress is generated by a mismatch in the growth rates of each layer. We restrict our attention to the case in which the axial growth of the inner layer is greater than that of the outer layer, giving rise to a situation in which the inner layer is axially compressed. Such situations are readily found throughout the natural world, and include plant roots growing in soil, microtubules embedded within the cytoplasm and blood vessels surrounded by body tissue. A simple modelling

approach that can be applied to each of these scenarios is to treat the surrounding material as an elastic foundation, which provides the inner filament with transverse reinforcement. Many studies of such embedded slender structures make use of the classical Euler beam theory [21] in order to study the onset of buckling under the action of a compressive force. Murmu and Pradhan [70] used Timoshenko beam theory (an extension of Euler beam theory) to investigate the effect of various types of elastic foundation on the critical longitudinal buckling stress (*i.e.* the compressive stress at which the tube buckles) of embedded single-walled carbon nanotubes. Their analysis made use of a foundation modulus parameter, k_f, which characterises the amount of transverse reinforcement of the foundation acting on the tube [107, 106, 24]. They found that the critical buckling pressure increases with k_f, although no information is given on how the parameter k_f can be measured for a specific material. Brangwynne *et al.* performed buckling experiments on microtubules. They applied axial loads to microtubules by two different means. First, they observed that under small axial loads, microtubules excised from the cell exhibited Euler-type buckling [13]. However, when embedded within the cytoplasm microtubules were able to withstand a greater compressive force (imposed by applying a normal force at the point where the microtubule meets the cell membrane) before the onset of buckling. Moreover, once buckling did occur, the observed wavelength was shorter than when isolated microtubules were considered. The authors also carried out a theoretical analysis by treating a microtubule as a cylindrical, inextensible beam embedded within an elastic foundation. They proposed that the observed buckling mode is that which minimises the sum of the beam's bending energy and the energy required to transversely displace the surrounding cytoplasm. Their analysis uses the parameter α to characterise the transverse reinforcement of the cytoplasm, and they estimate this parameter in terms of the radius of the rod, a, the Young's modulus of the surrounding matrix, G,

and the characteristic buckling length scale of the structure, l as follows:

$$k_{e1} = \frac{4\pi G}{\log\left(\frac{l}{a}\right)}. \tag{4.1}$$

This estimate was first derived in 1967 by Herrmann *et al.* [45] and has also been used in various other experimental studies [92]. However, from a theoretical point of view, this approach is problematic, since the wavelength l is not known *a priori*. Therefore this estimate cannot be used in any predictive way. An alternative estimate of this parameter, where the wavelength is replaced by the length L of the beam, was presented in [88], and given by

$$k_{e2} = \frac{4\pi G}{\log\left(\frac{L}{a}\right)}. \tag{4.2}$$

As we will see, this estimate cannot be correct, as the buckling properties of a sufficiently long filament in a matrix are essentially independent of the length of the beam. By comparing the exact buckling properties of a cylinder under axial load in an infinite matrix with the properties of a Kirchhoff rod on an elastic foundation our aim is to derive a new estimate for the foundation modulus parameter in terms of the known properties of the system.

4.1.1 The Problem

We consider the problem of a transversely isotropic, elastic filament embedded in an isotropic, elastic matrix. The filament and matrix are constrained in the axial direction by two flat, rigid platens and the filament undergoes uniform axial growth, so that it becomes axially compressed. At a critical growth, the filament buckles. We model this problem firstly by considering volumetric growth in a 3-D, elastic body. This approach has been used in a number of previous studies of axial and circumferential buckling of hollow multi-layered cylinders with finite radii [35, 99, 100,

66], and exploits the idea of multiplicative decomposition of the deformation tensor introduced in Chapter 2. For the case of a neo-Hookean filament and neo-Hookean matrix we are able to estimate the critical growth value analytically via the use of the WKB method. Secondly, we consider a rod theory formulation that models the system as a 2-D elastic beam embedded in a Winkler foundation. Like previous rod theory models, this approach makes use of a foundation modulus parameter. Each approach provides us with an estimate of the critical axial growth of the filament and the wavelength of the resulting buckled state. The goal of this chapter is to describe this buckling instability and obtain an estimate of the foundation modulus parameter by comparing the results of the two approaches. This foundation modulus parameter is directly related to the geometric and material properties of the system. Furthermore, we show that the generalisation to a Mooney-Rivlin matrix does not alter this estimate.

4.2 The Two-Layer Cylinder

We consider a two-layer, solid cylinder constrained axially between two rigid platens. The setup is similar to that described in Chapter 3: points in $\mathcal{B}_0$, are described by (3.1), with $0 \leq R \leq C$, $0 \leq Z \leq L_0$, with the difference that a material boundary exists at $R = B$, where $0 \leq B \leq C$. We first consider the mechanics and geometry of the axisymmetric solution prior to bifurcation. Under this assumption, the body occupies the current configuration $\mathcal{B}_f$ defined by (3.2), with $\tau = 0,\ 0 \leq r \leq c$ and $0 \leq z \leq l$. We use b and c to denote the material boundaries in the deformed configuration, *i.e.* $b = r(B)$ and $c = r(C)$. The presence of the rigid platens requires that $l = L_0$ so that $\lambda = 1$. This restriction on the axial stretch is used instead of a boundary condition on the axial load analogous to that in (3.26). Furthermore, we do not consider twisting of the cylinder, so the deformation gradient is simply given

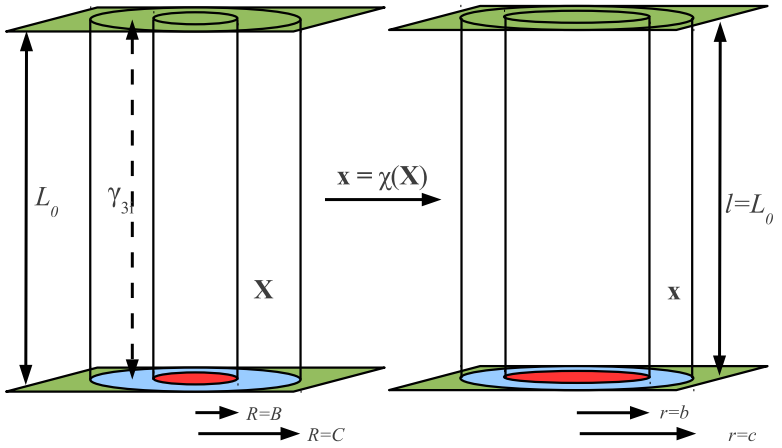

Figure 4.1: Illustration of the axisymmetric deformation of a two-layer cylinder subject to axial differential growth. Capitals denote quantities defined with the respect to the reference configuration, $\mathcal{B}_0$ (left), while lower case characters denote the same quantities defined in terms of the current configuration, $\mathcal{B}_f$ (right). We are primarily interested in the zero-extension case, therefore we set $l = L_0$.

by

$$\mathbf{F}^{(0)} = \text{diag}\left(\frac{dr}{dR}, \frac{r}{R}, 1\right). \tag{4.3}$$

The deformation is shown schematically in Figure 4.1. For convenience, we introduce the superscript $^{(0)}$ to denote the axisymmetric deformation for consistency with the notation in Chapter 2.2. We prescribe constant axial growth in the inner layer, denoted by the parameter γ and allow no growth or resorption to occur in the other two directions, nor in any direction in the outer layer. Therefore, the growth tensor is given by

$$\mathbf{G} = \text{diag}(1, 1, \gamma_3), \quad \gamma_3 = \begin{cases} \gamma, & 0 \leq R \leq B, \\ 1, & B < R \leq C, \end{cases} \tag{4.4}$$

and the elastic response tensor is given by

$$\mathbf{A}^{(0)} = \text{diag}(\alpha_1, \alpha_2, \alpha_3). \tag{4.5}$$

From (4.4)-(4.5) and (2.4), the variables α_j are given by

$$\alpha_1 = r', \quad \alpha_2 = \frac{r}{R}, \quad \alpha_3 = \frac{1}{\gamma_3}. \tag{4.6}$$

Initially, we shall assume that both layers are neo-Hookean, and we define the strain-energy density to be

$$W = \begin{cases} W_i, & 0 \leq R \leq B, \\ W_o, & B < R \leq C, \end{cases} \tag{4.7}$$

where

$$W_{i,o}\left(\alpha_1, \alpha_2, \alpha_3\right) = \frac{\mu_{i,o}}{2}(\alpha_1^2 + \alpha_2^2 + \alpha_3^2 - 3), \tag{4.8}$$

and $\mu_{i,o}$ are the shear moduli of each layer. Utilising the incompressibility condition (2.30), it follows that $\alpha_1\alpha_2\alpha_3 = 1$. We can then rewrite $W_{i,o}$ as follows:

$$W_{i,o}\left(\frac{1}{\alpha_2\alpha_3}, \alpha_2, \alpha_3\right) = \hat{W}_{i,o}(\alpha_2, \alpha_3) = \frac{\mu_{i,o}}{2}\left(\frac{1}{\alpha_2^2\alpha_3^2} + \alpha_2^2 + \alpha_3^2 - 3\right). \tag{4.9}$$

As in Chapter 3, we neglect any time-dependence. Then, the only non-trivial equation arising from the equations of static, mechanical equilibrium is (3.17). Substitution of (4.9) into (3.17) then gives

$$\frac{dT_{rr}}{dr} = \frac{\alpha_2}{r}\frac{\partial \hat{W}_{i,o}}{\partial \alpha_2}, \tag{4.10}$$

which can be integrated to yield

$$T_{rr}(r) = \begin{cases} T_{rr}(b) - \displaystyle\int_b^r \frac{\alpha_2}{r}\frac{\partial \hat{W}_i}{\partial \alpha_2}\,\mathrm{d}r, & 0 \leq r \leq b, \\ \displaystyle -\int_c^r \frac{\alpha_2}{r}\frac{\partial \hat{W}_o}{\partial \alpha_2}\,\mathrm{d}r, & b \leq r \leq c. \end{cases} \tag{4.11}$$

At the boundary between the inner and outer layer ($r = b$), we require the displacement and the radial stress to be continuous. On the outer radius of the cylinder ($r = c$), we impose the condition (2.13) with $\hat{\mathbf{n}} = \mathbf{e}_r$ and $\hat{\mathbf{t}} = \mathbf{0}$. Therefore, the

boundary conditions are as follows

$$T_{rr}(c) = 0, \tag{4.12}$$

$$[T_{rr}]_{r=b} = 0. \tag{4.13}$$

The incompressibility equation (2.30) can be integrated directly to give

$$r = \begin{cases} \sqrt{\gamma}R, & 0 \leq R \leq B, \\ \sqrt{b^2 + (R^2 - B^2)}, & B \leq R \leq C. \end{cases} \tag{4.14}$$

4.3 Incremental Equations

As in the previous chapter, we investigate the axial stability of the axisymmetric solution by applying a small perturbation, belonging to a class of deformation with no prescribed axial symmetry. We denote the components of the incremental deformation, $\boldsymbol{\chi}^{(1)}$, in polar co-ordinates as $(u(r,\theta,z), v(r,\theta,z), w(r,\theta,z))^T$. This gives the following expression for $\mathbf{A}^{(1)}$:

$$\mathbf{A}^{(1)} = \text{grad}\boldsymbol{\chi}^{(1)} = \begin{pmatrix} u_r & \dfrac{u_\theta - v}{r} & u_z \\ \\ v_r & \dfrac{u + v_\theta}{r} & v_z \\ \\ w_r & \dfrac{w_\theta}{r} & w_z \end{pmatrix}, \tag{4.15}$$

where subscripts denote differentiation with respect to the relevant variable. The incompressibility condition leads to the relation

$$\text{tr } \mathbf{A}^{(1)} = u_r + \frac{u + v_\theta}{r} + w_z = 0. \tag{4.16}$$

Unlike the previous chapter, we have no prior expectation of the buckling mode of the filament. Furthermore, it is convenient to work in terms of the deformed variables r, θ and z, because the form of the finite deformation is known completely, once the parameter γ has been specified. We therefore seek static solutions of (2.41) (neglecting body forces) that are oscillatory in θ and z:

$$u = f(r)\cos(m\theta)\cos(\alpha z), \tag{4.17}$$

$$v = g(r)\sin(m\theta)\cos(\alpha z), \tag{4.18}$$

$$w = h(r)\cos(m\theta)\sin(\alpha z), \tag{4.19}$$

$$p_1 = k(r)\cos(m\theta)\cos(\alpha z), \tag{4.20}$$

where $\alpha = n\pi/L_0, n \in \mathbb{N}$ and m is the mode number, chosen to be a non-negative integer so that displacements are single-valued. The values of m and n determine the type of buckling that occurs. If $m = 0$ and $n \geq 1$, the centreline of the cylinder remains straight and we obtain radially symmetric solutions, but a 'barrelling' effect is observed. If $m = 1$ and $n \geq 1$ then the cross-section of the cylinder remains circular, however the centreline ceases to be straight. Finally, if $m \geq 2$ we observe circumferential buckling, with m nodes visible in the cross-section. Axial oscillations are possible when $n \geq 1$. Each of these cases has been studied previously. For example, Moulton and Goriely examined the case of cross-sectional buckling ($m \geq 1, n = 0$) as a result of radial growth [67]. MacLaurin *et al.* studied combinations of axial and circumferential modes $m \geq 1, n \geq 1$ arising in tumour capillaries due to the rapid growth of malignant cells [61]. Goriely and Vandiver investigated the axial stability of growing arteries ($m = 1, n \geq 1$) [35]. In 2008, Goriely *et al.* studied the effect of geometry on the type of buckling observed for a one-layer, neo-Hookean cylinder [36]. They found that in the regime of a slender, solid cylinder, instability will always develop in the axial direction before the circumferential direction. Using

this information, we make the ansatz that, in the two-layer case, an axial buckling mode will be the observed buckling mode, therefore we set $m = 1$.

Substitution of (4.17)-(4.20) into the static form of (2.41) and setting $\mathbf{b}^{(1)} = \mathbf{0}$ then results in the following system of ordinary differential equations

$$\begin{aligned} k' &= (r(\mathcal{L}'_{2211} - \mathcal{L}'_{3311}) - \mathcal{L}_{2222} + \mathcal{L}_{2233} - \mathcal{L}_{2121} + \mathcal{L}_{1331})g/r^2 \\ &\quad + (\mathcal{L}_{2112} + \mathcal{L}_{2211} - \mathcal{L}_{1331} - \mathcal{L}_{3311})g'/r + (\mathcal{L}_{1111} - \mathcal{L}_{3311} - \mathcal{L}_{1331})f'' \\ &\quad + (r(\mathcal{L}'_{1111} + p'_0 - \mathcal{L}'_{3311}) + \mathcal{L}_{1111} - 2\mathcal{L}_{3311} + \mathcal{L}_{2233} - \mathcal{L}_{1331})f'/r \\ &\quad + (r(\mathcal{L}'_{2211} - \mathcal{L}'_{3311}) - \mathcal{L}_{2222} + \mathcal{L}_{2233} + \mathcal{L}_{1331})f/r^2 - \mathcal{L}_{2121}f/r^2 - \alpha^2\mathcal{L}_{3131}f, \end{aligned} \tag{4.21}$$

$$\begin{aligned} r\mathcal{L}_{1212}g'' &= -k + (r\mathcal{L}'_{1212} + \mathcal{L}_{1212} + \mathcal{L}_{2222} - \mathcal{L}_{2233} - \mathcal{L}_{3223})f/r \\ &\quad + (r\mathcal{L}'_{1212} + \mathcal{L}_{1212})g/r + (\mathcal{L}_{2222} - \mathcal{L}_{2233} - \mathcal{L}_{3223})g/r \\ &\quad + r\alpha^2\mathcal{L}_{3232}g + (\mathcal{L}_{2211} - \mathcal{L}_{2233} - \mathcal{L}_{3223} + \mathcal{L}_{1221})f' - (r\mathcal{L}_{1212} + \mathcal{L}_{1212})g', \end{aligned} \tag{4.22}$$

$$\begin{aligned} \mathcal{L}_{1313}f''' &= (f' + (g+f)/r)\mathcal{L}_{2323}/r^2 - (r\mathcal{L}'_{1331} + rp'_0 + \mathcal{L}_{1331} - \mathcal{L}_{2332})\alpha^2 f/r \\ &\quad - \mathcal{L}_{1313}((f'' + g'')/r - 2(f' + g')/r^2 + 2(f+g)/r^3) \\ &\quad + (\mathcal{L}_{3333} - \mathcal{L}_{2332} - \mathcal{L}_{2233})\alpha^2(f+g)/r + (\mathcal{L}_{3333} - \mathcal{L}_{3311} - \mathcal{L}_{1331})\alpha^2 f' \\ &\quad - (r\mathcal{L}'_{1313} + \mathcal{L}_{1313})(f'' + (f' + g')/r - (f+g)/r^2)/r - \alpha^2 k. \end{aligned} \tag{4.23}$$

These are essentially the same as (3.51)-(3.53), with the difference that they are written in terms of r, as opposed to R. The incremental ambient pressure is zero, so applying (2.42) we have the following three boundary conditions at $r = c$

$$(\mathcal{L}_{1122} - \mathcal{L}_{1133})(f+g) + \left(\mathcal{L}_{1111} - \mathcal{L}_{1133} + \alpha_1\frac{\partial W}{\partial \alpha_1}\right)rf' - rk = 0, \tag{4.24}$$

$$rg' - g - f = 0, \tag{4.25}$$

$$r^2 f'' + rf' + \alpha^2 r^2 f = 0. \tag{4.26}$$

At the interface between the two layers, we assume a continuous deformation without slippage. Thus we have the following at $r = b$

$$f_i = f_o, \tag{4.27}$$

$$g_i = g_o, \tag{4.28}$$

$$f_i' = f_o'. \tag{4.29}$$

Furthermore, we require the radial stress at the interface to be continuous. Therefore

$$\begin{aligned}(\mathcal{L}_{1122_i} - \mathcal{L}_{1133_i})(f_i + g_i) + \left(\mathcal{L}_{1111_i} - \mathcal{L}_{1133_i} + \alpha_{1_i}\frac{\partial W_i}{\partial \alpha_{1_i}}\right) r f_i' - r k_i \\ = (\mathcal{L}_{1122_o} - \mathcal{L}_{1133_o})(f_o + g_o) + \left(\mathcal{L}_{1111_o} - \mathcal{L}_{1133_o} + \alpha_{1_o}\frac{\partial W_o}{\partial \alpha_{1_o}}\right) r f_o' - r k_o,\end{aligned} \tag{4.30}$$

$$\mathcal{L}_{1212_i}(r g_i' - g_i - f_i) = \mathcal{L}_{1212_o}(r g_o' - g_o - f_o), \tag{4.31}$$

$$\begin{aligned}&\mathcal{L}_{1313_i}(r^2 f_i'' + r f_i' + (\alpha^2 r^2 - 1) f_i + r g_i' - g_i) \\ &\quad = \mathcal{L}_{1313_o}(r^2 f_o'' + r f_o' + (\alpha^2 r^2 - 1) f_o + r g_o' - g_o).\end{aligned} \tag{4.32}$$

Finally, we demand that all solutions remain bounded as $r \to 0$.

4.3.1 Numerical Solutions

As in Chapter 3, we simplify equations (4.21)-(4.23) by eliminating k. This results in a six-dimensional system of equations that can be written in a form similar to (3.57)

$$\mathbf{y}' = \mathbf{f}(\mathbf{y}; r), \quad \mathbf{y} \in \mathbb{R}^6, \tag{4.33}$$

where $\mathbf{y}= (f, f', f'', g, g', g'')$. The radial stresses must remain bounded as $r \to 0$. Therefore the functions f, g and k must be 'well-behaved' as $r \to 0$, *i.e.* we demand bounded approximations of f, g and k close to zero for which the incremental equi-

librium equations are satisfied. We proceed by seeking f and g of the form

$$f = Q_1 r^{\nu_1}, \quad g = Q_2 r^{\nu_2}. \tag{4.34}$$

We substitute these expressions into (4.21)-(4.23) and eliminate the terms that do not decay as $r \to 0$ by setting the coefficients of such terms to be zero. There are three cases to consider; they are $\nu_1 > \nu_2$, $\nu_1 = \nu_2$ and $\nu_1 < \nu_2$. Each gives rise to an admissible expression for both f and g. Combining these expressions then yields

$$f \sim a_1 r^2 + b_1, \quad g \sim a_1 r^2 - b_1, \quad \text{as } r \to 0, \tag{4.35}$$

where a_1, a_2 and b_1 are constants. The remaining boundary conditions comprise a set of 9 linear functions $c_{1,\ldots,9}(\mathbf{y}(r); r)$:

$$c_{1,2,3}(\mathbf{y}_o(c); c) = 0, \quad c_{4,5,6,7,8,9}(\mathbf{y}_i(b); b) = c_{4,5,6,7,8,9}(\mathbf{y}_o(b); b). \tag{4.36}$$

The determinant method can be used to find values of γ for which non-trivial solutions exist. We make three copies of the system (4.33) with linearly independent conditions of the form (4.35) as $r \to 0$. For our system, $\mathbf{y}^{(i)}, \quad i = 1, 2, 3$, are given by

$$\mathbf{y}^{(i)} \sim (f^{(i)}, f^{(i)\prime}, f^{(i)\prime\prime}, g^{(i)}, g^{(i)\prime}, g^{(i)\prime\prime}), \quad r \to 0, \tag{4.37}$$

where

$$f^{(1)} = r^2, \quad g^{(1)} = 0, \tag{4.38}$$

$$f^{(2)} = 1, \quad g^{(2)} = -1, \tag{4.39}$$

$$f^{(3)} = 0, \quad g^{(3)} = r^2. \tag{4.40}$$

We integrate this system up to $r = b$ and use the boundary conditions at the interface (4.36(b)), together with the end values $\mathbf{y}_i^{(j)}(b), \quad j = 1, 2, 3$, to obtain the initial conditions $\mathbf{y}_o^{(j)}(b), \quad j = 1, 2, 3$. We then integrate up to $r = c$ and evaluate the 3×3 determinant of boundary conditions at $r = c$ given by

$$\Delta(\gamma) = \begin{vmatrix} c_1(\mathbf{y}_o^{(1)}(c);\gamma) & c_2(\mathbf{y}_o^{(1)}(c);\gamma) & c_3(\mathbf{y}_o^{(1)}(c);\gamma) \\ c_1(\mathbf{y}_o^{(2)}(c);\gamma) & c_2(\mathbf{y}_o^{(2)}(c);\gamma) & c_3(\mathbf{y}_o^{(2)}(c);\gamma) \\ c_1(\mathbf{y}_o^{(3)}(c);\gamma) & c_2(\mathbf{y}_o^{(3)}(c);\gamma) & c_3(\mathbf{y}_o^{(3)}(c);\gamma) \end{vmatrix}. \tag{4.41}$$

Given an initial length of the cylinder, for each choice of n, there exists a non-trivial solution of the system (4.21)-(4.23) satisfying the prescribed boundary conditions for values of γ at which the determinant vanishes. As in Chapter 3, to find such values, we use a numerical root-finding scheme, such as the interval bisection method. For a growing tube, the critical growth value corresponding to the mode n, say $\gamma^{(n)}$ is the smallest value of γ in the interval $(1, \infty)$ for which $\Delta(\gamma) = 0$. The critical growth is then given by $\gamma^c = \min_n \left(\gamma^{(n)}\right)$.

4.4 3-D Elasticity Results

We first examine the effect of the outer layer thickness on the buckling behaviour. The curves in Figure 4.2(a) show $\gamma^{(n)}$ as a function of the outer radius, C, for fixed inner radius, $B = 1$, initial length, $L_0 = 100$, and shear modulus ratio (which we shall call the stiffness ratio), μ_i/μ_o=100. For each mode the corresponding growth curve is monotonic and approaches a constant value as C increases (this is observable for $n > 5$ in Figure 4.2(a), but the limits are not shown for lower modes). This is due to the fact that increasing the thickness of the outer layer results in a greater degree of transverse reinforcement acting on the inner layer, and the displacement of the surrounding medium is confined to a small region surrounding the inner layer.

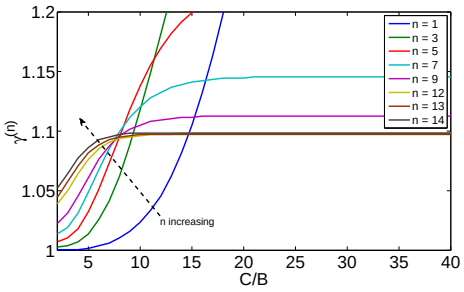

(a) $\mu_i/\mu_o = 100, B = 1, L_0 = 100$.

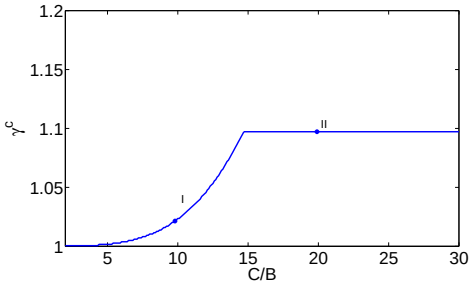

(b) $\mu_i/\mu_o = 100, B = 1, L_0 = 100$.

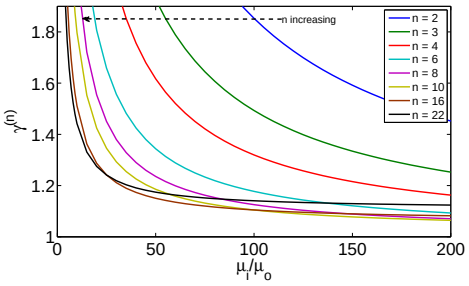

(c) $B = 1, C = 40, L_0 = 100$.

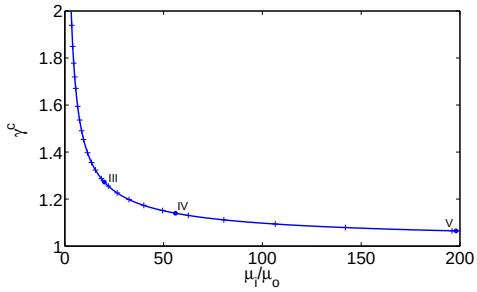

(d) $B = 1, C = 40, L_0 = 100$.

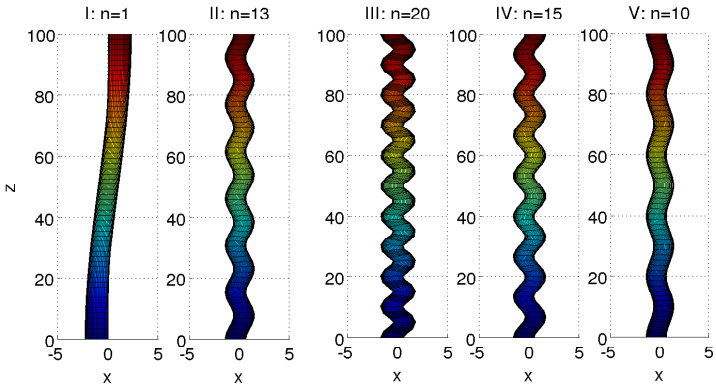

(e)

Figure 4.2: (a) Critical growth vs. relative thickness of layers for a range of modes between $n = 1$ and $n = 14$ and fixed stiffness ratio. (b) Overall critical growth vs. relative thickness of each layer. Around $k = 15$ a mode transition occurs, where the observed buckled mode switches from one with a long wavelength to one with a short wavelength. (c) Critical growth vs. stiffness ratio μ_i/μ_o for a range of modes between $n = 1$ and $n = 22$. (d) Overall critical growth vs. stiffness ratio. Crosses indicate transition points. We note the curve appears much smoother than that shown in (b) and there exist many more transition points. (e) Depictions of the buckled inner filament corresponding to each of the arbitrary points marked in (b) and (d). The amplitude of the oscillations is determined by ϵ and has no physical significance. It has been chosen to illustrate the form of the structure.

Within this region, the magnitude of the displacement decreases as r increases so that material points far from the buckled filament are less displaced than those close to the material boundary. Thus, increasing the thickness of the outer layer beyond a certain amount has no effect on the resulting value of $\gamma^{(n)}$.

For each C the critical growth γ^c is given by $\gamma^c = \min_n \left(\gamma^{(n)}\right)$, as shown in Figure 4.2(b). Visual depictions of the critical mode in each region are shown in Figure 4.2(e). For the given parameter values, we see that close to $C = 15$ a mode transition occurs, where the observed buckling mode suddenly switches from $n = 1$ to $n = 13$. A similar jump in buckling mode has been observed previously by Moulton and Goriely [67] in the case of a single layer tube subject to radial growth. We can consider the total energy of the system to be a combination of the bending energy of the inner cylinder and the elastic 'foundation' energy of the outer layer. For a one-layer tube ($C = B$), we recover the classical Euler beam problem, and expect the mode $n = 1$ to be selected. When C is close to B, the foundation energy is small compared to the bending energy, therefore longer wavelength modes are selected, when compared to the case in which C is large. As C increases, the foundation energy of the outer layer plays a more significant role and the inner layer 'prefers' to undergo a higher degree of bending. Therefore, shorter wavelength modes are selected. Thus, we can interpret the transition point as the maximum thickness of the outer tube for which larger foundation displacements are preferable to a higher degree of bending.

Next, we consider the case of a fixed geometry with varying stiffness ratio, that is, we set $\mu_o = 1$ and vary μ_i. In Figure 4.2(c) we see that for each buckling mode, the critical growth value decreases monotonically as the stiffness ratio increases. This reflects the fact that a relatively soft outer layer is easier to displace than a relatively stiff outer layer. Thus, as μ_i/μ_o increases, the amount of lateral reinforcement decreases so that less axial growth can occur before the onset of instability. We also observe that each curve approaches a constant value that is greater than or equal to

1 as $\mu_i/\mu_o \to \infty$. We can consider this limit to be identical to the scenario of the outer layer being absent altogether, which is precisely the Euler buckling problem [21]. Furthermore, the observed buckling mode is highly sensitive to variations in the stiffness ratio, particularly when $\mu_i/\mu_o < 40$. In this region, shorter wavelength buckling modes are selected as the observed buckling mode because the associated bending energy cost is low, whilst longer wavelength modes are selected as the relative stiffness and thus foundation energy of the outer layer decreases. The critical growth γ^c as a function of μ_i/μ_o is given in Figure 4.2(d). We observe much 'smoother' transitions between the observed modes as μ_i/μ_o varies, when compared to the case of varying C. Depictions of the inner cylinder are shown in Figure 4.2(e) for the indicated points in Figure 4.2(d).

Repeating our numerical procedure for different values of L_0 while maintaining B and C at fixed values, we find that the graphs of γ^c against μ_i/μ_o (not shown), are identical. This indicates that in the case of a filament embedded in a sufficiently thick outer layer, the critical growth value is independent of the initial length of the filament, as expected. Figure 4.3 shows the corresponding observed dimensionless buckling wavelength, λ, against the stiffness ratio for each value of L_0. We observe that the initial length does have some influence on the buckling wavelength, particularly when $B/L_0 = \mathcal{O}(1)$. However, this dependence arises due to our demand that n is an integer, so that the wavelength must belong to a discrete set of values. As L_0 increases we observe smaller differences between the curves, so for large L_0 we may estimate the wavelength by a best-fit to the discretised results.

In Figure 4.4, the log-log plot of the dimensionless wavelength of the observed buckling mode against the stiffness ratio μ_i/μ_o is shown for the case $L_0 = 100$. We observe that the slope is close to 1/4, which indicates that the observed buckling wavelength and stiffness ratio are related by a power law, *i.e.* $\lambda \propto (\mu_i/\mu_o)^{1/4}$. This is consistent with a basic dimensional analysis, which can already be found in the

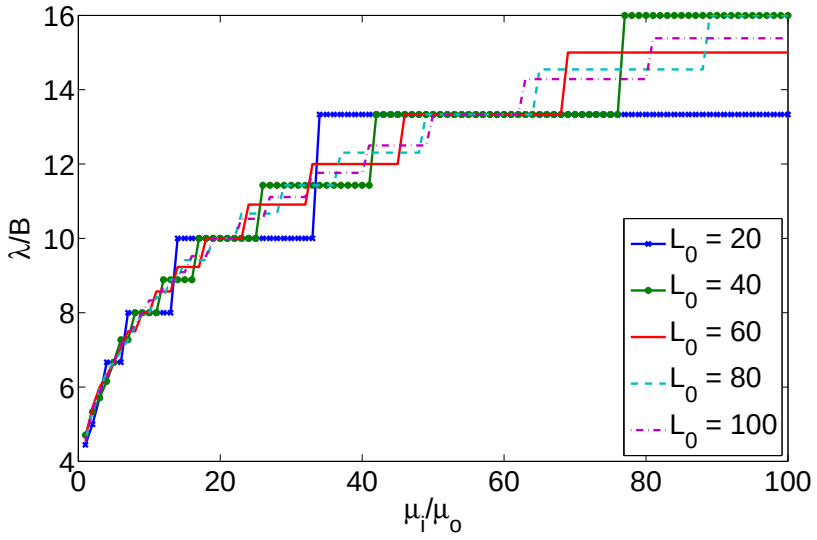

Figure 4.3: Observed buckling wavelength vs. stiffness ratio μ_i/μ_o for $B = 1, C = 40$ and a range of initial lengths.

original work of Winkler [106, 24]. We also consider the case $m = 0$ (*i.e.* barrelling modes) for the parameter values $L_0 = 10, B = 1, C = 40$ and varying μ_i/μ_o. In the region of interest ($25 < \mu_i/\mu_o < 200$), the critical growth $\min_n(\gamma^{(n)})$ is greater than that corresponding to the critical growth in the case $m = 1$. This justifies the assumption that slender filaments will always exhibit axial buckling rather than barrelling instabilities.

4.4.1 WKB Approximation

We are particularly interested in the case of a slender filament embedded in an infinite matrix, so that we can compare the results of the 3-D approach with those obtained using a rod theory approach. Therefore, we seek analytical solutions of the equilibrium equations (4.21)-(4.23) in the case $C \to \infty$ by considering the problem of a neo-Hookean cylinder embedded in an infinite neo-Hookean matrix.

By substituting the relevant expressions for $\mathcal{L}_{ijkl}$ for a neo-Hookean material into

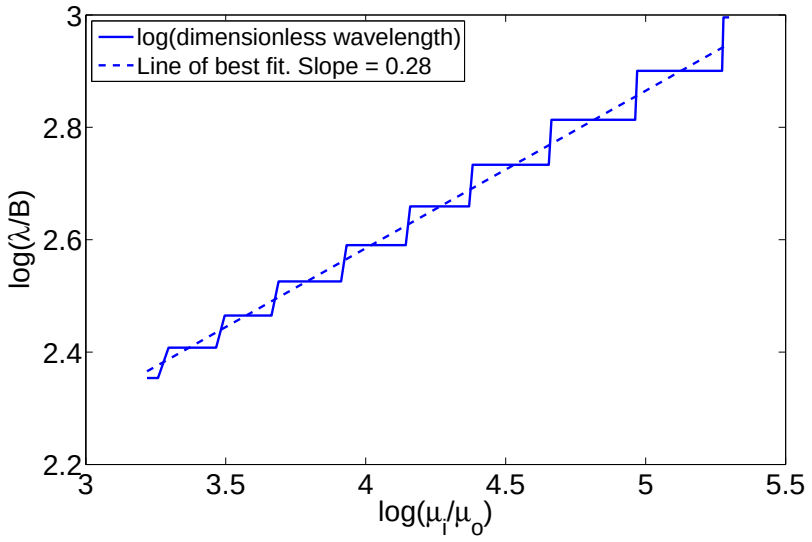

Figure 4.4: log-log plot of observed buckling wavelength vs. stiffness ratio μ_i/μ_o.

(4.21)-(4.23) we obtain the following system of equations in the inner layer:

$$0 = f'' + \frac{1}{r}f' - \left(\frac{\alpha^2}{\gamma^3} + \frac{2}{r^2}\right) f - \frac{2}{r^2}g - \frac{1}{\gamma\mu_i}k', \tag{4.42}$$

$$0 = g'' + \frac{1}{r}g' - \left(\frac{\alpha^2}{\gamma^3} + \frac{2}{r^2}\right) g - \frac{2}{r^2}f - \frac{1}{\gamma\mu_i}\frac{k}{r}, \tag{4.43}$$

$$0 = -f''' - \frac{2}{r}f'' + \left(\frac{\alpha^2}{\gamma^3} + \frac{2}{r^2}\right) f' + \frac{\alpha^2}{\gamma^3 r}f - \frac{1}{r}g'' + \frac{1}{r^2}g' + \frac{\alpha^2}{\gamma^3 r}g + \frac{\alpha^2}{\gamma\mu_i}k. \tag{4.44}$$

In the outer layer, we define $\hat{\kappa} = 1 - (1 - \gamma^{-1})b^2 r^{-2}$. The resulting system is then given by

$$0 = \hat{\kappa}f'' + \left(4 - 2\hat{\kappa} - \frac{1}{\hat{\kappa}}\right)\frac{f'}{r} - \left(\alpha^2 r^2 + \frac{2}{\hat{\kappa}}\right)\frac{f}{r^2} - \frac{2}{r^2\hat{\kappa}}g - \frac{1}{\mu_o}k', \tag{4.45}$$

$$0 = -\left(2 - \hat{\kappa} + \frac{1}{\hat{\kappa}}\right)\frac{f}{r^2} + \hat{\kappa}g'' + (2 - \hat{\kappa})\frac{g'}{r} - \left(\alpha^2 r^2 + 2 - \hat{\kappa} + \frac{1}{\hat{\kappa}}\right)\frac{g}{r^2} + \frac{k}{r\,\mu_o}, \tag{4.46}$$

$$\begin{aligned} 0 = {} & \frac{\alpha^2 k}{\mu_o} - \hat{\kappa}\frac{g''}{r} + (3\hat{\kappa} - 2)\frac{g'}{r^2} + \left(\alpha^2 r^2 + 2 - 3\hat{\kappa} + \frac{1}{\hat{\kappa}}\right)\frac{g}{r^3} - \hat{\kappa}f''' - \frac{2f''}{r} \\ & + \left(\alpha^2 r^2 - 2 + 3\hat{\kappa} + \frac{1}{\hat{\kappa}}\right)\frac{f'}{r^2} + \left(2 - 3\hat{\kappa} + \frac{1}{\hat{\kappa}} + \alpha^2 r^2\left(\hat{\kappa} - 1 + \frac{1}{\hat{\kappa}}\right)\right)\frac{f}{r^3}. \end{aligned} \tag{4.47}$$

As in the case of a finite outer radius, we require finite radial stress as $r \to 0$ and

$$f_i = f_o, \tag{4.48}$$

$$g_i = g_o, \tag{4.49}$$

$$f_i' = f_o', \tag{4.50}$$

$$2\gamma\mu_i \left(f_i' - \frac{k_i}{\mu_i} \right) = 2\mu_o \left(\hat{\kappa} f_o' - \frac{k_o}{\mu_o} \right), \tag{4.51}$$

$$\gamma\mu_i \left(-\frac{f_i}{r} + g_i' - \frac{g_i}{r} \right) = \mu_o \hat{\kappa} \left(-\frac{f_o}{r} + g_o' - \frac{g_o}{r} \right), \tag{4.52}$$

$$\begin{aligned} \gamma\mu_i \left(-f_i'' - \frac{f_i'}{r} + (1 \ - \alpha^2 r^2) \frac{f_i}{r^2} + \frac{g_i'}{r} + \frac{g_i}{r^2} \right) \\ = \mu_o \hat{\kappa} \left(-f_o'' - \frac{f_o'}{r} + \left(1 - \alpha^2 r^2\right) \frac{f_o}{r^2} + \frac{g_o'}{r} + \frac{g_o}{r^2} \right), \end{aligned} \tag{4.53}$$

at $r = b$. We replace the zero-stress condition at $r = c$ with the condition that $f_o,\ g_o,\ k_o \to 0$ as $r \to \infty$.

4.4.2 Inner Layer

Equations (4.42)-(4.44) can be solved exactly by using a method described in [11]. We proceed by introducing the potential functions $\Omega(r, \theta, z)$ and $\Psi(r, \theta, z)$ such that the displacements u, v and w are given by:

$$u = \Omega_{r,z} + \frac{\Psi_\theta}{r}, \quad v = \frac{\Omega_{\theta,z}}{r} - \Psi_r, \quad w = -\nabla^2 \Omega. \tag{4.54}$$

Furthermore, we set

$$\Omega = \omega(r) \cos\theta \sin\alpha z, \tag{4.55}$$

$$\Psi = \psi(r) \sin\theta \cos\alpha z, \tag{4.56}$$

so that substitution into (4.54) gives:

$$f_i(r) = \alpha\omega' + \frac{\psi}{r}, \quad g_i(r) = -\frac{\alpha}{r}\omega - \psi'. \tag{4.57}$$

Then, eliminating k from (4.42)-(4.44) we are able to solve the remaining equations exactly. Imposing the finite stress condition results in the following expressions for ω and ψ:

$$\omega = a_1 I_1\left(\gamma^{-\frac{3}{2}}\alpha r\right), \quad \psi = a_2 I_1\left(\gamma^{-\frac{3}{2}}\alpha r\right), \tag{4.58}$$

where $I_1(r)$ is a modified Bessel function of the first kind. Therefore we have the following expressions for f_i, g_i and k_i:

$$f_i = \frac{\alpha^2 a_1}{\gamma^{\frac{3}{2}}} I_0\left(\gamma^{-\frac{3}{2}}\alpha r\right) + \frac{a_2 - \alpha a_1}{r} I_1\left(\gamma^{-\frac{3}{2}}\alpha r\right), \tag{4.59}$$

$$g_i = -\frac{\alpha a_2}{\gamma^{\frac{3}{2}}} I_0\left(\gamma^{-\frac{3}{2}}\alpha r\right) + \frac{a_2 - \alpha a_1}{r} I_1\left(\gamma^{-\frac{3}{2}}\alpha r\right), \tag{4.60}$$

$$k_i = 0, \tag{4.61}$$

where a_1 and a_2 are constants.

4.4.3 Outer Layer

Equations (4.45)-(4.47) do not easily yield an exact analytical solution. A possible way to proceed is by exploiting a small parameter in the problem and carrying out an asymptotic expansion. In this case, there are several possible choices. Given that the cylinder is slender, we could try using the aspect ratio B/L_0. Alternatively, we know the outer layer is much thicker than the inner layer, so B/C is another scaling that could be used, but only in the case where C is finite. Furthermore, it is reasonable to expect the growth to be close to 1 in the case of a stiff, slender filament, so we could

use a further simplification whereby we expand $\gamma = 1 + \epsilon\gamma^{(1)}$, where ϵ is chosen to be one of the scalings mentioned above. In all these cases, we find that the leading order problem can be solved. However, the solution obtained is either independent of the axial mode, α, or the growth parameter, γ, whilst at the next order we are faced with a computational challenge that does not seem any easier to solve than the exact outer layer equations. In order to make progress analytically, we consider the case of a high axial wavenumber, that is $\alpha \gg 1$ so that $\delta = \alpha^{-1} \ll 1$ and obtain an approximate solution using the WKB method. Note that we cannot guarantee *a priori* that for given L_0 the value of α corresponding to the observed buckling mode will indeed be large and this issue will be discussed later. Further details can be found in [25]. We seek solutions of the form

$$\begin{Bmatrix} f_o \\ g_o \\ k_o \end{Bmatrix} = \begin{Bmatrix} F \\ G \\ \alpha K \end{Bmatrix} \exp\left(\alpha \int^r s(x)dx\right). \tag{4.62}$$

Substituting this expression into the equilibrium system leads to the following forms of $f_o,\ g_o$ and k_o at leading order:

$$f_o = \frac{a_3\sqrt{r}\,\mathrm{e}^{-\alpha r} + a_4\,\mathrm{e}^{-\alpha\sqrt{r^2-\gamma+1}}\,(r^2-\gamma+1)^{1/4}}{\sqrt{\gamma-1}}, \tag{4.63}$$

$$g_o = \frac{a_5\,\mathrm{e}^{-\alpha\sqrt{r^2-\gamma+1}}}{(r^2-\gamma+1)^{1/4}}, \tag{4.64}$$

$$k_o = \frac{\mu_o a_4\,\alpha\,\mathrm{e}^{-\alpha r}\sqrt{\gamma-1}}{r^{3/2}}, \tag{4.65}$$

where $a_j,\ j = 3, 4, 5$, are constants.

Substitution of (4.59)-(4.61) and (4.63)-(4.65) into the matching conditions (4.48)-

(4.53) results in the matrix equation

$$\mathbf{M.a} = 0, \tag{4.66}$$

where $\mathbf{a}= (a_1, a_2, a_3, a_4, a_5, \gamma)^T$ and M_{ij} is the coefficient of a_j (or γ, when $j = 6$) in each condition. For a given aspect ratio B/L_0 and stiffness ratio μ_i/μ_o we select a buckling mode of interest (*i.e.* choose a value of n) and solve the system of matching conditions to find $\gamma^{(n)}$:

$$\det\left(\mathbf{M}(\gamma^{(n)})\right) = 0. \tag{4.67}$$

Again, the critical growth is then given by $\gamma^c = \min_n\left(\gamma^{(n)}\right)$.

4.4.4 Comparison of Numerical and WKB Results

We assess the accuracy of the WKB approximation by comparing the estimated critical growth values and corresponding wavelengths obtained using this method with the numerical results. As before, we assume $m = 1$. In Figure 4.5(a) plots of γ^c as a function of μ_i/μ_o are shown for five different values of L_0, together with the corresponding plot obtained numerically. We see that the estimates lie close to the numerical curves, which indicates that our approximation provides a good estimate of the critical growth.

In Figure 4.5(b) the estimated observed buckling wavelength is plotted along with the corresponding numerical value. We see good agreement with the numerical results, even though the largest value of α is approximately given by 0.4π. Our approximation was based on the assumption that the wavenumber, α, is large, but we conclude that the approximation gives good estimates of γ^c, even when $\alpha = \mathcal{O}(1)$. The WKB method also recovers the power law relationship between wavelength and stiffness ratio obtained from the numerical results and the work of [13].

Now that we have an analytic method for estimating γ^c in terms of the directly

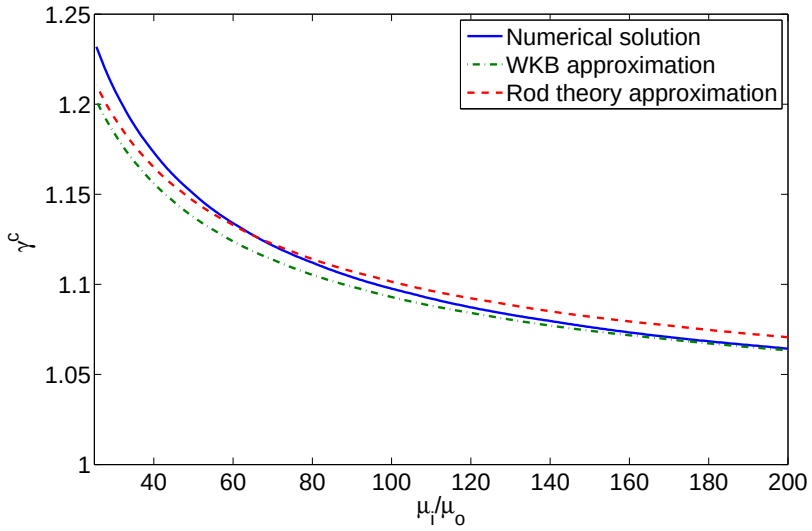

(a) Comparison of critical growth value vs. stiffness ratio curves in a fixed geometry for the two modelling approaches. The parameter values used are $E = 3\mu_i$, $\mu_o = 1$, $L_0 = 100$, $B = 1$, and $C = 40$ (the latter applies to 3-D elasticity approach only). The value of C_1 that minimises the sum of squares between the rod theory and numerical results is 2.8π.

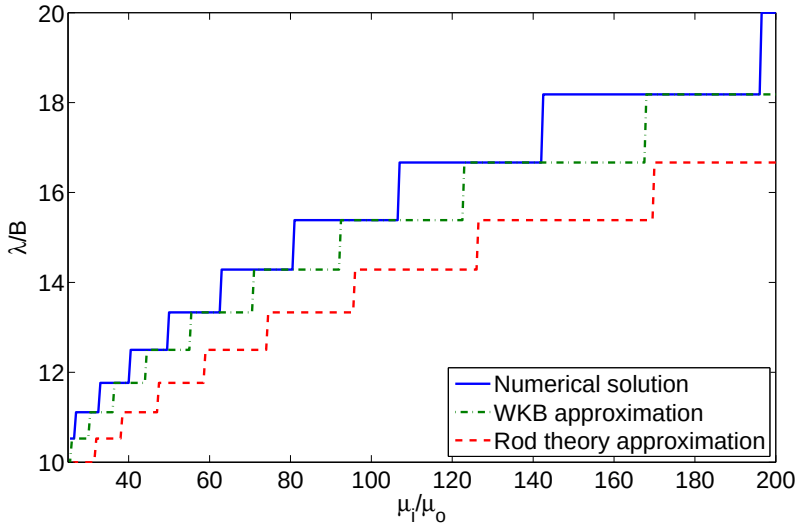

(b) Comparison of observed buckling wavelength vs. stiffness ratio in a fixed geometry for the two modelling approaches. The parameter values used are identical to those used in Figure 4.5(a) and $C_1 = 2.8\pi$.

Figure 4.5: Comparison of the approaches obtained by minimising the sum of squares of differences in critical growth between the numerical results and those obtained using rod theory.

observable properties of the system, we aim to map these properties to the foundation modulus. In the next section we focus on estimating γ^c using a rod theory approach. Our two different estimates of the critical growth then act as the link between the two frameworks and will yield a means of estimating k_f.

4.5 Elastic Rod Approach

To obtain the numerical results in Section 4.4, we assumed that in the buckled configuration, spatial oscillations within the body are confined to a single plane. The full rod analysis also shows that the first instability is planar [69]. Therefore, an alternative approach is to use a rod theory formulation, which treats the inner layer as an elastic rod embedded in an infinite medium subject to axial growth and transverse displacements. We use the general formalism of morphoelastic rods for this particular problem.

4.5.1 Setup

We consider a stress-free straight unshearable rod of length L_0 lying in the (y, z) plane. The rod's centreline lies along the z-axis, and is confined between two rigid platens a fixed distance, L_0, apart. The rod is subjected to axial growth, γ, so that in the absence of the platens, its unstressed (natural) length is $L = \gamma L_0$. However the axial constriction supplied by the platens results in the rod becoming compressed, until it buckles. Let S_0 and s denote the arc length of the rod in the initial and current configurations respectively. Additionally, let S denote arc length in the stress-free grown configuration *i.e.* the configuration the grown rod would adopt if the platens were removed and define $\beta = ds/dS$. We use κ and θ to denote the curvature of the rod and angle between the rod's centreline and the z-axis respectively. This information is summarised in Figure 4.6.

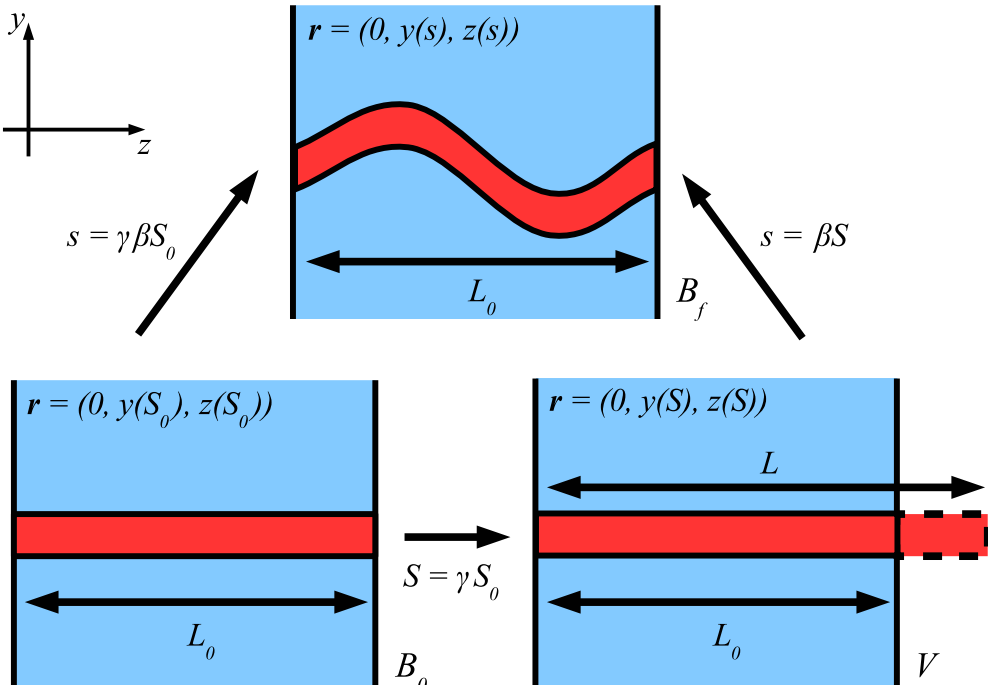

Figure 4.6: As in the 3-D case we can decompose the overall deformation into stress-free growth and elastic response steps. $\mathcal{B}_0$ is the initial, pre-growth state of the rod and $\mathcal{B}_f$ is the final, buckled state. If the absence of the platens, the rod would adopt the stress-free configuration depicted in state $\mathcal{V}$.

Assuming that the system is in static equilibrium and neglecting body couples, we have from (2.50) and (2.51)

$$\frac{\partial \mathbf{n}}{\partial S} + \mathbf{f} = 0, \tag{4.68}$$

$$\frac{\partial \mathbf{m}}{\partial S} + \frac{\partial \mathbf{r}}{\partial S} \wedge \mathbf{n} = 0, \tag{4.69}$$

where $\mathbf{m}= (m_x, 0, 0)$ is the resultant moment, $\mathbf{n}= (0, n_y, n_z)$ is the resultant force, $\mathbf{f}$ are the body forces per unit unstressed natural length. We also adopt the commonly-used assumption that the outer matrix acts as a Winkler foundation. That is, we use a linear relationship between the transverse displacement and transverse body force acting on the rod due to the surrounding matrix, so that the transverse component of traction acting on the rod is given by $-\beta k_f y$, where k_f is the foundation modulus parameter, which characterises the resistive force of the surrounding medium. Under this assumption, $\mathbf{f}$ is given by

$$\mathbf{f} = (0, -\beta k_f y, 0), \tag{4.70}$$

Finally, we close the problem by imposing the standard constitutive relations for the rod

$$m_x = E\mathcal{I}\beta\kappa = E\mathcal{I}\beta\frac{d\theta}{ds}, \tag{4.71}$$

$$n_y \sin\theta + n_z \cos\theta = E\mathcal{A}_0(\beta - 1), \tag{4.72}$$

where $E, \mathcal{I}$ and $\mathcal{A}_0$ are defined in Table 4.1. Note that since $(\beta - 1)$ measures the stretch in the rod, the last equation is simply a form of Hooke's law when uniaxial

deformations are considered. Substitution into the equilibrium equations then gives

$$\begin{cases} y' = \gamma\beta \sin\theta, \\ z' = \gamma\beta \cos\theta, \\ n_y' = \gamma\beta k_f y, \\ n_z' = 0, \\ E\mathcal{I}\theta'' + \gamma(z'n_y - y'n_z) = 0, \end{cases} \tag{4.73}$$

where primes denote differentiation with respect to S_0. The boundary conditions are given by:

$$z(0) = 0, \quad z(L_0) = L_0, \quad \theta(0) = \theta(L_0) = 0, \quad n_y(0) = n_y(L_0) = 0. \tag{4.74}$$

4.5.2 Buckling

We proceed by considering small perturbations around the straight, compressed straight rod solution. That is, we introduce perturbations of size $0 < \epsilon \ll 1$ and make the following expansions:

$$\begin{aligned} y &= y_0 + \epsilon y_1 + \dots, \\ z &= z_0 + \epsilon z_1 + \dots, \\ \theta &= \epsilon\theta_1 + \dots, \\ n_y &= n_{y0} + \epsilon n_{y1} + \dots, \\ n_z &= n_{z0} + \epsilon n_{z1} + \dots, \\ \beta &= \beta_0 + \epsilon\beta_1 + \dots. \end{aligned}$$

At leading order, we obtain the system

$$\begin{cases} y_0' = 0, \\ z_0' = \gamma\beta_0, \\ n_{y0}' = \gamma\beta_0 k_f y_0, \\ E\mathcal{I}\theta_0'' + \gamma(z_0' n_{y0} - y_0' n_z) = 0, \end{cases} \tag{4.75}$$

and the constitutive relation (4.72) yields

$$n_{z0} = E\mathcal{A}_0(\beta_0 - 1). \tag{4.76}$$

A non-trivial solution is given by

$$z_0 = S, \quad \beta_0 = \frac{1}{\gamma}, \quad y_0 = 0, \quad n_{y0} = 0. \tag{4.77}$$

This solution corresponds with the finite, pre-buckled solution derived in the 3-D elasticity problem in Section 4.2.

To examine the stability of the straight solution we consider the $\mathrm{O}(\epsilon)$ system

$$\begin{cases} y_1' = \gamma\beta_0\theta_1, \\ z_1' = \gamma\beta_1, \\ n_{y1}' = \gamma\beta_0 k_f y_1, \\ E\mathcal{I}\theta_1'' + \gamma(n_{y1} - y_1' n_{z0}) = 0, \end{cases} \tag{4.78}$$

and

$$\beta_1 = 0, \tag{4.79}$$

which follows from the constitutive relation. Substitution leads to the following

fourth-order ordinary differential equation for θ_1

$$E\mathcal{I}\theta_1'''' + \gamma(k_f\theta_1 - n_{z0}\theta_1'') = 0. \tag{4.80}$$

We seek solutions of the form $\theta_1 \sim \mathrm{e}^{n\pi i S_0/L_0}$ (real part assumed), where n is a positive integer. Substitution into (4.80) results in the following quadratic equation for n^2:

$$\frac{E\mathcal{I}\pi^4}{L_0^4}n^4 + \frac{\gamma n_{z0}\pi^2}{L_0^2}n^2 + \gamma k_f = 0. \tag{4.81}$$

Note that in the absence of the outer layer $k_f = 0$ and we recover a scenario that is similar to the classic Euler beam problem (see *e.g.* Chapter 4.9.3 of [50]). In this case we can obtain a form of (3.60), where K_{m_1} replaces $E\mathcal{I}$ and $\frac{\hat{\lambda}}{\lambda^*}$ replaces γ, by setting $n = 1$.

Substitution of (4.76) into (4.81) then yields the following expression for γ:

$$\gamma(n) = \frac{E\mathcal{I}n^4\pi^4 + L_0^2E\mathcal{A}_0n^2\pi^2}{L_0^2E\mathcal{A}_0n^2\pi^2 - L_0^4k_f} = \frac{E\mathcal{I}\alpha^4 + E\mathcal{A}_0\alpha^2}{E\mathcal{A}_0\alpha^2 - k_f} \tag{4.82}$$

We wish to find the buckling mode that minimises the critical growth. Therefore we solve $\dfrac{\mathrm{d}\gamma}{\mathrm{d}\alpha} = 0$ to find some α^c and a corresponding value of n, which will lie between two consecutive integers, say n_1 and $n_1 + 1$. The critical growth is then given by $\gamma^c = \min(\gamma(n_1), \gamma(n_2))$ and the corresponding $n_j,\ j = 1,\ 2$, is the observed buckling mode. As $L_0 \to \infty$, the critical growth value approaches the value of γ for which (4.82) has real roots. Therefore we examine when its discriminant is equal to zero:

$$E^2\mathcal{A}_0^2(\gamma - 1)^2 = 4E\mathcal{I}\gamma k_f, \tag{4.83}$$

3-D Model	Role of Parameter(s)	Rod Theory Model	Role of Parameter(s)
L_0	Initial length of cylinder	L_0	Initial length of rod
l	Deformed length of cylinder (pre-bifurcation)	l	Compressed length of rod
γ	Axial growth	γ	Axial growth
B	Radius of stress-free inner cylinder	$\mathcal{A}_0 = \pi B^2$	Cross-sectional area
		$\mathcal{I} = \pi B^4/4$	Second moment of area
μ_i	Shear modulus of inner layer	$E = 3\mu_i$	Young's modulus of rod
u, v, w	Post-bifurcation displacements	y, z, θ	Geometry of buckled rod
μ_o	Shear modulus of outer layer	k_f	Foundation modulus
z	Axial co-ordinate	S_0	Arc length of undeformed rod

Table 4.1: Relationships between the parameters used in each modelling approach.

which yields

$$\gamma^c = 1 + \frac{2\mathcal{I}k_f}{E\mathcal{A}_0^2}\left(1 + \sqrt{1 + \frac{E\mathcal{A}_0^2}{\mathcal{I}k_f}}\right), \quad \lambda = 2\pi\left(\frac{E\mathcal{I}}{\gamma k_f}\right)^{1/4}. \tag{4.84}$$

4.6 Connecting the Approaches

As discussed in the introduction to this chapter, there is no direct method to obtain the parameter k_f, despite the fact that it is widely used in many rod theory problems. We relate this parameter to measurable properties of the system by comparing the results of the rod theory approach described in the previous section with the results of the 3-D formulation. To do so, we first compare the roles of the various parameters involved in each modelling approach. A summary of the correspondence between the parameters of the two models is shown in Table 4.1. In particular, we note that the parameters μ_o and k_f are related to each other, though the exact relationship between them is unknown. We investigate whether a simple, linear relationship provides agreement with the 3-D elasticity approach. That is, we postulate

$$k_f = C_1\mu_o, \tag{4.85}$$

where C_1 is a constant. Such an ansatz is a natural first-approximation for the proposed relationship. For a rod with a circular cross-section we have $\mathcal{A}_0 = \pi B^2$ and $\mathcal{I} = \pi B^4/4$. For each choice of C_1 we solve (4.82) to find the observed buckling mode of the rod and its corresponding critical growth value, γ^c, in terms of μ_i/μ_o. We then estimate k_f by seeking the value of C_1 that minimises the sum of squares of the growth between these data and the corresponding results obtained numerically in Section 4.4.

Figure 4.5 shows the critical growth and wavelength plots obtained using the WKB approximation and rod theory approach, together with the corresponding numerical results obtained in Section 4.4 for ease of comparison. The fitting of the results from the rod theory approach with the corresponding results from the 3-D approach was repeated for different values of L_0 to determine whether C_1 is, in fact, dependent upon the geometry of the rod (though only the plots corresponding to the case $L_0 = 100$ are shown, because other values of L_0 give rise to almost identical results). The region of fitting used was $25 < \mu_i/\mu_o < 200$. We restrict attention to this region because stiffness ratios lower than $\mu_i/\mu_o = 200$ are most common throughout nature, and when $\mu_i/\mu_o < 25$ the axial strain is greater than 20%. In the case of low ($L_0 \approx 10$), there is some variation of C_1 with L_0. However, this is precisely the regime in which we expect the assumptions of rod theory to break down, since $B/L_0 = \mathcal{O}(1)$. As L_0 increases, C_1 becomes geometry-independent and is approximately equal to 2.8π. Figure 4.5(a) shows good agreement in the critical growth curves in the region $25 < \mu_i/\mu_o < 200$ for this choice of constant, with the maximum relative difference between the two curves being approximately 0.02, when $\mu_i/\mu_o = 25$. When the observed buckling wavelength is considered, as shown in Figure 4.5(b), the rod theory approach tends to slightly underestimate the observed wavelength, compared to the numerical results.

Alternatively, we could fit the the observed buckling wavelength instead of the critical growth. This may be preferable, since the wavelength is a directly-observable

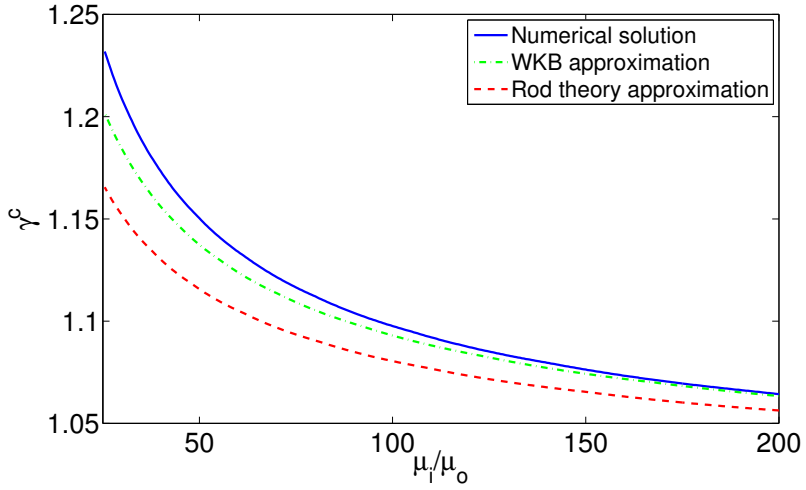

(a) Comparison of critical growth value vs. stiffness ratio curves in a fixed geometry for the two modelling approaches. The parameter values used are $E = 3\mu_i$, $\mu_o = 1$, $L_0 = 100$, $B = 1$, and $C = 40$ (the latter applies to 3-D elasticity approach only). The value of C_1 that minimises the sum of squares between the rod theory and numerical results is 1.8π.

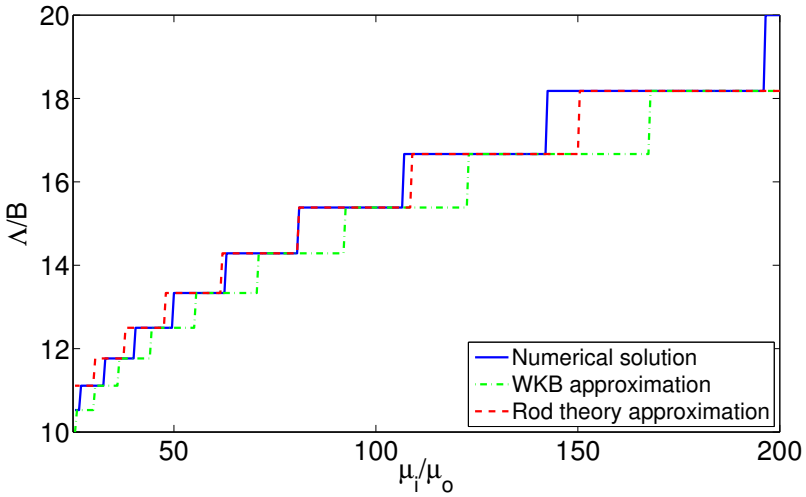

(b) Comparison of observed buckling wavelength vs. stiffness ratio in a fixed geometry for the two modelling approaches. The parameter values used are identical to those used in Figure 4.7(a) and $C_1 = 1.8\pi$.

Figure 4.7: Comparison of the approaches obtained by minimising the sum of squares of differences in observed buckling wavelength between the numerical results and those obtained using rod theory.

property of the system. As in the previous case, we fit the two curves in the region $25 < \mu_i/\mu_o < 200$ and the results are shown in Figure 4.7. Here, the optimal value of C_1 is approximately equal to 1.8π. As expected, the agreement between the numerical results and rod theory results is good when the wavelengths are compared, but the rod theory approach tends to slightly underestimate the value of the critical growth.

There are two possibles causes for the slight difference between the two results. First, we note that there exists a potentially significant difference between the two modelling approaches. In the 3-D elasticity formulation, we adopted the assumption of incompressibility. Therefore, as the inner cylinder grows subject to the axial constraint, its cross-sectional area must increase to preserve the overall volume of the grown structure. In the elastic rod model, we can account for this cross-sectional change in the case of bending energy by modifying $\mathcal{A}_0$ and $\mathcal{I}$ accordingly. However, a key assumption of our approach is that the transverse force n_y acts on the rod's centreline. Therefore, as long as the rod remains straight it experiences the axially compressive force only. This simplification thus affects the energy required by the rod to displace the surrounding matrix. Second, in Figure 4.2(c) we note that the critical growth values for the various axial buckling modes are very close. This suggests that small differences in the critical growth value could result in significant qualitative differences in the state of the rod post-bifurcation, as is the case with our two modelling approaches. Nevertheless, the agreement between the two approaches is generally good, and it is interesting that a single value of C_1 is sufficient to characterise the relationship between the shear modulus of the elastic matrix and the transverse pressure it applies to the growing filament inside. We also compare our estimate of k_f with those given in (4.1) and (4.2). The parameter l is taken to be 10 (since Figure 4.3 shows the observed dimensionless buckling wavelength to be of the order 10). This yields a values $k_{e1} = 5.2\pi$ which is about twice too large. If we set $C_1 = k_{e1}$ and substitute into (4.82), this leads to significant underestimation of the critical growth

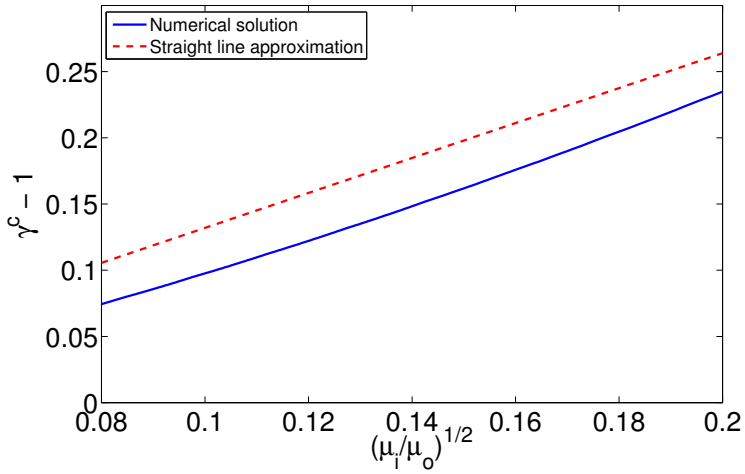

Figure 4.8: An estimate of C_1 can be derived by considering the gradient when $\gamma^c - 1$ is plotted as a function of $(\mu_o/\mu_i)^{1/2}$. To obtain the dashed line we first estimate the gradient of the solid curve. From (4.84) we estimate the gradient in the region of interest to be 1.32, which means $C_1 = 5.2\pi$. The parameter values used are the same as those in Figures 4.5 and 4.7.

value, when compared with the numerical results of the 3-D approach. The estimate k_{e2} is also unreliable because it is dependent upon the length of the filament and as the length of the filament increases, $k_f \to 0$ leading to the unphysical behaviour that an infinite filament in an elastic matrix would be equivalent to a beam without matrix.

Another means of deriving an estimate of the foundation modulus parameter from the numerical results arises from (4.84). By expanding the expression for γ^c in terms of the small parameter $\frac{k_f}{E}$, we obtain the following

$$\gamma^c - 1 = 2\left(\frac{\mathcal{I}k_f}{E\mathcal{A}_0^2}\right)^{\frac{1}{2}} + \mathcal{O}\left(\frac{k_f}{E}\right) \tag{4.86}$$

$$= 2\left(\frac{\mathcal{I}C_1}{3\mathcal{A}_0^2}\right)^{\frac{1}{2}}\left(\frac{\mu_o}{\mu_i}\right)^{\frac{1}{2}} + \mathcal{O}\left(\frac{\mu_o}{\mu_i}\right). \tag{4.87}$$

So, by plotting $\gamma^c - 1$ as a function of $(\frac{\mu_o}{\mu_i})^{\frac{1}{2}}$ we ought to expect a straight line. In Figure 4.8, we see that the numerical results do indeed exhibit this behaviour, and

that the gradient of the line is approximately 1.32 in the region $25 < \mu_i/\mu_o < 200$. For a solid filament, with radius $B = 1$, this corresponds to $C_1 \approx 5.2\pi$. However, this tangential approximation to the numerical curve does not intercept the origin. If this estimate of C_1 is substituted into the right hand side of (4.87) and plotted, we obtain the red dashed line in Figure 4.8. There is a consistent overestimation of the critical growth in the region $25 < \mu_i/\mu_o < 200$. This result suggests an approximation of the form $(\gamma^c - 1) \propto \left(\frac{\mu_o}{\mu_i}\right)^{1/2}$ is appropriate only when μ_i/μ_o is very large, and a least-squares fit of the data seems to be a more useful approach in our region of interest.

So far, our estimates of k_f have been obtained by comparing the numerical data with the results of the rod theory problem. However by combining the results of the rod theory approach and asymptotic approximation obtained in Section 4.4.1 we are able to derive a relationship between the shear modulus of the elastic matrix and the resulting transverse force acting on the embedded rod. By equating the relevant solution of (4.67) with the right hand side of (4.84(a)), an estimate of C_1 in terms of μ_i/μ_o is given by

$$C_1 = 3\pi \frac{(1-\gamma^c)^2}{\gamma^c} \frac{\mu_i}{\mu_o}, \tag{4.88}$$

where γ^c satisfies (4.67). As an example, we consider the case $\mu_i = 200$. The corresponding critical growth obtained using the WKB method is given by $\gamma^c \approx 1.06$ and substitution into (4.88) yields the estimate $C_1 \approx 2.3\pi$, which lies in the middle of the range of the two estimates obtained via the data-fitting process.

4.7 Discussion

Within the framework of 3-D elasticity, we have presented a model to predict the critical axial growth of a two-layer cylinder constrained between two rigid platens. This has allowed us to study the buckling of slender filaments embedded in a thick

elastic matrix. By taking the limit of an infinitely thick outer layer we obtained an exact solution to the inner layer equations and an analytic approximation to the outer layer equations via the WKB method. We have demonstrated that this is comparable with the finite-thickness case, since for all n, $\gamma^{(n)}$ approaches a constant value as $C \to \infty$ for fixed B. We have also compared this model with an approach making use of elastic rod theory, under the assumptions that the rod lies within an infinite Winkler foundation and that the shear modulus of the foundation, μ_o, is directly proportional to the transverse pressure, k_f.

An advantage of using the 3-D elasticity formulation is that it can easily be adapted for a wide range of strain-energy densities. We now briefly consider the case of the outer layer comprising a Mooney-Rivlin material, to determine whether the value of C_1 is affected by a second material parameter. The strain-energy density in the outer layer is now given by:

$$W_o = \frac{\mu_{1o}}{2}\left(\alpha_1^2 + \alpha_2^2 + \alpha_3^2\right) + \frac{\mu_{2o}}{2}\left(\alpha_1^2\alpha_2^2 + \alpha_2^2\alpha_3^2 + \alpha_3^2\alpha_1^2\right). \tag{4.89}$$

The shear modulus is then defined to be $\mu_o = \mu_{1o} + \mu_{2o}$. In the case $\mu_{2o} = 0$ we recover the neo-Hookean model. To investigate the role of each parameter in this model, the numerical scheme described in Section 4.4 was repeated for the case $B = 1,\ C = 40,\ L_0 = 100$ and various choices of μ_{1o} and μ_{2o} such that $\mu_o = 1$. The resulting critical growth and wavelength curves were almost identical to the curves obtained in the neo-Hookean case, though they exhibited slight variation for lower values of μ_i/μ_o (*i.e.* $\mu_i/\mu_o < 40$). We therefore conclude that for a fixed geometry, the estimate for k_f is well captured by the tangent shear modulus around the unstressed state and that no significant changes are observed in third-order elasticity (which for an incompressible material is equivalent to Mooney-Rivlin). Therefore, we do not expect the foundation modulus to depend on the non-linear properties of the strain-energy density function close to the bifurcation.

A drawback of the 3-D approach is that it requires numerical methods to solve the resulting equilibrium equations, even in the case of a simple strain-energy density. Moreover, the method of determinants can become unreliable for large or small values of γ due to the exponential growth of one or more of the $\mathbf{y}^{(i)}$ in (4.37). One way of overcoming this limitation is to use an alternative numerical scheme, such as the compound matrix method [25], though this is still computationally intensive. We are also able to make use of the WKB approximation, which allows investigation of a wider range of parameter space. This is particularly useful should we wish to investigate deformations that give rise to a combination of axial and circumferential buckling modes, such as those observed in solid tumour capillaries [61].

The elastic rod theory approach is comparatively quick to implement and is widely used throughout existing literature. Moreover, this approach allows the deformation of the filament to be tracked for different loads and beyond the point at which buckling occurs. The main drawback of rod theory is that the constant k_f is difficult to determine, whilst the 3-D approach only requires knowledge of the elastic properties of the two layers.

Both modelling approaches recover the power law relationship between the stiffness ratio and buckling wavelength, first derived by Winkler. They also show that as the relative stiffness of the outer layer increases, the critical axial growth decreases monotonically and the wavelength of the buckled configuration increases. Moreover, the critical growth is independent of the initial length of the filament. We have also shown that the two approaches can be used to provide an estimate of the foundation modulus parameter, k_f. The WKB method allows us to estimate γ^c in terms of μ_i and μ_o, and (4.88) can then be used to provide an estimate of C_1 that shows good agreement with the corresponding values obtained by fitting the results of the two approaches. Therefore we suggest the following estimate for the foundation modulus

parameter of a Winkler elastic foundation of shear modulus μ_o to be

$$k_f = 2.3\pi\mu_o, \tag{4.90}$$

independent of the length or radius of the filament. This lies in the middle of the range $[1.8\pi\mu_o, 2.8\pi\mu_o]$ which is bounded below and above by the estimates of k_f obtained by fitting the wavelength and growth curves respectively.

4.8 Conclusion

In this chapter, we have continued the theme of bridging the gap between the full 3-D theory of non-linear elasticity and rod theory begun in the previous chapter. In this case, our goal was to estimate the foundation modulus parameter characterising the transverse reinforcement of the outer elastic matrix on the inner filament. Our approach gives two estimates: one obtained by comparing the rod theory approach with the analytic approximation to the full 3-D buckling problem, and the other by curve-fitting between the rod theory and numerical results. Unlike previous estimates of the foundation modulus parameter, our estimates do not require knowledge *a priori* of the characteristic buckling wavelength of the filament, which is advantageous because it allows prediction of the critical growth and observed post-buckled wavelength, knowing only the material and geometric properties of the system.

In the next chapter, we continue to look at multi-layered cylinders, through the study of the chameleon's tongue. However our focus moves away from problems involving growth; instead we investigate the role played by anisotropy, multiple layers and residual stress in aiding the function of the tongue. To do so, we use the now-familiar theory of non-linear elasticity, because it is ideally-suited to modelling this problem: the geometric description is relatively simple, whilst the mechanical response of the tissue is more complex than the problems we have studied thus far.

Chapter 5

The Elastic Projection of the Chameleon's Tongue

Up to now, we have examined problems involving several different features of soft biological tissue introduced in Chapter 1, particularly, growth, incompressibility and multiple layers. In this chapter we consider a biologically-motivated problem involving the remaining two features mentioned in Chapter 1: anisotropy and muscle contraction. This problem can be well-described using the theory of non-linear elasticity, but before giving details, we introduce the biological question of interest.

5.1 Introduction

The chameleon is a reptile in possession of several interesting anatomical features. These include a prehensile tail, zygodactylous feet, eyes that are able to move independently of one another and, for some species, the ability to change its skin colour to match its surroundings. From a mechanical point of view, a particularly interesting anatomical feature is the chameleon's tongue, which is able to undergo ballistic flight in order to catch prey. Both the speed and range of projection are truly remarkable: depending upon the species, the tongue can extend up to twice the chameleon's

own body length in approximately 5-10ms, which is equivalent to an acceleration of roughly 500ms^{-2}.

The question is, how are such high accelerations achieved? Researchers first began investigating the anatomy of the chameleon's tongue in the nineteenth century in an attempt to provide an answer. Early theories of projection proposed a build-up of blood or air pressure in the soft tissues of the tongue [49, 14], though these were soon discredited. In 1930, Gnanamuthu reviewed these theories and proposed that muscular activity is entirely responsible for the rapid acceleration [32]. More recent work has led to the now widely-accepted hypothesis that tongue projection is the result of a catapult-like mechanism. That is, elastic energy is built up in the soft tissues of the tongue, whilst muscular activity initiates the process of converting this stored energy into kinetic energy [105, 98]. Experimental findings support this idea; it has been observed that muscle fibres within the tongue are electrically active up to 200ms prior to the onset of projection, whilst projection itself lasts only around 20ms [7, 18]. This hypothesis takes into account the role of each component of the tongue which we now briefly describe.

5.1.1 Anatomy

The entoglossal process (also known as the entoglossus) forms the rigid core of the tongue. It consists of a slender cylinder of cartilage surrounded by layers of longitudinal fibres, known as the perichondrium [49, 18]. The anterior end of the entoglossal process and perichondrium is slightly thickened and rounded [43, 18] (see Figure 5.1). Depending on the species of chameleon, the length of the entoglossal process can vary greatly, with reported measurements ranging from 15mm to 34mm [14, 109]. Wainwright and Bennett report a mean radius of the process of 0.64mm [105], though photographs taken by de Groot and van Leeuwen yield a radius of 0.85mm [18].

Surrounding the anterior portion of the entoglossal process and its connective

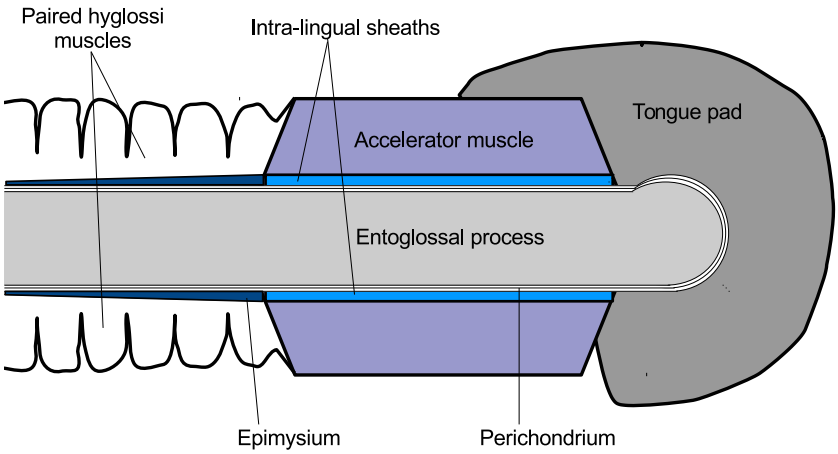

Figure 5.1: Representation of the anatomy of the chameleon's tongue, based upon photographs in [18]. The entoglossal process is surrounded by connective tissue (perichondrium) and is rounded at the anterior end. The intra-lingual sheaths consist of thin, concentric, elastic layers. The accelerator muscle is a thick sleeve of tissue surrounding the sheaths. Also depicted are the sticky tongue pad and hyglossi muscles, which are used to retract the tongue following projection.

tissue are 10-20 thin, tubular layers of elastic tissue known as the intra-lingual sheaths [18]. These sheaths are arranged in concentric layers, with the outer sheaths connected to one another via collagen attachments. The sheaths are able to slide relative to one another in a telescoping fashion [44]. Each sheath consists of families of collagenous fibres in helical arrangements, but they do not contain any elastin [18]. The pitch of the helices (defined as the angle between a fibre and the longitudinal axis of the tongue) varies along the length of the sheath, ranging from 84° at the posterior end to 40° at the anterior end [18].

Surrounding the intra-lingual sheaths is the accelerator muscle. This is a thick sleeve of tissue reinforced by fibres arranged in transverse planes. These fibres spiral outwards from the inner fascia of the muscle (that is the surface in direct contact with the intra-lingual sheaths) to the outer edge and are able to contract when electrically activated. The anterior portion of the accelerator muscle does not form a completely closed ring around the intra-lingual sheaths [49, 14, 44]. Wainwright and Bennett, among others, investigated the relationship between shape change in the accelerator muscle during electrical activation and the degree of sliding over the entoglossal process experienced by the soft tissue components [105]. Tongue projection is only possible when the muscle applies pressure to the anterior portion of the entoglossal process. This fact was determined by Meyers and Nishikawa, who severed the motor neuron of the accelerator muscle of a specimen and observed that projection was no longer possible [63]. However, de Groot and van Leeuwen concluded that muscle activity alone is not sufficient to provide the required power output. This required output was estimated using high-speed video evidence and histological measurements of a specimen [18].

Other components of the tongue include the hyglossus complex (also known as the retractor complex), which consists of a pair of muscles used to draw the tongue back into the mouth following projection [49, 32, 109], and the sticky tongue pad,

which adheres to the prey and allows the chameleon to draw the prey into its mouth during retraction.

These morphological and experimental observations suggest that the process of chameleon prey capture is as follows. Firstly, once prey is sighted, nerve impulses are received by the accelerator muscle, causing its fibres to contract. When fibre contraction occurs, the radial thickness of the muscle and intra-lingual sheaths reduces. Since soft tissue is almost incompressible, radial thinning is accompanied by axial elongation. During elongation, the fibres in the intra-lingual sheaths reorient and store elastic energy. Once the anterior portion of the accelerator muscle and sheath bundle reaches the end of the entoglossal process, the rounded end exerts a normal reaction on the inner fascia of the sheath bundle (see Figure 5.2). This reaction causes the sheaths to slide off the entoglossal process and convert elastic energy into kinetic energy. The sheaths continue to slide across one another in a telescoping fashion until the tongue reaches its maximum extension and the prey adheres to the sticky tongue pad. The hyglossus complex activates following projection and draws the accelerator muscle, sheaths and tongue pad back into the chameleon's mouth, thereby resetting the system [104].

In this chapter, we develop the first biomechanical model of the chameleon's tongue, using the sophisticated tools of finite elasticity. The model incorporates the anisotropic material response of the accelerator muscle and intra-lingual sheaths and is used to perform a detailed analysis of the energy stored in the system immediately prior to, and after projection. We verify first the hypothesis that muscle contraction alone cannot account for the high power (up to 3000Wkg^{-1}) accelerations observed experimentally [18]. We then consider the hypothesis that storing energy in the intra-lingual sheaths can account for the accelerations seen in practice. As we shall see, the stress-free configuration of the sheaths plays a crucial role in determining whether rapid projection is possible. For a realistic set of material and geometric

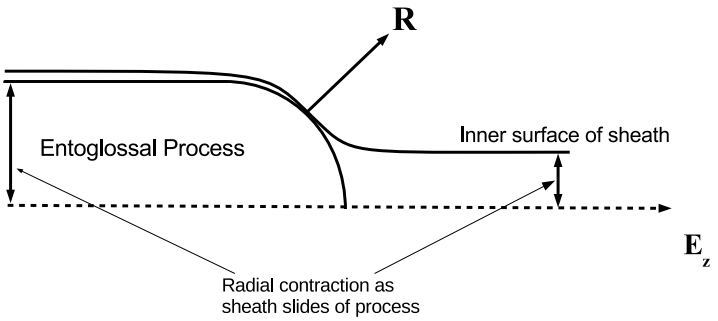

Figure 5.2: As the intra-lingual sheaths slide towards the anterior end of the entoglossal process, they contract radially. The rounded tip of the process then exerts a normal reaction on the sheaths, causing them to accelerate longitudinally.

parameters, we will determine which reference geometries yield sufficient energy for rapid projection.

5.2 Problem Setup

Tongue projection is assumed to consist of three main stages. Before prey capture begins, the fibres in the accelerator muscle are relaxed and the muscle and intra-lingual sheaths are at rest on the entoglossal process. We refer to this state as the relaxed configuration (I in Figure 5.3). When the muscle fibres are activated, axial elongation occurs until the anterior end of the muscle and sheath bundle reaches the tapering end of the entoglossal process. At this point any further contraction will initiate the conversion of stored elastic energy to kinetic energy, therefore we refer to this state as the armed configuration (II in Figure 5.3). We refer to the transition from the relaxed configuration to the armed configuration as the protrusion phase. Once the muscle and sheaths begin to slide past this point, the anterior end of the

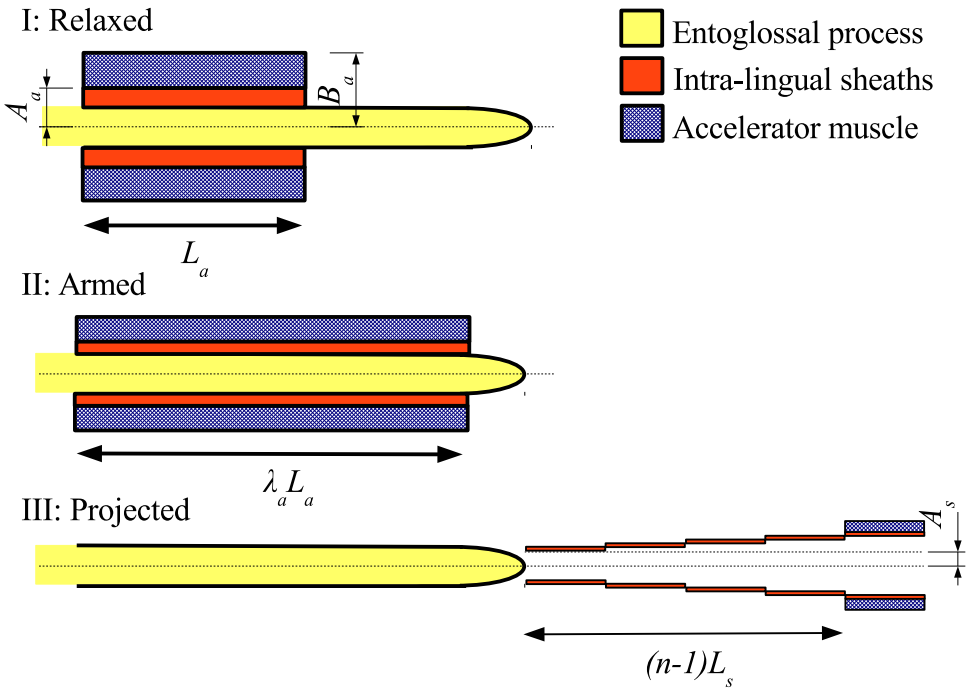

Figure 5.3: The three stages of chameleon tongue projection, according to [18]. In the relaxed configuration (I), the accelerator muscle is stress-free. Muscle fibres are relaxed and the soft tissue remains stationary on the bone. In the armed configuration (II) the muscle fibres are contracted so that the anterior end of the muscle and sheaths reaches the tapering portion of the entoglossal process. In the projected configuration (III) the tongue is no longer constrained radially by the entoglossal process. We use A_a, B_a, L_a and λ_a to denote the stress-free inner radius, outer radius, length and axial stretch, respectively, of the accelerator muscle, whilst A_s and L_s denote the stress-free inner radius and length, respectively, of the sheath bundle. Finally, n represents the number of nested sheaths. Note that B_s is not shown because the outermost sheath is not stress-free in the projected configuration.

entoglossal process exerts a normal reaction, whose axial component is non-zero, on them. This transition marks the onset of rapid acceleration. Note that it is not clear from existing literature whether the muscle slides off the entoglossal process first, followed by the sheaths, or if the muscle and sheaths slide off together. Projection continues until the tongue is fully-extended. We refer to the state of the tongue in which the muscle is contracted to the same degree as in the armed configuration, but the sheaths are no longer constrained by the entoglossal process, as the projected configuration (III in Figure 5.3).

The difference in elastic energy between the armed and projected configurations provides a measure of the kinetic energy spent during projection. Our primary focus is determining how this difference in elastic energy depends upon the material properties, geometry and structural arrangement of the tongue components. In particular, it is not clear from existing evidence whether the intra-lingual sheaths are stress-free in the relaxed configuration. Therefore we shall compare the case in which they are stress-free in the relaxed configuration with several other possible reference geometries.

We take de Groot and van Leeuwen's estimate of 72mJ to be the energy stored in the soft tissues of the tongue that is required for fast projection [18]. Muscular activity builds elastic energy in the system, but this increase is limited by the maximum power output of the accelerator muscle. According to Lutz and Rome (1994) [60], one of the highest estimates of vertebrate muscle power output is 371Wkg^{-1}. For a protrusion phase of 20ms and muscle mass of 2g we obtain an estimate of 15mJ as the maximum amount of elastic energy that can be stored in the accelerator muscle.

5.3 Mechanical Model

We model both the accelerator muscle and intra-lingual sheaths as incompressible, homogeneous, hyperelastic, fibre-reinforced cylinders. We assume each sheath has the same length and stress-free thickness, and that there are no gaps between neighbouring sheaths, so that the outer radius of any sheath is equal to the inner radius of its surrounding sheath. The sliding of neighbouring sheaths is taken to be frictionless and such that it does not induce any strain. Thus, during the protrusion phase we treat the entire sheath bundle as one continuous body (see Figure 5.4). Throughout this chapter we use the subscripts a and s to distinguish between the accelerator muscle and intra-lingual sheaths. The variables A_a, B_a and L_a, *etc.* refer

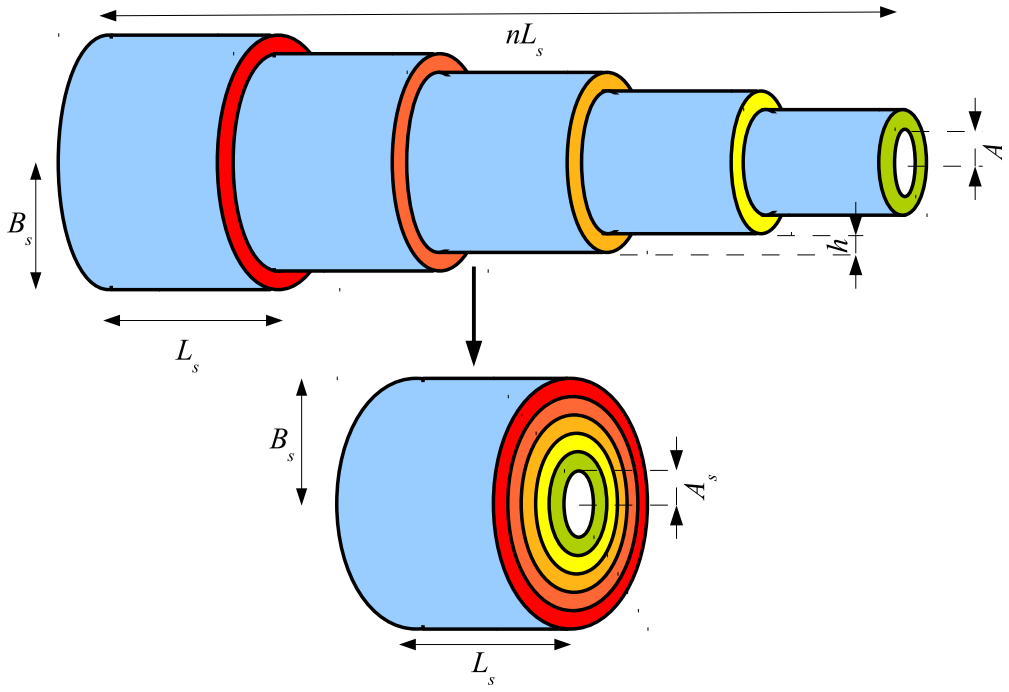

Figure 5.4: Illustration of the telescopic nature of the sheaths. The upper portion shows the arrangement of the tubular sheaths in their stress-free configuration. We assume each sheath has identical thickness, h, and length, L_s, so that no elastic energy is stored in the sheaths when they slide across each other into the lower configuration.

to the stress-free inner radius, outer radius and length, respectively, of the accelerator muscle, whilst A_s, B_s and L_s, *etc.* refer to the stress-free inner radius, outer radius and length, respectively, of the sheath bundle. As in Chapters 3 and 4, we consider axisymmetric deformations of a hyperelastic cylinder and use this geometry to model both the accelerator muscle and intra-lingual sheaths. Following the approach described in Chapter 2, and using the subscripts a and s to distinguish between the accelerator muscle and sheaths respectively, we can represent points in the reference configurations of the muscle and sheaths as

$$\mathbf{X}_{a,s} = R_{a,s}\mathbf{E}_R + Z_{a,s}\mathbf{E}_Z. \tag{5.1}$$

Similarly, the image of these points in the deformed configurations are given by

$$\mathbf{x}_{a,s} = r_{a,s}(R_{a,s})\mathbf{E}_R + \lambda_{a,s} Z_{a,s}\mathbf{E}_Z. \tag{5.2}$$

Unlike the previous chapter, we do not assume that the muscle and sheaths have the same stress-free length, nor do we assume that the outer radius of the sheaths is equal to the inner radius of the muscle. Since we do not consider twisting of the cylinders, and we do not constrain the ends, the deformation gradient is given by

$$\mathbf{F}_{a,s} = \mathrm{Grad}(\mathbf{x}_{a,s}) = \mathrm{diag}\left(\frac{dr_{a,s}}{dR_{a,s}}, \frac{r_{a,s}}{R_{a,s}}, \lambda_{a,s}\right). \tag{5.3}$$

Applying the constraint of incompressibility to each body, we obtain

$$r_{a,s}(R_{a,s}) = \sqrt{a_{a,s}^2 + \frac{R_{a,s}^2 - A_{a,s}^2}{\lambda_{a,s}}}, \tag{5.4}$$

where $a_{a,s} = r(A_{a,s})$.

The presence of spiral families of fibres in the accelerator muscle and helical arrangements of collagen fibres in the sheaths endows them with an anisotropic material response. Thus, we should consider strain-energy densities for the muscle and sheaths of the form (2.28), with the modification that I_3 is set equal to 1. For simplicity, we shall assume W depends upon I_1, I_4 and I_6 only. In this case, the expression for the Cauchy stress tensor in (2.29) simplifies to the following

$$\mathbf{T}_{a,s} = -p\mathbf{I} + 2\left[W_{a,s_1}\mathbf{B}_{a,s} + W_{a,s_4}\mathbf{F}_{a,s}\mathbf{M}_{a,s} \otimes \mathbf{F}_{a,s}\mathbf{M}_{a,s} + W_{a,s_6}\mathbf{F}_{a,s}\mathbf{M}'_{a,s} \otimes \mathbf{F}_{a,s}\mathbf{M}'_{a,s}\right]. \tag{5.5}$$

We prescribe the fibre orientations in the muscle and sheaths based upon histological observations, and these are depicted Figure 5.5. In the accelerator muscle the fibres are arranged in spirals in the cross-sectional planes, therefore we take $\mathbf{M}_a$ and $\mathbf{M}'_a$ to

be the following

$$\mathbf{M}_a = (\cos\alpha_a, \sin\alpha_a, 0)^T, \quad \mathbf{M}'_a = (\cos\alpha_a, -\sin\alpha_a, 0)^T, \tag{5.6}$$

where α_a is the (constant) angle between the fibre and the radial vector, $\mathbf{E}_R$. In the intra-lingual sheaths, the collagen fibres are arranged helically. The fibre angle, α_s varies between 84° and 40° along the length of the sheath bundle [18]. For simplicity we assume the fibre angle is constant along the length of the sheath bundle and we choose $\alpha_s = 50°$. This value lies in the observed range but is closer to the pitch in the region of the sheaths that is enveloped by the accelerator muscle than that towards the posterior end of the sheaths. Then $\mathbf{M}_s$ and $\mathbf{M}'_s$ are given by

$$\mathbf{M}_s = (0, \sin\alpha_s, \cos\alpha_s)^T, \quad \mathbf{M}'_s = (0, -\sin\alpha_s, \cos\alpha_s)^T. \tag{5.7}$$

Because the arrangement of fibres in the muscle and sheaths is symmetric, it follows that $W_4 = W_6$ and the Cauchy stress tensor has the form

$$\mathbf{T}_{a,s} = \mathrm{diag}(T_{a,s_{rr}}, T_{a,s_{\theta\theta}}, T_{a,s_{zz}}). \tag{5.8}$$

Before prescribing the material response, we consider the mechanics of the system. An important assumption we make is that during the protrusion phase, the muscle contraction occurs at a sufficiently slow rate that the tongue is in static equilibrium in the relaxed and armed configurations. We also assume that the projected phase is static, *i.e.* in the absence of body forces it would be the final resting position of the sheaths and muscle if the retractor complex were to fail to activate. Therefore, in each configuration, we have the equations of static equilibrium

$$\mathrm{div}\ \mathbf{T}_{a,s} = \mathbf{0}. \tag{5.9}$$

Since $\mathbf{T}$ is diagonal, the only non-trivial equations arising from (5.9) are

$$\frac{dT_{a,s_{rr}}}{dr_{a,s}} = \frac{T_{a,s_{\theta\theta}} - T_{a,s_{rr}}}{r}. \tag{5.10}$$

We model both the accelerator muscle and intra-lingual sheaths as reinforced neo-Hookean cylinders. The fibres in the sheaths are passive, whilst those in the muscle are active and able to contract and generate active stress. We will use the parameter ν to represent the ratio of the contracted length of the muscle fibres to their inactive length, *i.e.* it measures the degree of muscle contraction. Then the strain energy densities of the muscle and sheaths are given by

$$W_a\left(I_1, I_4, I_6\right) = \frac{\mu_{1a}}{2}\left(I_1 - 3\right) + \frac{\mu_{4a}}{2}\left[\left(I_4 - \nu\right) + \left(I_6 - \nu\right)\right], \tag{5.11}$$

and

$$W_s\left(I_1, I_4, I_6\right) = \frac{\mu_{1s}}{2}\left(I_1 - 3\right) + \frac{\mu_{4s}}{2}\left[\left(I_4 - 1\right)H(I_4 - 1) + \left(I_6 - 1\right)H(I_6 - 1)\right]. \tag{5.12}$$

The intra-lingual sheaths are unable to generate active stress, therefore there is no equivalent parameter in (5.12). We include Heaviside functions in the anisotropic term in (5.12) because we assume the helical fibres are active only in tension; when compressed they make no contribution to the elastic energy of the system. Our expressions for strain-energy and fibre angle in the muscle and sheaths can be substituted into (5.5) to obtain the components of the Cauchy stress. These components can then be substituted into (5.10) to obtain two equations of equilibrium in terms of an unknown axial stretch and inner radius, which are determined by the boundary conditions.

Since we are interested in three different configurations of the tongue, we consider three different sets of boundary conditions, each relating to one of these configu-

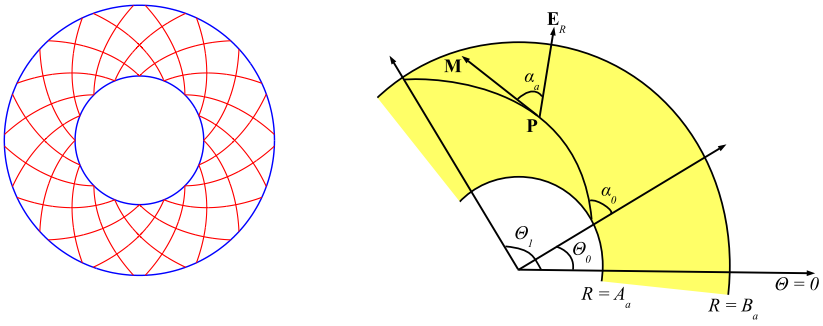

(a) Left: Cross-section of accelerator muscle. Right: Close-up of single fibre showing tangent $\mathbf{M}$ at a point $\mathbf{P}$. The other fibre passing through $\mathbf{P}$ is denoted $\mathbf{M}'$ (omitted for clarity). $\mathbf{M}$ and $\mathbf{M}'$ are symmetric about $\mathbf{E}_R$.

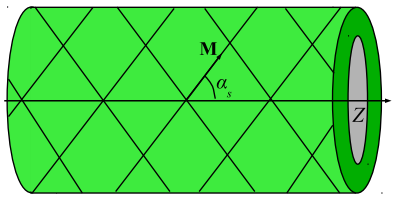

(b) Intra-lingual sheaths

Figure 5.5: Fibre arrangement in the accelerator muscle and intra-lingual sheaths. In the accelerator muscle, the fibres lie in the cross-sectional plane and spiral outwards from the centre. The fibres in the intra-lingual sheaths are arranged helically.

rations. First, in the relaxed configuration the intra-lingual sheaths surround the entoglossal process and are surrounded by the accelerator muscle. We assume there are no gaps between layers and there is zero traction acting on the exterior curved surface of the accelerator muscle. We also impose continuity of radial stress at the boundary of the sheath bundle and muscle, and no applied loads on the end of the tongue. Therefore, we have the following

$$a_s = r_{ep}, \quad T_{a_{rr}}(b_a) = 0, \quad b_s = a_a, \quad T_{s_{rr}}(b_s) = T_{a_{rr}}(a_a), \quad N = 0, \quad \nu = 1, \quad (5.13)$$

where r_{ep} is the radius of the rigid entoglossal process. Demanding that the degree of muscle contraction, ν, is equal to 1 is not, technically-speaking, a boundary condition.

However it is convenient to include it here, because the only difference between the relaxed and armed configurations is that the accelerator muscle is active, so its fibres are contracted. In other words, in the armed configuration, we have

$$a_s = r_{ep}, \quad T_{a_{rr}}(b_a) = 0, \quad b_s = a_a, \quad T_{s_{rr}}(b_s) = T_{a_{rr}}(a_a), \quad N = 0, \quad \nu = \nu^c, \tag{5.14}$$

where $\nu^c < 1$, that is, the muscle fibres are contracted. Finally, in the projected configuration the sheaths no longer surround the entoglossal process and are able to telescope. This means that only the outermost sheath is deformed, due to its connection to the accelerator muscle. Therefore, we ignore all other sheaths in this configuration, since they make no contribution to the elastic energy of the system and use a_{n_s} to denote the deformed inner radius of the outermost sheath. We assume the muscle remains contracted, so that we have the following

$$T_{s_{rr}}(a_{n_s}) = 0, \quad T_{a_{rr}}(b_a) = 0, \quad b_s = a_a, \quad T_{s_{rr}}(b_s) = T_{a_{rr}}(a_a), \quad N = 0, \quad \nu = \nu^c. \tag{5.15}$$

We are particularly interested in the amount of stored elastic energy converted to kinetic energy during projection. The elastic energy stored in any configuration is given by

$$\mathcal{E} = 2\pi l \left[\int_{a_s}^{b_s} r_s W_s \mathrm{d}r_s + \int_{a_a}^{b_a} r_a W_a \mathrm{d}r_a \right]. \tag{5.16}$$

The difference between the elastic energy of two different configurations of the tongue indicates the amount of elastic energy converted to kinetic energy during the transition between these states.

5.3.1 Model Parameters

In Table 5.1 we give typical values of model parameters that can be determined using information available in existing literature. It is important to note that representative

Observed	Value	Notes
r_{ep}	0.85mm	[105]
A_a	1.40mm	[18]
B_a	2.10mm	[18]
L_a	9.80mm	[18]
α_a	45°	[97]
α_s	50°	[18]
n	15	[18]

Table 5.1: Model parameters based on experimental observations. In the case of α_s the fibre angle varies along the length of the entoglossal process. The stated value lies in the observed range and is taken to be closer to the angle of the anterior portion, which is surrounded by the accelerator muscle.

Parameter	Value	Source
μ_{1_s}, μ_{1_a}	10kPa	Assumed to be similar of the same order of magnitude of other isotropic soft tissues [85].
μ_{4_s}	0.33GPa	[29, 85].
μ_{4_a}	0.07GPa	Taken to be approximately a fifth of μ_{4_s} since muscle fibre stiffness varies between that of elastin and collagen [85].

Table 5.2: Estimates of material parameters, based upon available data of similar biological tissues.

values could not be found for all model parameters: the stress-free geometry of the intra-lingual sheaths, the material parameters and the degree of muscle contraction must be estimated. In the case of the material parameters, our estimates are based upon properties of similar soft tissues, and these are given in Table 5.2.

A key part of our analysis will be to consider the effect of parameter choices on the mechanical behaviour of the tongue model (see Chapter 5.6.1). Before doing so, we estimate the remaining unknown parameters and obtain the resulting elastic energy difference between the armed and projected configurations. This difference indicates the amount of energy in the system that is available for ballistic acceleration.

5.4 Accelerator Muscle Contraction

We first consider the hypothesis that muscle contraction alone can account for large accelerations. We do so by neglecting the deformation of the intra-lingual sheets and assuming that the inner surface of the accelerator muscle remains in contact with a fixed boundary during protrusion. In other words, we prescribe the boundary conditions

$$a_a = A_a, \quad T_{a_{rr}}(b_a) = 0, \quad N = 0. \tag{5.17}$$

For a range of fibre angles we prescribe a degree of muscle contraction and solve the static equilibrium equation (5.10) subject to (5.17).

In Figure 5.6(a) the level sets of the axial stretch are plotted as functions of the muscle contraction, ν and muscle fibre angle, α_a. The axial stretch, λ_a increases monotonically as the muscle contracts (ν decreases). Moreover, for a fixed degree of muscle contraction, λ_a increases with the fibre angle, so the greatest axial extension occurs when the fibres are circumferentially arranged and highly contracted. When $\nu = 1$ the muscle is inactive and no deformation occurs. For our choice of muscle fibre angle ($\alpha_a = 45^\circ \approx 0.78$) we observe an axial stretch of 1.33 and this is consistent with experimental observations when ν is approximately 0.75.

Figure 5.6(b) shows the pairs of values (ν, α_a) for which the radial stress acting on the inner fascia of the accelerator muscle is equal to zero. The fascia is stress-free when $\nu = 1$, since this value corresponds to no muscle activity. There exist several other branches of the zero-stress contour, so that the parameter space under investigation is divided into regions corresponding to radial compression and radial tension. The regions of radial tension arise as a consequence of the condition that the muscle must remain structurally attached to the outermost sheath, which we have (for now) assumed to be fixed. The inner fascia of the muscle must be under local radial compression in the armed configuration in order for the entoglossal process to

exert a positive normal reaction force (as in Figure 5.2). Thus, the value of the fibre angle has an important effect upon the degree of muscle contraction that can occur before projection becomes impossible. Based on our choice of muscle fibre angle, the maximum degree of fibre contraction permitted is approximately 0.65.

By considering the axial stretch of the muscle and radial stress acting on its inner surface, we have obtained two estimates of the degree of muscle contraction in the armed configuration. As a representative value of ν to be used in the remainder of this chapter, we will therefore use their average, so that $\nu = 0.7$. In the armed configuration, a minimum of approximately 72mJ of elastic energy is required for rapid projection, but as Figure 5.7 shows, the energy stored in the muscle when $\nu = 0.7$ is less than 1mJ. This result confirms that Gnanamuthu's hypothesis of acceleration caused solely by muscular activity is indeed implausible.

5.5 Reference Configuration of the Intra-Lingual Sheaths

The intra-lingual sheaths, which are situated between the muscle and entoglossal process, are an essential component of the chameleon's tongue. We do not assume that the sheaths are stress-free in the relaxed configuration. It is possible for them to have their own stress-free length and radius, but when loaded onto the entoglossal process, they are constrained geometrically so that they are stressed. We will consider various choices of reference configuration where the inner radius of the sheath bundle is less than the the radius of the entoglossal process, *i.e.* $A_s < r_{ep}$. The case $A_s > r_{ep}$ is physically irrelevant, because if it were true, no morphological feature of the tongue's anatomy could ensure that the sheaths remain inside the chameleon's mouth whilst the accelerator muscle is inactive.

We seek pairs of values (L_s, A_s) for which the sheaths are subject to zero exter-

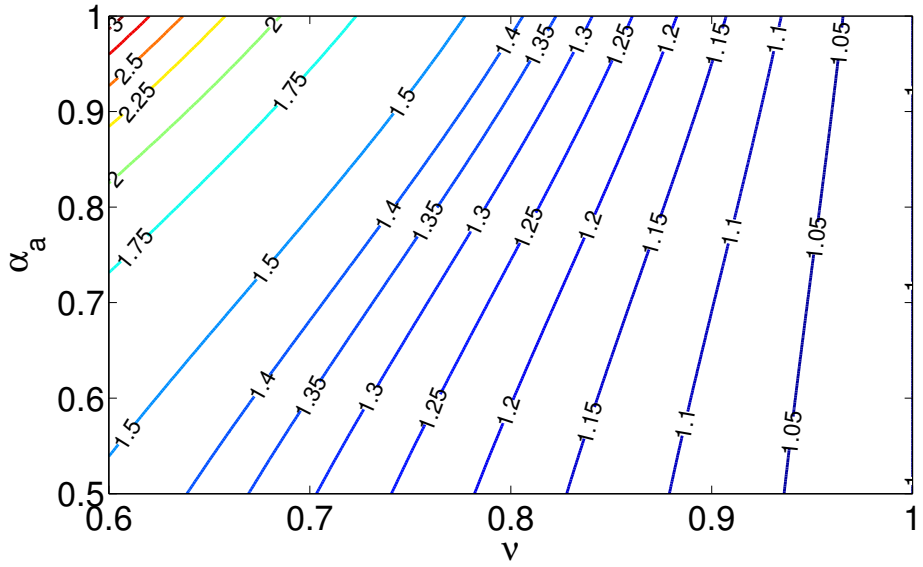

(a) Contours of constant axial stretch, λ_a as a function of fibre angle and degree of muscle contraction.

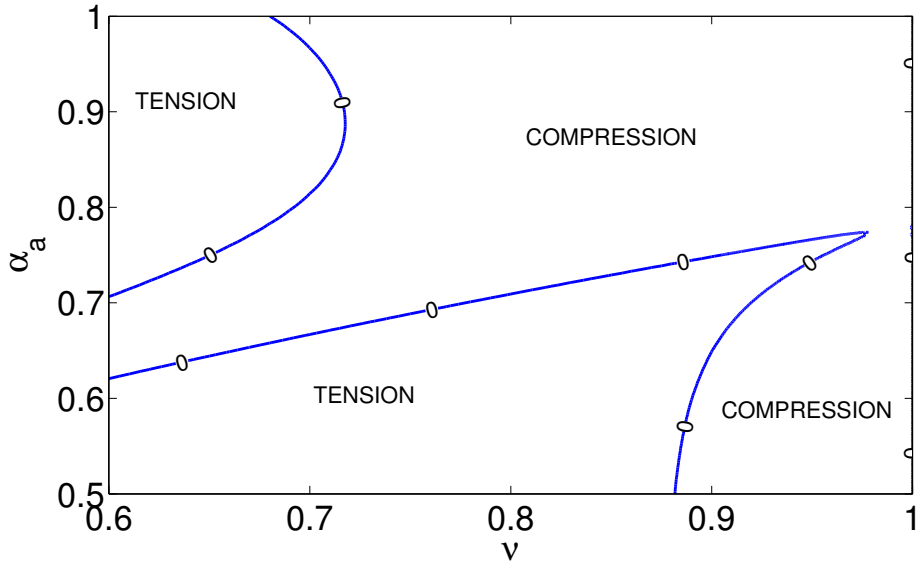

(b) Contours of zero radial stress acting on the inner fascia of the muscle, $T_{rr}(a_a)$.

Figure 5.6: Results of the isolated accelerator muscle problem assuming the fibres are arranged in logarithmic spirals in the cross-sectional plane. The parameter values used are given in Tables 5.1 and 5.2.

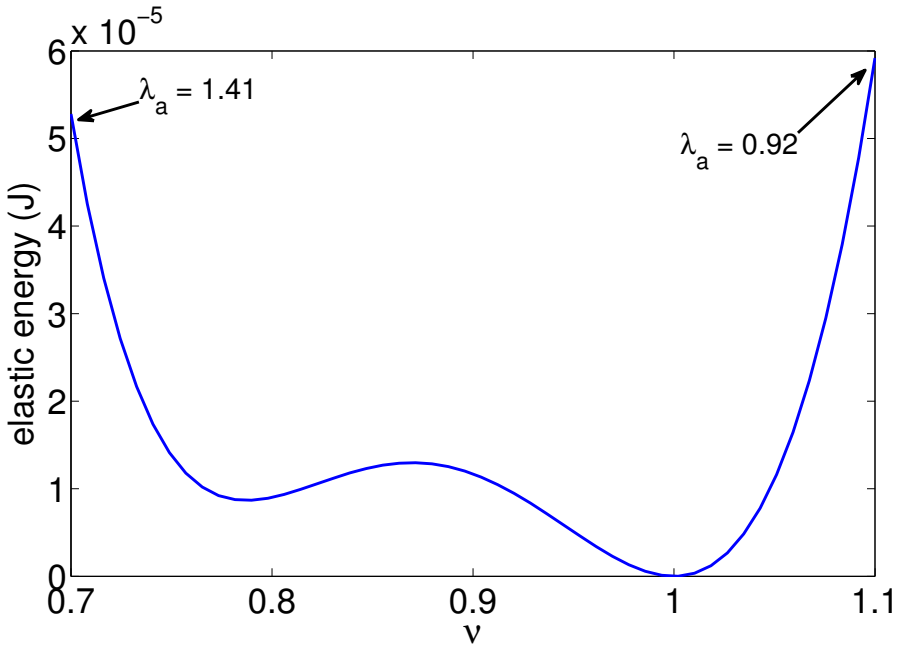

Figure 5.7: Elastic energy stored in accelerator muscle as a function of muscle contraction, ν, when no sheaths are present. The energy is not sufficient for rapid projection to occur, even in the case of large muscle contractions.

nal radial stress and zero normal loading when they are deformed into the relaxed configuration. That is, we seek solutions of (5.10) satisfying (5.13). This condition will ensure that in the absence of active muscle stress, the sheath bundle remains in static equilibrium on the entoglossal process.

The curve in Figure 5.8 shows the values of (L_s, A_s) satisfying these equations. The shaded region indicates stress-free geometries that give rise to a tensile radial stress (*i.e.* $T_{s_{rr}} > 0$) acting on the inner fascia of the sheath bundle in the relaxed configuration, whilst the unshaded region corresponds to a compressive radial stress (*i.e.* $T_{s_{rr}} < 0$). A compressive radial stress is required for the inner fascia to remain in contact with the entoglossal process. If the magnitude of the radial stress is large, friction between the inner fascia of the sheath bundle and the entoglossal process is also large, so that sliding of the sheath bundle is inhibited. Thus it is reasonable to expect that the actual geometry lies on the portion of the curve lying close to the boundary with the shaded region. As potential reference geometries, we consider

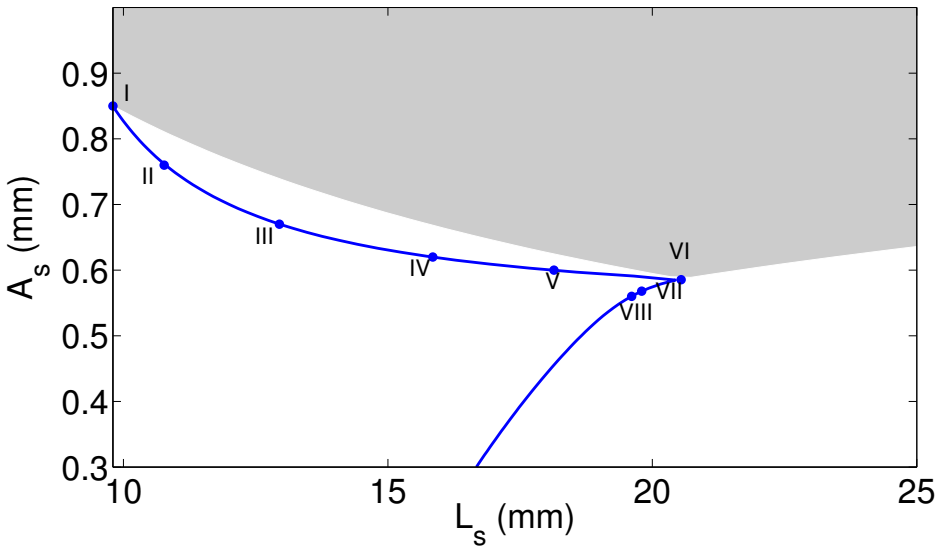

Figure 5.8: Values of the stress-free inner radius, A_s, and length L_s, of the sheaths for which the axial load N, acting in the relaxed configuration is equal to zero. The fibre angle of the sheaths is $\alpha_s = 50°$. The shaded region indicates reference geometries for which the radial stress acting on the inner surface of the sheaths is tensile ($T_{rr}(a_s) > 0$) in the relaxed configuration, whilst the unshaded region indicates reference geometries for which the radial stress acting on the inner surface of the sheaths is compressive ($T_{rr}(a_s) < 0$) in the relaxed configuration.

Reference	A_s(mm)	B_s(mm)	L_s(mm)
I	0.85	1.40	9.8
II	0.76	1.31	10.8
III	0.67	1.18	12.9
IV	0.62	1.07	15.8
V	0.60	1.01	18.1
VI	0.58	0.97	20.5
VII	0.57	0.97	19.8
VIII	0.56	0.97	19.6

Table 5.3: Potential reference configurations of the sheath bundle when $\alpha_s = 50°$. Each satisfies the conditions of zero normal loading applied to the ends of the bundle and negative radial stress on the inner fascia.

the sample range of points indicated in Figure 5.8, which we refer to as Geometries I-VIII. These are also given explicitly in Table 5.3. Geometry I is the case in which the sheaths are stress-free in the relaxed configuration, whilst the other cases have a smaller inner radius, A_s, so the sheath bundle must be stretched radially to fit onto the entoglossal process.

5.6 Energy Comparison

Using the parameter values given in Chapter 5.3.1 and each choice of sheath bundle reference geometry in Table 5.3 we vary the degree of muscle contraction, ν, and solve (5.10) subject to (5.14) to obtain the axial stretch of the soft tissues and corresponding elastic potential energy of the system in the armed configuration. We then repeat the process, with (5.14) replaced by (5.15) to find the same quantities in the projected configuration. The difference in the elastic energy between the two configurations provides an estimate of the amount of kinetic energy available during projection.

The curves depicted in Figure 5.9(a) show the axial stretch of the muscle and sheath bundle during protrusion for each choice of sheath bundle reference geometry given in Table 5.3. On each curve the point at which the stored elastic energy in the accelerator muscle is equal to its maximum limit (see Chapter 5.2) is marked by a

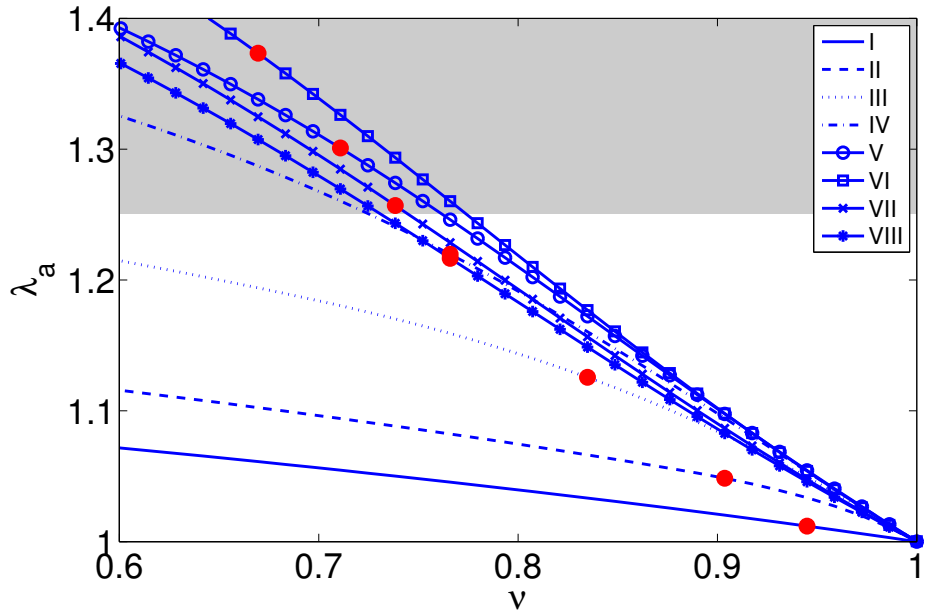

(a) Muscle contraction vs. axial stretch of muscle. The shaded region indicates an axial stretch greater than 25%.

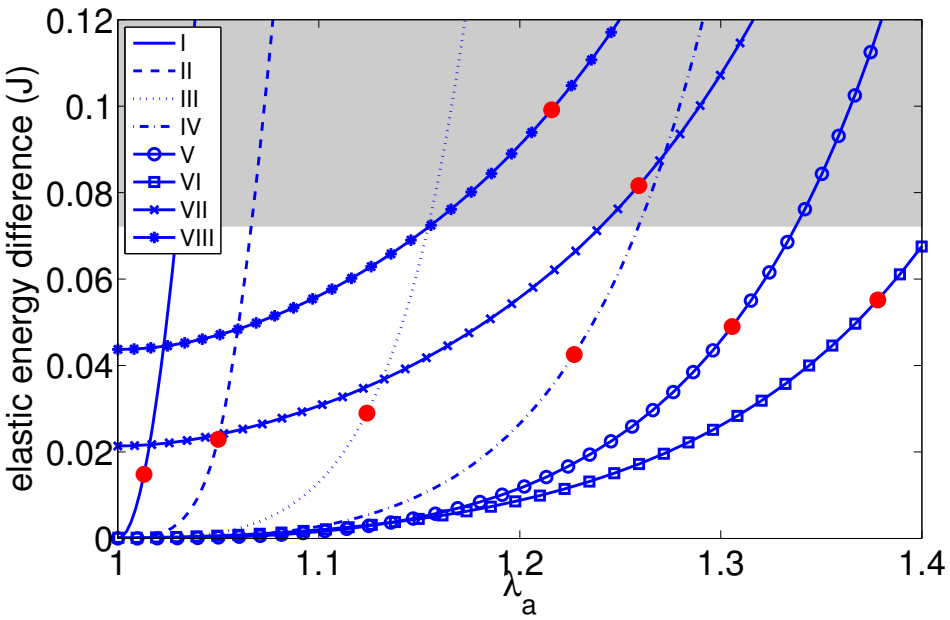

(b) Stored elastic energy vs. axial stretch of accelerator muscle. The shaded region indicates elastic energies that are greater than 72mJ and therefore sufficient for ballistic projection.

Figure 5.9: Results of the fully-coupled problem assuming a fixed boundary condition at $r = a_s$ for each choice of reference configuration of the sheath bundle. Red circles denote the point at which the energy stored in the accelerator muscle is 15mJ.

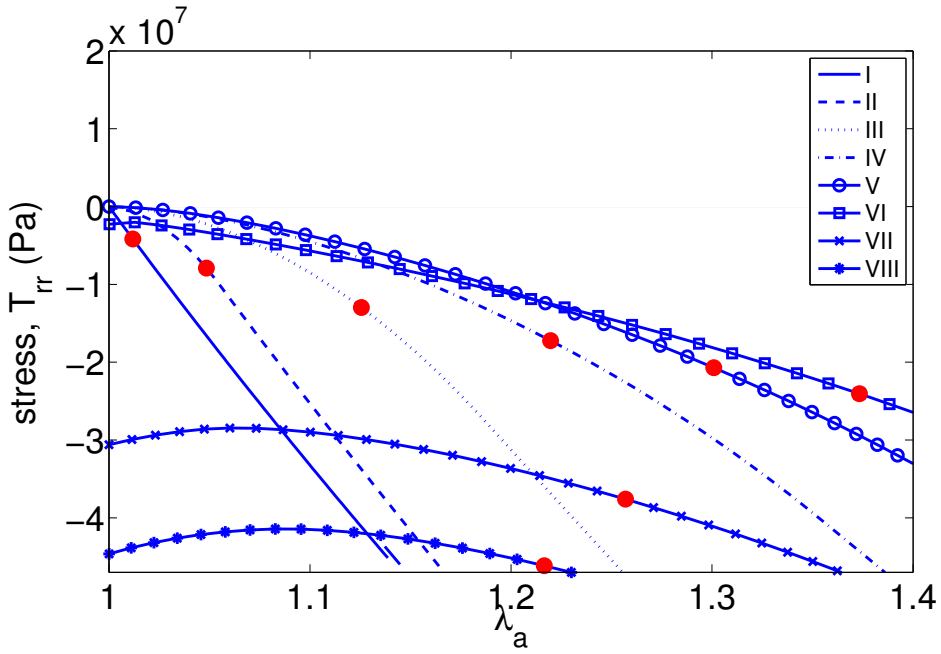

Figure 5.10: Radial stress acting on the inner fascia of the intra-lingual sheaths as a function of axial stretch. Red dots indicate the points at which the accelerator muscle reaches its maximum energy storage capacity.

solid red circle. It is essential that muscle contraction produces a sufficiently large axial stretch before reaching its maximum work capacity for the sheaths to begin sliding off the entoglossal process. Based on an observed stretch of up to 33% during the protrusion phase [18], we will consider all extensions greater than 25% as being suitable for projection. We conclude that the armed configuration can be reached only in the cases of Geometries V-VII. The small extension observed in Geometries I-V is due to the collagen fibres in the sheaths. Because of their high stiffness, it is difficult for the muscle to extend the sheaths very far beyond their stress-free length. In the case of Geometries V-VII, the sheaths are sufficiently compressed in the relaxed configuration, relative to their stress-free length, that they are less resistant to axial extension. However, as A_s decreases, the sheaths experience an increasing level of radial compression whilst surrounding the entoglossal process. This compression increases their resistance to further radial compression under the action of the accelerator muscle thereby rendering axial elongation increasingly difficult.

Thus, in the case of Geometry VIII, the axial stretch obtained when the muscle reaches its work capacity is lower than the observed target of 33%, even though the sheaths are compressed in the relaxed configuration.

Figure 5.9(b) shows the difference in elastic energy before and after projection as a function of axial stretch. When $\lambda_a = 1$ (equivalent to no muscle activity), the sheaths store very little energy in the case of Geometries I-VI, but for Geometries VII and VIII the sheaths store around 20-50mJ of elastic energy in the relaxed configuration. As the axial stretch increases, the elastic energy available for projection also increases, but out of those investigated only Geometries VII and VIII yield at least the required estimate of 72mJ of energy for projection, without exceeding the capacity of the accelerator muscle. Of these two Geometries, VIII yields more kinetic energy for projection, though the radial stress acting on the inner fascia in the armed configuration is greater (see Figure 5.10), thus resulting in increased friction as it slides over the entoglossal process, which could inhibit projection. Moreover, the axial extension observed in the case of Geometry VII is greater, thereby increasing the range of capture, but this is most likely a comparatively small effect when the telescopic action of the sheaths and extension of the hyglossus complex is taken into account.

When the two criteria of a minimum axial stretch and a minimum kinetic energy are considered together, we conclude that there exists a region of the $N = 0$ contour in Figure 5.8 lying between Geometries VI and VIII for which both requirements are met, under our choices of representative parameter values. However, we note that an estimated kinetic energy of less that 72mJ does not render projection impossible; it may occur, albeit with a reduced acceleration. Similarly, the required axial stretch in the armed configuration is dependent upon the distance between the anterior end of the accelerator muscle and the tip of the entoglossal process, which varies from one chameleon to another. Therefore, it is important to consider variations in the model's

parameters, which we present in the following section.

5.6.1 Sensitivity Analysis

We examine changes in the model's results with variations in the geometry and material constants by means of a sensitivity analysis. We consider the effect of variations in the model parameters about a prescribed set of values upon both the axial stretch before projection and the kinetic energy achieved during projection for a known degree of muscle contraction (see Appendix B for details). For the base values of the parameters we use Geometry VII, along with those given in Tables 5.1 and 5.2.

In Figure 5.11 the set of base parameters is given along with a plot showing the mean absolute value of the sensitivity parameter. The kinetic energy is highly sensitive to variations in both the stress-free inner radius and fibre angle of the sheath bundle, and the radius of the entoglossal process. Interestingly, the choice of sheath bundle reference geometry plays a crucial role in determining whether ballistic projection is possible. In particular, the fibre angle and degree of radial stretching experienced by the sheaths in the relaxed configuration determines how readily they will undergo axial extension due to contraction of the accelerator muscle fibres. If ballistic projection is to be achieved, we may expect to see a high level of uniformity in the ratio r_{ep}/A_s and fibre angle α_s across several different specimens of chameleon. In contrast, the kinetic energy exhibits little sensitivity to the the geometry of the accelerator muscle and the material parameters, whilst the axial stretch shows little sensitivity to any of the material or geometric parameters. It is therefore reasonable to expect a greater level of variation in these parameters across several specimens of chameleon, since variations do not greatly affect the maximum extension, nor the velocity of the tongue.

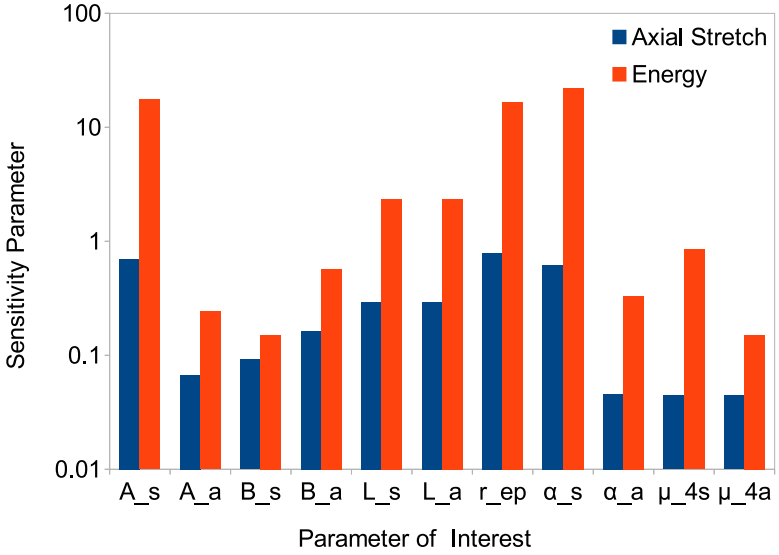

Figure 5.11: Sensitivity analysis results for the fully-coupled boundary value problem. In all cases the degree of muscle contraction was fixed at $\nu = 0.7$ and the base parameter values are given in Table 5.4. Note the logarithmic scale.

Quantity	P	P_0
Sheath stress-free inner radius	A_s	0.57mm
Muscle stress-free inner radius	A_a	1.40mm
Sheath stress-free outer radius	B_s	0.97mm
Muscle stress-free outer radius	B_a	2.11mm
Sheath stress-free length	L_s	19.80mm
Muscle stress-free length	L_a	9.80mm
Sheath fibre angle	α_s	50°
Muscle fibre angle	α_a	40°
Sheath fibre stiffness	μ_{4_s}	0.50GPa
Muscle fibre stiffness	μ_{4_a}	0.07GPa
Entoglossal process radius	r_{ep}	0.85mm

Table 5.4: Base values of each of the model's estimated parameters: the inner and outer radii, length, fibre angle and fibre stiffness of the muscle and sheaths, and the radius of the entoglossal process.

5.7 Conclusion

In this chapter we have developed a biomechanical model of the chameleon's tongue to study its energy landscape. The well-developed framework of non-linear elasticity has enabled us to analyse in depth the effect of varying geometry, fibre angle and material properties on the projection mechanism.

We have demonstrated that muscle contraction alone cannot account for the high power acceleration of the chameleon's tongue that has been observed experimentally. This result is due to the fact that the energy storage capacity of the muscle is lower than the kinetic energy required for rapid projection. When the intra-lingual sheaths are included the energy storage capacity of the system increases and it is this greater amount of stored elastic energy that allows the chameleon to catch prey before they are able to react and evade capture. Our framework allows estimation of the range of reference geometries of the intra-lingual sheaths that yield sufficient energy for fast projection; these values could be measured in practice, though very careful dissection of the lingual apparatus would be required.

Our model also allows us to consider the question of optimality: has evolution (in some sense) led to a tongue morphology that is optimised for its role? This is a difficult question to answer, since there is no clear definition of what an optimal design is. For instance, if the aim were to maximise the extension of the tongue, to obtain a long range of capture, whilst demanding that the energy remains above the required target of 72mJ, we could argue that Geometry VII is the optimal sheath reference geometry for our choice of model parameters. However, if we wished to maximise extension then Geometry VI would be the optimal choice, at a cost of reduced energy. Geometry VIII (and beyond) provides more energy at a cost of reduced extension and greater radial stress acting on the entoglossal process.

We have neglected some of the morphological features of the hyolingual complex that may play an important role in prey capture in addition to those we have focussed

on, such as the rounded tip of the entoglossal process and the anterior non-annular portion of the accelerator muscle. Furthermore, the model presented here is static, and as such does not capture the complex motion of the sheaths, muscle and tongue pad during projection. A model of the full projection dynamics would allow a more detailed analysis of the kinetic energy available for projection and estimation of the range and speed of projection. However this study would be complicated by the fact that the muscle and sheaths cannot be assumed to be cylindrical as they slide off the tapered anterior end of the entoglossal process. Therefore consideration of a wider class of deformation is necessary, which in turn yields a more complex system of equilibrium equations than (3.17). Moreover, the introduction of time-dependence into the problem could result in phenomena such as travelling waves, oscillations, the effects of inertial foraces and damping. These features may act to reduce the overall useful energy that is available for projection, which could limit further the range of potential reference configurations of the sheaths and other parameter values for which rapid projection will be feasible.

Chapter 6

Conclusion

In this thesis, we have sought a greater understanding of the complex relationship between growth and stress, as well as their effects on biological systems. In addition to identifying the main characteristics of biological tissue, such as growth, residual stress, anisotropy, remodelling and incompressibility, we have surveyed existing modelling frameworks and established that there is a demand for modelling approaches to biomechanical problems that can account for these features, especially in complex spatial domains. This is a difficult task, but by restricting our attention to filamentary structures, we have been able to take steps towards the development of such a framework, because they can be idealised as elastic cylinders. Under this assumption, the powerful framework of non-linear elasticity provides a means of obtaining detailed information about the stress profiles throughout the body. However, it is difficult to explore fully the space of possible deformations because the equations of equilibrium only remain simple as long as the cylindrical form is preserved. To study more geometrically complex deformations, we can use rod theory, in which the geometry of the structure is approximated by a 1-D space curve. This has the disadvantage of being unable to account for residual stresses. One way of combining the strengths of each model is as follows:

1. use non-linear elasticity to determine the mechanical properties of a filament, *including* the effects of residual stress;

2. map these properties from the 3-D framework into an 'effective' elastic rod;

3. use rod theory to study geometrically-complex deformations of this effective rod.

The effective rod is not residually-stressed in its undeformed configuration. Rather, the mechanical effects of residual stress are encapsulated in its constitutive laws. Our focus has been the first two of these stages.

In Chapter 3, we focussed on deriving the effective stiffnesses of a one-layer cylinder subject to non-uniform growth. We considered six different types of growth, which are representative of those observed in the natural world. Given a particular growth law, we presented a method for obtaining analytic estimates of the effective axial, torsional and bending stiffness in the case of an isotropic body, in terms of the stress-free geometry and strain-energy density of the constituent material. We assumed the growth was close to uniform for the sake of analytic tractability, but we also showed that these estimates could also be derived numerically, so that more 'extreme' growth profiles can be studied. In most cases, the results showed good agreement with corresponding results obtained numerically, though for larger deviations from uniform, stress-free growth, they were less reliable. However, it is important to remember that our comparison was based on one particular choice of strain-energy density, and others may perform differently. Our results yielded interesting insight into the role of residual stress in growing filaments: it allows a greater range of combinations of stiffnesses to be attained than when only uniform growth is considered, and in some cases it is able to counteract a change in stiffness caused by variations in the cross-sectional area. In other words, differential growth allows an initially stress-free cylinder to grow in such a way that its cross-section reduces in size, but it

becomes more difficult to bend or twist. This is not possible in the case of isotropic, uniform growth. Furthermore, we investigated the inverse problem of whether it is possible, given a particular stress-free configuration and desired unloaded geometry and stiffnesses, to find a suitable growth law that will yield these values. Sometimes it is possible, and there may be more than one growth law available, but we were not able to find solutions in all cases. Furthermore, since our inverse approach relies on the asymptotic approximations to the effective stiffnesses, we must ensure that the difference between the approximations and numerical results is not too great, especially if the values of the incremental growth parameters are found to be large.

In Chapter 4, we continued the theme of using 3-D, non-linear elasticity to inform parameter choices in rod theory approaches by investigating the role of a second layer of soft tissue. Here, we considered a filament embedded in an elastic matrix subject to constrained axial growth. We assumed the outer layer was sufficiently thick that it could be modelled as a Winkler foundation, in line with many other previous studies. Our aim was to determine the foundation modulus parameter. Unlike previous studies, we sought an estimate of the foundation modulus that depends only upon the measurable properties of the system, and not the buckled wavelength of the filament. We did so using by comparing the critical growth obtained using an asymptotic approximation to the non-linear theory with that obtained using rod theory. We also derived a simpler approximation for the foundation modulus by fitting the critical growth and observed buckling wavelength obtained using each approach, under the assumption that the foundation modulus is directly proportional to the shear modulus of the matrix. However, our analysis was limited to the case in which both the filament and matrix are made of a neo-Hookean material, due to the complexity of the non-linear governing equations. We were able to investigate numerically the effect of using a Mooney-Rivlin material and found the same behaviour as the neo-Hookean case, but there is scope for further investigation into the behaviour of other isotropic

strain-energy densities.

In Chapter 5, we considered a real-world application of the non-linear elasticity framework, namely the chameleon's tongue. Here we constructed a mechanical model of the tongue to investigate the theory that high-powered acceleration is achieved via an energy storage-and-release mechanism. We were able to provide evidence to support this theory by estimating the energy stored in the soft tissues of the tongue prior to, and immediately after projection. This process revealed that residual stress could play an essential role in projection. If the intra-lingual sheaths are stress-free when the accelerator muscle is relaxed, then there is not enough energy in the system in the armed configuration for rapid acceleration to occur. Instead, the three major structures each play a vital role: the entoglossal process acts as a rigid central foundation for the ballistic apparatus, the elastic sheaths are loaded whilst in contact with the entoglossal process, because they have a smaller stress-free radius than the process, and the accelerator muscle initiates projection via fibre contraction. The stress-free geometry of the elastic sheaths plays a particularly important role. Only with a limited range of geometries can sufficient energy for rapid projection be achieved, and we also showed by means of a sensitivity analysis that the energy is particularly sensitive to variations in the reference geometry of the sheaths, including the orientation of their fibres. Overall, we demonstrated that the mechanism of projection proposed by de Groot and van Leeuwen is plausible when the energy available for projection is considered.

In summary, we have made progress in developing a general framework for modelling growth and residual stress in soft tissue, and examined their role in real-world problems. We have also identified several extensions to this work that could yield further insight into such systems. We now discuss these in further detail.

6.1 Future Work

One of the simplest extensions to the work detailed in Chapter 3 is to investigate the growth of fibre-reinforced cylinders. General anisotropic strain-energy densities may prove to be more difficult to investigate analytically, due to the increase in complexity of the governing equations. However, in the simplest case, the anisotropic contribution to the strain-energy density would be similar to that in (5.11) or (5.12), so that there is no additional contribution to the off-diagonal elements of the Cauchy stress tensor and the equations of equilibrium remain simple. This assumption would enable us to investigate the influence of fibre angle on the mechanical properties of a differentially growing cylinder, which would have applications to various systems, including airways, arteries, plant stems and the gastrointestinal tract. The investigation of larger growth gradients could be facilitated by considering more terms in the asymptotic expansion of the growth laws, and the study of other types of growth law could reveal interesting phenomena that have not been observed in our studies. The choice of these laws will depend upon the underlying biology of the problem, but possibilities include piecewise constant or linear functions of the radius, representing situations in which the growth takes place only in certain layers of the tissue. The theory is well-developed, as we have seen in Chapter 4, so there is much potential for interesting insight. One important issue to consider in the case of large growth gradients is cavitation, in which a solid cylinder may develop a void at the centre when the radial stress at the centre reaches some critical value. Cavitation occurs only in the case of certain strain-energy densities [34], but when it is possible for cavitation to occur, it would be interesting to compare the effective stiffnesses of the cavitated and uncavitated solutions of the governing boundary value problem.

Possible extensions to the work detailed in Chapter 4 include considering the behaviour of anisotropic layers. The non-linear elasticity framework can easily be adapted to account for anisotropic effects by modifying the strain-energy density.

The components of the fourth order tensor of instantaneous elastic moduli are already known for a fibre-reinforced material and are given in [35]. Furthermore, a key assumption of our model was that the outer layer behaved as a Winkler foundation, whereby the the transverse force acting on a point in the rod scaled linearly with its displacement. However, this approach does not accurately capture the true mechanical response of the foundation, because shearing of the foundation is not taken into account. There are many other choices of foundation model available, but a common choice is to use a Pasternak model, in which case the body force vector is given by

$$\mathbf{f} = \left(-k_f y + G_f \frac{\partial^2 y}{\partial z^2} \right) \mathbf{e}_2, \tag{6.1}$$

where k_f is the Winkler foundation modulus and G_f is the shear modulus of the elastic matrix. Another interesting problem related to this work is the case in which the matrix is much stiffer than the embedded rod. Here, we expect the post-buckled configuration of the rod to be non-planar [92], which requires modification of the incremental equilibrium equations in both the rod theory and 3-D elasticity approaches, but there exist studies such as [6] that could easily be adapted for this purpose.

Finally, we consider extensions to the study of the chameleon's tongue. At the end of Chapter 5, we discussed the potential use of a dynamic model of projection. Using the framework of non-linear elasticity, the governing equations of the dynamic problem would be straightforward to formulate, though it is likely that computational methods would be required to solve them. The benefit of such an approach would be that we would be able to determine for sure whether the energy 'spent' by the tongue in changing from the armed to projected configurations is indeed used for axial acceleration. Another feature that could be incorporated into the model is the distribution of fibres in a material, which can be accounted for by defining a structure tensor, $\mathbf{H}$, representing this distribution of fibre direction and making W

dependent on **H**. This approach has been used by [72] to model the response of skin. To gain some analytic insight into the problem, it may be possible to exploit the small thickness of the intra-lingual sheaths, though a similar approximation cannot be made for the accelerator muscle. If such an approximation is made for the sheaths, then it may be necessary to alter our assumption that there are multiple, concentric layers and instead model the sheath bundle as a continuous, single, elastic sheath that is folded back and forth upon itself whilst on the entoglossal process. This refinement also leads us to consider the problem of tongue retraction: how is the ballistic apparatus able to reset following prey capture?

In summary, we have developed methods of accounting for the effects of differential growth, and residual stress in geometrically complex deformations of cylindrical structures. It is vital that mechanical models are able to account for these phenomena if we are to understand their role in biological systems. A major challenge for the future will be coupling growth at the cellular level with tissue-level mechanics, but the work described herein constitutes some progress in developing a morphoelastic modelling framework that gives interesting insights into the effects of differential growth. Furthermore, we have identified achievable goals for future work in this fascinating field of research.

Appendix A

Effective Stiffnesses

Here, we present the asymptotic estimates of the three effective stiffnesses, defined in Chapter 3, as well as the bending and torsional moduli. These are obtained by normalising the corresponding stiffness with respect to the relevant moment of area. In all cases, we have assumed the initial cylinder to be hollow (*i.e.* $A > 0$), but the corresponding result for the solid cylinder can be obtained by taking the limit of each term as $A \to 0$.

Growth	Axial Stiffness, $K_{n_3}^{(1)}$
I (CR)	$6\pi\gamma_{11}\gamma_{10}\left(\bar{W}_2+\bar{W}_1\right)\left(B^2-A^2\right)$
II (RR)	$2\pi\gamma_{11}\gamma_{10}\left(\bar{W}_2+\bar{W}_1\right)(B-A)\left(2\left(A^2+AB+B^2\right)-3R_0\left(A+B\right)\right)$
III (CC)	$6\pi\gamma_{21}\gamma_{10}\left(\bar{W}_2+\bar{W}_1\right)\left(B^2-A^2\right)$
IV (RC)	$2\pi\gamma_{21}\gamma_{10}\left(\bar{W}_2+\bar{W}_1\right)(B-A)\left(2\left(A^2+AB+B^2\right)-3R_0(A+B)\right)$
V (CS)	$4\pi\gamma_{21}\gamma_{10}\left(\bar{W}_2+\bar{W}_1\right)(B-A)\left(2\left(A^2+AB+B^2\right)-3R_0(A+B)\right)$
VI (RA)	0

Table A.1: $\mathcal{O}(\epsilon)$ terms of the effective axial stiffness. This is dominated by the geometry of the cross-section, so $K_{n_3} > K_{n_3}^0$ when $\mathcal{A}^* > \mathcal{A}_0$ and vice-versa.

Growth	Torsional stiffness, $K_{m_3}^{(1)}$
I (CR)	$\pi\gamma_{11}\gamma_{10}^3\left(4A^2B^2\bar{W}_1(\log(A)-\log(B))-\left(\bar{W}_2+2\bar{W}_1\right)\left(A^4-B^4\right)\right)$
II (RR)	$\frac{\pi\gamma_{11}\gamma_{10}^3}{15}\left(-3\bar{W}_2\left(4A^5-5A^4R_0+B^4(5R_0-4B)\right)-10\bar{W}_1\left(2A^5-3A^4R_0\right.\right.$ $\left.\left.-4A^3B^2+4A^2B^3+6A^2B^2R_0(\log(A)-\log(B))+B^4(3R_0-2B)\right)\right)$
III (CC)	$\frac{1}{6}\pi\gamma_{10}^2\left(6\gamma_{10}\left(B^4-A^4\right)\left(3\gamma_{21}\bar{W}_2+2\gamma_{21}\bar{W}_1\right)\right.$ $\left.-24A^2B^2\gamma_{10}\gamma_{21}\bar{W}_1\left(\log(A)-\log(B)\right)\right)$
IV (RC)	$\frac{\pi\gamma_{21}\gamma_{10}^3}{15}\left(-20A^5\bar{W}_1+30A^4R_0\bar{W}_1-80A^3B^2\bar{W}_1+80A^2B^3\bar{W}_1\right.$ $+60A^2B^2R_0\bar{W}_1\log(A)-60A^2B^2R_0\bar{W}_1\log(B)+20B^5\bar{W}_1$ $\left.-30B^4R_0\bar{W}_1-36A^5\bar{W}_2-45B^4R_0\bar{W}_2+45A^4R_0\bar{W}_2+36B^5\bar{W}_2\right)$
V (CS)	$\frac{-4}{15}\pi\gamma_{21}\gamma_{10}^3\left(5\bar{W}_1(A-B)\left(A^2+B^2\right)\left(2\left(A^2+AB+B^2\right)-3R_0(A+B)\right)\right.$ $\left.+3\bar{W}_2\left(4A^5-5A^4R_0+B^4(5R_0-4B)\right)\right)$
VI (RA)	$\frac{2\left(\pi\gamma_{31}\gamma_{10}^4\left(\bar{W}_2-2\bar{W}_1\right)(A-B)^3\left(A^2+3AB+B^2\right)\right)}{15\gamma_{30}}$

Table A.2: $\mathcal{O}(\epsilon)$ terms of the effective torsional stiffness.

Growth	Effective Torsional Modulus, $\mu_{m_3}^{(1)}$
I (CR)	$-\frac{2\gamma_{11}\left(B^4-A^4-4A^2B^2\left(\log(B)-\log(A)\right)\right)\bar{W}_2}{\gamma_{10}\left(B^4-A^4\right)}$
II (RR)	$-\frac{2\gamma_{11}\bar{W}_2}{15\gamma_{10}\left(A^4-B^4\right)}\left(15R_0\left(B^4-A^4\right)+60A^2B^2R_0(\log(A)-\log(B))\right.$ $\left.+8\left(A^2+3AB+B^2\right)(A-B)^3\right)$
III (CC)	$\frac{2\gamma_{21}\left(B^4-A^4-4A^2B^2\left(\log(B)-\log(A)\right)\right)\bar{W}_2}{\gamma_{10}\left(B^4-A^4\right)}$
IV (RC)	$\frac{2\gamma_{21}\bar{W}_2}{15\gamma_{10}\left(A^4-B^4\right)}\left(15R_0\left(B^4-A^4\right)+60A^2B^2R_0(\log(A)-\log(B))\right.$ $\left.+16\left(A^2+3AB+B^2\right)(A-B)^3\right)$
V (CS)	$\frac{16\gamma_{21}\left(A^4+A^3B-4A^2B^2+AB^3+B^4\right)\bar{W}_2}{15\gamma_{10}(A+B)\left(A^2+B^2\right)}$
VI (RA)	$\frac{4\gamma_{31}\left(\bar{W}_2-2\bar{W}_1\right)(A-B)^2\left(A^2+3AB+B^2\right)}{15\gamma_{30}(A+B)\left(A^2+B^2\right)}$

Table A.3: $\mathcal{O}(\epsilon)$ terms of the effective torsional modulus.

Growth	Bending stiffness, $K_{m_1}^{(1)}$
I (CR)	$\frac{1}{2}\gamma_{10}^3\pi\gamma_{11}\left(6\bar{W}_2\left(-A^4+2A^2B^2(\log(A)-\log(B))+B^4\right)\right.$
II (RR)	$\frac{\pi\gamma_{11}\gamma_{10}^3}{30}\left(\bar{W}_1\left(-52A^5+75A^4R_0+80A^3B^2-80A^2B^3\right.\right.$ $+120A^2B^2R_0(\log(B)-\log(A))+B^4(52B-75R_0)\big)$ $-30\bar{W}_2\left(2A^5-3A^4R_0-4A^3B^2+4A^2B^3\right.$ $\left.\left.+6A^2B^2R_0(\log(A)-\log(B))+B^4(3R_0-2B)\right)\right)$
III (CC)	$\frac{1}{6}\pi\gamma_{10}^2\left(6\gamma_{10}\left(A^4-B^4\right)\left(-3\gamma_{21}\bar{W}_2-2\gamma_{21}\bar{W}_1\right)\right.$ $\left.-24\gamma_{21}\left(A^2B^2\gamma_{10}\bar{W}_1\log(A)-A^2B^2\gamma_{10}\bar{W}_1\log(B)\right)\right)$
IV (RC)	$\frac{1}{30}\pi\gamma_{21}\gamma_{10}^3\left(\bar{W}_1\left(-76A^5+105A^4R_0-160A^3B^2+160A^2B^3\right.\right.$ $+B^4(76B-105R_0)+120A^2B^2R_0(\log(A)-\log(B))\big)$ $-30\bar{W}_2\left(2A^5-3A^4R_0+8A^3B^2-8A^2B^3\right.$ $\left.\left.+6A^2B^2R_0(\log(B)-\log(A))+B^4(3R_0-2B)\right)\right)$
V (CS)	$\frac{2}{15}\pi\gamma_{21}\gamma_{10}^3\left(\bar{W}_1\left(45R_0\left(A^4-B^4\right)-4\left(8A^5+5A^3B^2-5A^2B^3-8B^5\right)\right)\right.$ $\left.-15\bar{W}_2(A-B)\left(A^2+B^2\right)\left(2\left(A^2+AB+B^2\right)-3R_0(A+B)\right)\right)$
VI (RA)	$\frac{2\left(\pi\gamma_{31}\gamma_{10}^4\left(3\bar{W}_2+\bar{W}_1\right)(A-B)^3\left(A^2+3AB+B^2\right)\right)}{15\gamma_{30}}$

Table A.4: $\mathcal{O}(\epsilon)$ terms of the effective bending stiffness.

Growth	Effective Bending Modulus, $\mu_{m_1}^{(1)}$
I (CR)	$-\frac{2\gamma_{11}\left(B^4-A^4-4A^2B^2\left(\log(B)-\log(A)\right)\right)\bar{W}_1}{\gamma_{10}\left(B^4-A^4\right)}$
II (RR)	$-\frac{2\gamma_{11}\bar{W}_1}{15\gamma_{10}\left(A^4-B^4\right)}\left(15R_0\left(B^4-A^4\right)+60A^2B^2R_0(\log(A)-\log(B))\right.$ $\left.+8\left(A^2+3AB+B^2\right)(A-B)^3\right)$
III (CC)	$\frac{2\gamma_{21}\left(B^4-A^4-4A^2B^2\left(\log(B)-\log(A)\right)\right)\bar{W}_1}{\gamma_{10}\left(B^4-A^4\right)}$
IV (RC)	$\frac{2\gamma_{21}\bar{W}_1}{15\gamma_{10}\left(A^4-B^4\right)}\left(15R_0\left(B^4-A^4\right)+60A^2B^2R_0(\log(A)-\log(B))\right.$ $\left.+16\left(A^2+3AB+B^2\right)(A-B)^3\right)$
V (CS)	$\frac{16\gamma_{21}\left(A^4+A^3B-4A^2B^2+AB^3+B^4\right)\bar{W}_1}{15\gamma_{10}(A+B)\left(A^2+B^2\right)}$
VI (RA)	$\frac{4\gamma_{31}\left(\bar{W}_2-2\bar{W}_1\right)(A-B)^2\left(A^2+3AB+B^2\right)}{15\gamma_{30}(A+B)\left(A^2+B^2\right)}$

Table A.5: $\mathcal{O}(\epsilon)$ terms of the effective bending modulus.

Appendix B

Derivation of Sensitivity Parameter

Here, we give details of the sensitivity parameter used in Chapter 5.

First, let P be the parameter of interest, which has base value P_0, and V be the dependent variable of interest. We solve the relevant boundary value problem using the set of base parameters to find the associated value of V, which we shall call V_0. We then vary P so its new value is P_1 and solve the same system of equations to find V_1, the new value of V. We then define $s_{V,P}$, to be the following

$$s_{V,P} = \frac{(V_1 - V_0)/V_0}{(P_1 - P_0)/P_0}. \tag{B.1}$$

In other words, it is the ratio of the relative change in the dependent variable to the relative change in the model parameter. The larger the magnitutde of $s_{V,P}$, the more sensitive the dependent variable is to the parameter of interest. Repeating this process for each of the model's parameters allows us to determine which have the greatest and least effect on the dependent variables. We consider both a 5% increase and 5% reduction of each parameter's base value and calculate $s^+_{V,P}$ and $s^-_{V,P}$ respectively. Finally, we define the sensitivity parameter $S_{V,P}$ to be the mean of their absolute values, *i.e.*

$$S_{V,P} = \frac{\left|s^+_{V,P}\right| + \left|s^-_{V,P}\right|}{2}. \tag{B.2}$$

Bibliography

[1] B. Alberts, D. Bray, J. Lewis, M. Raff, K. Roberts, and J. D. Watson. *Molecular Biology of the Cell*. Garland Publishing, 5th edition, 2008.

[2] M. B. Amar, M. M. Müller, and M. Trejo. Petal shapes of sympetalous flowers: the interplay between growth, geometry and elasticity. *New Journal of Physics*, 14(8):085014, 2012.

[3] D. Ambrosi, G. A. Ateshian, E. M. Arruda, S. C. Cowin, J. Dumais, A. Goriely, G. A. Holzapfel, J. D. Humphrey, R. Kemkemer, E. Kuhl, J. E. Olberding, L. A. Taber, and K. Garikipati. Perspectives on biological growth and remodeling. *Journal of the Mechanics and Physics of Solids*, 59:863–883, 2011.

[4] G. A. Ateshian. On the theory of reactive mixtures for modeling biological growth. *Biomechanics and Modeling in Mechanobiology*, 6(6):423–445, 2007.

[5] G. F. Atkinson. *Lessons in Botany*. New York, H. Holt and Company, 1900.

[6] V. Balbi and P. Ciarletta. Helical buckling of thick-walled, pre-stressed, cylindrical tubes under a finite torsion. *Mathematics and Mechanics of Solids*, 2014.

[7] D. A. Bell. Kinematics of prey capture in the chameleon. *Zoologische Jahrbücher. Abteilung für allgemeine Zoologie und Physiologie der Tiere.*, 94(2):247–260, 1990.

[8] M. Ben Amar and A. Goriely. Growth and instability in elastic tissues. *Journal of the Mechanics and Physics of Solids*, 53:2284–2319, 2005.

[9] C. Bergernon and L.-P. Boulet. Structural changes in airway diseases: Characteristics, mechanisms, consequences and pharmacologic modulation. *Chest*, 129:1068–1087, 2006.

[10] R. Bernal, P. A. Pullarkat, and F. Melo. Mechanical properties of axons. *Physical Review Letters*, 99:018301, 2007.

[11] D. Bigoni and M. Gei. Bifurcations of a coated, elastic cylinder. *International Journal of Solids and Structures*, 38:5117–5148, 2001.

[12] M. Bock, K. Tyagi, Amit, J.-U. Kreft, and W. Alt. Generalized Voronoi tessellation as a model oftwo-dimensional cell tissue dynamics. *Bulletin of Mathematical Biology*, 72(7):1696–1731, 2010.

[13] C. P. Brangwynne, F. C. MacKintosh, S. Kumar, N. A. Geisse, J. Talbot, L. Mahadevan, K. K. Parker, D. E. Ingber, and D. A. Weitz. Microtubules can bear enhanced compressive loads in living cells because of lateral reinforcement. *Journal of Cell Biology*, 173:733–741, 2006.

[14] E. Brücke. Über die Zunge der Chamäleonen. *Sitzungsberichte / Akademie der Wissenschaften in Wien, Mathematisch-Naturwissenschaftliche Klasse Abteilung I, Biologie, Mineralogie, Erdkunde*, 8:65–71, 1852.

[15] L. Cardamone, A. Valentin, J. F. Eberth, and J. D. Humphrey. Origin of axial prestretch and residual stress in arteries. *Biomechanics and Modeling in Mechanobiology*, 8:431–446, 2009.

[16] N. Cauna and G. Mannan. The structure of human digital Pacinian corpuscles (corpuscula lamellosa) and its functional significance. *Journal of Anatomy*, 92(1):1–20.4, 1958.

[17] Y.-C. Chen and D. M. Haughton. Stability and bifurcation of inflation of elastic cylinders. *Proceedings of the Royal Society of London A*, 459(2029):137–156, 2003.

[18] J. H. de Groot and J. L. van Leeuwen. Evidence for an elastic projection mechanism in the chameleon tongue. *Proceedings of the Royal Society of London B*, 271:761–770, 2004.

[19] S. M. Deban, J. C. O'Reilly, U. Dicke, and J. L. van Leeuwen. Extremely high-power tongue projection in plethodontid salamanders. *Journal of Experimental Biology*, 210:655–667, 2007.

[20] B. S. Elkin, M. A. Shaik, and B. Morrison III. Fixed negative charge and the donnan effect: a description of the driving forces associated with brain tissue swelling and oedema. *Philosophical Transactions of the Royal Society of London A*, 368:585–603, 2010.

[21] L. Euler. *Sur la force des colonnes*. Vol. 13 Berlin, Germany: Memoires de l'Academie de Berlin., 1759.

[22] Y. Fan, H. Gregersen, and G. S. Kassab. A two-layered mechanical model of the rat esophagus. experiment and theory. *BioMedical Engineering Online*, 3:40, 2004.

[23] R. Farhadifar, J.-C. Röper, B. Aigouy, S. Eaton, and F. Jülicher. The influence of cell mechanics, cell-cell interactions, and proliferation on epithelial packing. *Current Biology*, 17(24):2095 – 2104, 2007.

[24] L. Frýba. History of Winkler foundation. *Vehicle System Dynamics*, 24:sup1:7–12, 1995.

[25] Y. B. Fu and M. Sanjarani Pour. WKB method with repeated roots and its application to the buckling analysis of an everted cylindrical tube. *SIAM Journal of Applied Mathematics*, 62(6):1856–1871, 2002.

[26] Y. C. Fung. What are the residual stresses doing in our blood vessels? *Annals of Biomedical Engineering*, 19:237–249, 1991.

[27] M. Gardner. Mathematical games the fantastic combinations of John Conway's new solitaire game "life". *Scientific American*, 223:120–123, 1970.

[28] T. C. Gasser, R. W. Ogden, and G. A. Holzapfel. Hyperelastic modelling of arterial layers with distributed collagen fibre orientations. *Journal of The Royal Society Interface*, 3(6):15–35, 2006.

[29] A. Gautieri, S. Vesentin, A. Redaelli, and M. J. Buehler. Hierarchical structure and nanomechanics of collagen microfibrils from the atomistic scale up. *Nano Letters*, 11:757–766, 2011.

[30] L. J. Gibson, M. F. Ashby, and B. A. Harley. *Cellular Materials in Nature and Medicine*. Cambridge University Press, 1st edition, 2010.

[31] D. L. Gilbert, W. J. Adelman, and J. M. Arnold. *Squid as experimental animals*. Springer, 1st edition, 1990.

[32] C. P. Gnanamuthu. The anatomy and mechanism of the tongue of chameleon carcaratus. *Proceedings of the Zoological Society of London*, 100(2):467–486, 1930.

[33] S. Göktepe, O. J. Abilez, K. K. Parker, and E. Kuhl. A multiscale model for eccentric and concentric cardiac growth through sarcomerogenesis. *Journal of Theoretical Biology*, 265(3):433 – 442, 2010.

[34] A. Goriely, D. E. Moulton, and R. Vandiver. Elastic cavitation, tube hollowing, and differential growth in plants and biological tissues. *Europhysics Letters*, 91:18001, 2010.

[35] A. Goriely and R. Vandiver. On the mechanical stability of growing arteries. *IMA Journal of Applied Mathematics*, 75:549–570, 2010.

[36] A. Goriely, R. Vandiver, and M. Destrade. Nonlinear Euler buckling. *Proceedings of the Royal Society of London A*, 464:3003–3019, 2008.

[37] A. Goriely and S. Neukirch. Mechanics of climbing and attachment in twining plants. *Physical Review Letters*, 97:184302, Nov 2006.

[38] F. Graner and J. A. Glazier. Simulation of biological cell sorting using a two-dimensional extended potts model. *Physical Review Letters*, 69:2013–2016, Sep 1992.

[39] A. E. Green, P. M. Naghdi, and M. L. Wenner. On the theory of rods. ii. developments by direct approach. *Proceedings of the Royal Society of London A*, 337(1611):485–507, 1974.

[40] H. Gregersen, D. Liao, and Y. C. Fung. Determination of homeostatic elastic moduli in two layers of the esophagus. *ASME Journal of Biomechanical Engineering*, 130:011005, 2008.

[41] W. Grossman. Cardiac hypertrophy: Useful adaptation or pathologic process? *American Journal of Medicine*, 69(4):576 – 584, 1980.

[42] M. Hayashi, K. L. Feilich, and D. J. Ellerby. The mechanics of explosive seed dispersal in orange jewelweed (impatiens capensis). *Journal of Experimental Botany*, 60(7):2045–2053, 2009.

[43] A. Herrel, J. J. Meyers, P. Aerts, and K. C. Nishikawa. Functional implications of supercontracting muscle in the chameleon tongue retractors. *Journal of Experimental Biology*, 204(21):3621–3627, 2001.

[44] A. Herrel, J. J. Meyers, K. C. Nishikawa, and F. De Vree. Morphology and histochemistry of the hyolingual apparatus in chameleons. *Journal of Morphology*, 249(2):154–170, 2001.

[45] L. R. Herrmann, W. E. Mason, and S. Chan. Response of reinforcing wires to compressive states of stress. *Journal of Composite Materials*, 1(3):212–226, 1967.

[46] E. K. Herzog, D. F. Bahr, R. F. Richards, and D. M. Rector. Spatially dependent mechanical properties of rat whiskers for tactile sensing. *Materials Research Society Symposium Proceedings*, 844:Y3.6/R3.6, 2005.

[47] G. A. Holzapfel, T. C. Gasser, and R. W. Ogden. A new constitutive framework for arterial wall mechanics and a comparative study of material models. *Journal of Elasticity*, 61:1–48, 2000.

[48] H. Honda. Description of cellular patterns by dirichlet domains: The two-dimensional case. *Journal of Theoretical Biology*, 72(3):523 – 543, 1978.

[49] J. Houston. On the structure and mechanism of the tongue of the chameleon. *The Transaction of the Royal Irish Academy*, 15:177–201, 1828.

[50] P. Howell, G. Kozyreff, and J. Ockendon. *Applied Solid Mechanics*. Cambridge University Press, 1st edition, 2009.

[51] J. Humphrey. Review paper: Continuum biomechanics of soft biological tissues. *Proceedings of the Royal Society of London A*, 459(2029):3–46, 2003.

[52] Z. S. Jackson, D. Dajnowiec, A. I. Gotlieb, and B. L. Langille. Partial off-loading of longitudinal tension induces arterial tortuosity. *Arteriosclerosis, Thrombosis and Vascular Biology*, 25:957–962, 2005.

[53] M. J. Jaffe and A. W. Galston. Physiological studies on pea tendrils. i. growth and coiling following mechanical stimulation. *Plant Physiology*, 41(6):1014–1025, 1968.

[54] R. D. Kamm. Airway wall mechanics. *Annual Review of Biomedical Engineering*, 01:47–72, 1999.

[55] G. N. Karam and L. J. Gibson. Biomimicking of animal quills and plant stems: natural cylindrical shells with foam cores. *Materials Science and Engineering C2*, 2:113–132, 1994.

[56] D. E. Kiousis, T. C. Gasser, and G. A. Holzapfel. A numerical model to study the interaction of vascular stents with human atherosclerotic lesions. *Annals of Biomedical Engineering*, 35(11):1857–1869, 2007.

[57] P. Lamoureux, S. R. Heidemann, N. R. Martzke, and K. E. Miller. Growth and elongation within and along the axon. *Developmental Neurobiology*, 70(3):135–149, 2010.

[58] G. E. Lang, P. S. Stewart, D. Vella, S. L. Waters, and A. Goriely. Is the Donnan effect sufficient to explain swelling in brain tissue slices? *Journal of The Royal Society Interface*, 11(96), 2014.

[59] W. R. Loewenstein and M. Mendelson. Components of receptor adaptation in a pacinian corpuscle. *Journal of Physiology*, 177(3):377–397, 1965.

[60] G. J. Lutz and L. C. Rome. Built for jumping: the design of the frog muscular system. *Science*, 263(5145):370–372, 1994.

[61] J. MacLaurin, S. J. Chapman, G. W. Jones, and T. Roose. The buckling of capillaries in solid tumours. *Proceedings of the Royal Society of London A*, 468:4123–4145, 2012.

[62] A. V. Melnik and A. Goriely. Dynamic fiber reorientation in a fiber-reinforced hyperelastic material. *Mathematics and Mechanics of Solids*, 18(6):634–648, 2013.

[63] J. J. Meyers and K. C. Nishikawa. Comparative study of tongue protrusion in three iguanian lizards, Sceloporus undulatus, Pseudotrapelus sinaitus and Chamaeleo jacksonii. *Journal of Experimental Biology*, 203(18):2833–2849, 2000.

[64] M. Mooney. A theory of large elastic deformation. *Journal of Applied Physics*, 11(9), 1940.

[65] M. S. Mora, Maria Giovanna. A nonlinear model for inextensible rods as a low energy γ-limit of three-dimensional nonlinear elasticity. *Annales de l'institut Henri Poincaré (C) Analyse non linéaire*, 21(3):271–293, 2004.

[66] D. E. Moulton and A. Goriely. Possible role of differential growth in airway wall remodeling in asthma. *Journal of Applied Physiology*, 110:1003–1012, 2010.

[67] D. E. Moulton and A. Goriely. Circumferential buckling instability of a growing cylindrical tube. *Journal of the Mechanics and Physics of Solids*, 59:525–537, 2011.

[68] D. E. Moulton, A. Goriely, and R. Chirat. Mechanical growth and morphogenesis of seashells. *Journal of Theoretical Biology*, 2012.

[69] D. E. Moulton, T. Lessinnes, and A. Goriely. Morphoelastic Rods Part I: A single growing elastic rod. *Journal of the Mechanics and Physics of Solids*, 61:398–427, 2013.

[70] T. Murmu and S. C. Pradhan. Buckling analysis of a single-walled carbon nanotube embedded in an elastic medium based on nonlocal elasticity and Timoshenko beam theory and using DQM. *Physica E*, pages 1232–1239, 2009.

[71] Y. Nakashima, T. N. Wright, and K. Sueishi. Early atherosclerosis in humans: role of diffuse intimal thickening and extracellular matrix proteoglycans. *Cardiovascular Research*, 79:14–23, 2008.

[72] A. Ní Annaidh, K. Bruyère, M. Destrade, M. D. Gilchrist, C. Maurini, M. Otténio, and G. Saccomandi. Automated estimation of collagen fibre dispersion in the dermis and its contribution to the anisotropic behaviour of skin. *Annals of Biomedical Engineering*, 40(8):1666–1678, 2012.

[73] R. W. Ogden. *Non-Linear Elastic Deformations*. Dover, 1st edition, 1997.

[74] S. G. O'Keeffe, D. E. Moulton, S. L. Waters, and A. Goriely. Growth-induced axial buckling of a slender elastic filament embedded in an isotropic elastic matrix. *International Journal of Non-Linear Mechanics*, 56(0):94 – 104, 2013. Soft Matter: a nonlinear continuum mechanics perspective.

[75] D. Parker. On the derivation of nonlinear rod theories from three-dimensional elasticity. *Zeitschrift für angewandte Mathematik und Physik*, 35(6):833–847, 1984.

[76] P. Pathmanathan, J. Cooper, A. Fletcher, G. Mirams, P. Murray, J. Osborne, J. Pitt-Francis, A. Walter, and S. J. Chapman. A computational study of discrete mechanical tissue models. *Physical Biology*, 6(3):036001, 2009.

[77] R. M. Pidaparti and K. Koombua. Tissue strains induced in airways due to mechanical ventilation. *Molecular and Cellular Biomechanics*, 8:149–168, 2011.

[78] J. Pitt-Francis, P. Pathmanathan, M. O. Bernabeu, R. Bordas, J. Cooper, A. G. Fletcher, G. R. Mirams, P. Murray, J. M. Osborne, A. Walter, S. J. Chapman, A. Garny, I. M. van Leeuwen, P. K. Maini, B. Rodríguez, S. L. Waters, J. P. Whiteley, H. M. Byrne, and D. J. Gavaghan. Chaste: A test-driven approach to software development for biological modelling. *Computer Physics Communications*, 180(12):2452 – 2471, 2009. 40 YEARS OF CPC: A celebratory issue focused on quality software for high performance, grid and novel computing architectures.

[79] P. Rissland, Y. Alemu, S. Einav, J. Ricotta, and D. Bluestein. Abdominal aortic aneurysm risk of rupture: Patient-specific fsi simulations using anisotropic model. *Journal of Biomedical Engineering*, 131(3):031001, 2009.

[80] R. S. Rivlin. Large elastic deformations of isotropic materials. i. fundamental concepts. *Philosophical Transactions of the Royal Society of London A*, 240(822):pp. 459–490, 1948.

[81] E. K. Rodriguez, A. Hoger, and A. D. McCulloch. Stress-dependent finite growth in soft elastic tissues. *Journal of Biomechanics*, 27:455–467, 1994.

[82] N. Rucci. Molecular biology of bone remodelling. *Clinical Cases in Mineral and Bone Metabolism*, 5(1):49–56, 2008.

[83] T. Savin, N. A. Kurpios, A. E. Shyer, P. Florescu, H. Liang, L. Mahadevan, and C. J. Tabin. On the growth and form of the gut. *Nature*, 476:57–62, 2011.

[84] I. A. T. Schaap, C. Carrasco, P. J. de Pablo, F. C. MacKintosh, and C. F. Schmidt. Elastic response, buckling, and instability of microtubules under radial indentation. *Biophysical Journal*, 91:1521–1531, 2006.

[85] K. U. Schmitt, P. Niederer, M. H. Muser, and F. Walz. *Trauma Biomechanics: Accidental injury in traffic and sports*. Springer, 3rd edition, 2009.

[86] J. M. Schröder, J. Bohl, and K. Brodda. Changes of the ratio between myelin thickness and axon diameter in the human developing sural nerve. *Acta Neuropathologica*, 43:169–178, 1978.

[87] M. Scianna and L. Preziosi. *Cellular Potts Models: Multiscale Extensions and Biological Applications*. Chapman & Hall/CRC Mathematical and Computational Biology. Taylor & Francis, 2013.

[88] W. L. Shan, Z. Chen, C. P. Broedersz, A. A. Gumaste, W. O. Soboyejo, and C. P. Brangwynne. Attenuated short wavelength buckling and force propagation in a biopolymer-reinforced rod. *Soft Matter*, 9:194–199, 2012.

[89] R. Skalak, G. Dasgupta, M. Moss, E. Otten, P. Dullemeijer, and H. Vilmann. Analytical description of growth. *Journal of Theoretical Biology*, 94(3):555 – 577, 1982.

[90] J. Soja, P. Grzanka, K. Sladek, K. Okon, A. Cmiel, M. Mikos, S. Mikrut, I. Gross-Sondej, E. Nizankowska-Mogilinicka, and A. Szczeklik. The use of endobronchial ultrasonography in assessment of bronchial wall remodelling in patients with asthma. *Chest*, 136:797–804, 2009.

[91] P. S. Spencer and H. H. Schaumburg. An ultrastructural study of the inner core of the pacinian corpuscle. *Journal of Neurocytology*, 2:217–235, 1973.

[92] T. Su, J. Liu, D. Terwagne, P. M. Reis, and K. Bertoldi. Buckling of an elastic rod embedded on an elastomeric matrix: planar vs. non-planar configurations. *Soft Matter*, 10:6294–6302, 2014.

[93] A. Szabó and R. M. H. Merks. Cellular potts modeling of tumor growth, tumor invasion and tumor evolution. *Frontiers in Oncology*, 3(87), 2013.

[94] D. A. W. Thompson and J. T. Bonner. *On Growth and Form*. Cambridge paperbacks. Cambridge University Press, 1992.

[95] C. Truesdell. The mechanical foundations of elasticity and fluid dynamics. *Indiana Univ. Math. J.*, 1:125–300, 1952.

[96] C. Truesdell and W. Noll. *The Non-Linear Field Theories of Mechanics*. Springer, 3rd edition, 2004.

[97] J. L. van Leeuwen. Why the chameleon has spiral-shaped muscle fibres in its tongue. *Philosophical Transactions of the Royal Society of London B*, 352:573–589, 1997.

[98] J. L. van Leeuwen, J. H. de Groot, and W. M. Kier. Evolutionary mechanics of protrusible tentacles and tongues. *Netherlands Journal of Zoology*, 50(2):113–139, 2000.

[99] R. Vandiver and A. Goriely. Tissue tension and axial growth of cylindrical structures in plants and elastic tissues. *Europhysics Letters*, 84:58004, 2008.

[100] R. Vandiver and A. Goriely. Differential growth and residual stress in cylindrical elastic structures. *Philosophical Transactions of the Royal Society of London A*, 367:3607–3630, 2009.

[101] R. Vandiver and A. Goriely. Morpho-elastodynamics: the long-time dynamics of elastic growth. *Journal of Biological Dynamics*, 3(2-3):180–195, 2009. PMID: 22880828.

[102] S. Vogel. Living in a physical world xi. to twist or bend when stressed. *Journal of Biosciences*, 32(4):643–655, 2007.

[103] D. Voges, K. Carl, G. J. Klauer, R. Uhlig, C. Schilling, C. Behn, and H. Witte. Structural characterization of the whisker system of the rat. *IEEE Sensors Journal*, 12:332–339, 2012.

[104] P. C. Wainwright and A. F. Bennett. The mechanism of tongue projection in chameleons. I. Electromyographic tests of functional hypotheses. *Journal of Experimental Biology*, 168:1–21, 1992.

[105] P. C. Wainwright and A. F. Bennett. The mechanism of tongue projection in chameleons: II. Role of shape change in a muscular hydrostat. *Journal of Experimental Biology*, 168:23–40, 1992.

[106] E. O. Winkler. *Die Lehre von der Elasticitaet und Feistigkeit. Theil 1, 2.* H. Dominicus, Prag, 1867.

[107] E. O. Winkler. *Vorträge über Eisenbahnbau. Heft 1, 2.* H. Dominicus, Prag, 1867.

[108] A. M. Zöllner, A. Buganza Tepole, A. K. Gosain, and E. Kuhl. Growing skin: tissue expansion in pediatric forehead reconstruction. *Biomechanics and Modeling in Mechanobiology*, 11(6):855–867, 2012.

[109] A. Zoond. The mechanism of projection of the chameleon's tongue. *Journal of Experimental Biology*, 10(2):174–185, 1933.